

**Promoter:**

Prof. dr. ir. Pascal Verdonck  
IBiTech  
Ghent University  
Campus Heymans  
De Pintelaan 185  
9000 Gent  
Belgium

**Members of the examination committee:**

Prof. Dr. ir. Ronny Verhoeven (chairman, Faculty Engineering, UGent)  
Prof. Dr. ir. Patrick Segers (secretary, Faculty Engineering, UGent)  
Prof. Dr. ir. Jan Vierendeels (Faculty Engineering, UGent)  
Prof. Dr. Guido Van Nooten (Faculty Medicine and Health Sciences,  
UGent)  
Dr. Ir. Tom Claessens (HoGent)  
Prof. Dr. Hans Weber (Aachen University of Applied Sciences)  
Dr. Ing. Stephan Kallweit (Intelligent Laser Applications GmbH)  
Dr. ir. Ashraf Khir (Brunel University)  
Prof. Dr. ir. Pascal Verdonck (supervisor, Faculty Engineering, UGent)



### *Acknowledgments*

At the time, when I started the PhD study I didn't know yet, that this activity requires such an amount of working hours, amazing input of energy and endless enthusiasm. However, it was interesting experience, which gave me a lot of knowledge, satisfaction and also very important - friendships and love. To obtain a doctoral degree, a well known phrase "being the right person in the right time at the right place" can't work anymore. There are many people they helped me in professional, private or both manners at ones to achieve the current level of knowledge and personality.

I am very thankful to my supervisor Prof. Pascal Verdonck for his endless support, professional face-to-face approach and very friendly behavior. It was awesome to have the opportunity present the results and get the knowledge at high ranked scientific international conferences worldwide.

I feel grateful for the extensive help and friendships of the company Intelligent Laser Applications GmbH, namely Michael Dues, Michael Schroll and Stephan Kallweit. Many thanks especially to Stephan, who was always there, early in the morning or late in the evening or in between, to answer my stupid questions about experiments.

Many thanks to my colleagues at the IBiTech for a very nice atmosphere. It was pleasure to have you around and have fun with you: Abigail, Benjamin, Daniel, Denis, Dries, Frederic, Guy, Jan, Koen, Lieve, Matthieu, Mirko, Patrick, Peter, Seba, Sunny and Tom. Special thanks belong to Guy for his friendliness and professional help in means of scientific writing. It would not be complete if I don't mention here my former colleague Kris Dumont, thank you!

Once you will read this thesis you will find out that the models plays in research a fundamental role. I would like to give my thanks to the technicians: Jürgen, Marcel, Martin and Stefaan, who were manufacturing high quality models for our research and thus made it possible to achieve presented results.

It was a pleasure to work in Italy not only because of nice weather, tasty pizza and long beaches (and more), but also because of meeting great people to work with and spend a great time with. I send my thanks to Massimiliano Rossi and Umberto Morbiducci for their friendship, help and wonderful cooperation with great professional background.

I am very thankful to all my friends, just because they are. I would like to give my special thanks to: Marián Drošč; Peter Vaško; Ján Ivanko; David· Alex· Merce· Seliz· Paula Alvarez Lopez; Magnolia Grau Galvez; Mark Tawileh and Zuzka.

Here, to point out, I give my thousands thanks to my family, parents and brothers, for all those 30 years of endless support and love.

## **Table of contents**

Acknowledgments	iii
Samenvatting	xii
Summary	xviii

## **A. BACKGROUND: CARDIOVASCULAR ANATOMY, PHYSIOLOGY, AND PARTICLE IMAGE VELOCIMETRY** **1**

### **I. CARDIOVASCULAR ANATOMY AND PHYSIOLOGY** **3**

#### **I.1. INTRODUCTION** **5**

##### **I.1.1. SYSTEMIC AND PULMONARY BLOOD CIRCULATION** **5**

##### **I.1.2. ANATOMY OF THE HEART** **6**

##### **I.1.3. THE CARDIAC CYCLE.** **8**

##### **I.1.4. BLOOD** **10**

##### **I.1.5. HEART VALVES** **11**

###### **I.1.5.1. Structure and function of the heart valves** **11**

###### **I.1.5.2. Valvular diseases** **13**

###### **I.1.5.3. Prosthetic heart valves** **14**

##### **I.1.6. CONCLUSION** **17**

#### **I.2. INTRODUCTION TO CENTRAL VENOUS HEMODIALYSIS CATHETERS** **19**

##### **I.2.1. VASCULAR ACCESS FOR EXTRACORPOREAL THERAPY** **21**

### **II. PARTICLE IMAGE VELOCIMETRY** **25**

#### **II.1. INTRODUCTION** **27**

#### **II.2. ILLUMINATION OF THE ROI** **28**

II.2.1.	LASERS.	29
II.2.1.1.	Neodym-YAG (Nd:YAG) lasers	29
II.2.1.2.	Neodym-YLF (Nd:YLF) lasers	31
II.2.2.	LASER SAFETY	32
II.2.3.	LIGHT SHEET OPTICS (LSO)	32
II.2.4.	PARTICLES	35
<b>II.3.</b>	<b>SIGNAL RECORDING</b>	<b>39</b>
II.3.1.	CCD CAMERAS	40
II.3.2.	CMOS CAMERAS	45
<b>II.4.</b>	<b>IMAGE PROCESSING.</b>	<b>47</b>
II.4.1.	CALIBRATION OF THE IMAGES.	52
II.4.2.	PRE-PROCESSING OF THE IMAGES.	54
II.4.3.	TIMING OF THE PIV PERFORMANCE.	54
II.4.4.	ANNOTATIONS OF THE IMAGES.	55
<b>II.5.</b>	<b>CONCLUSION.</b>	<b>55</b>

**B. IN VITRO STUDY OF BLOOD FLOWS BY PARTICLE IMAGE VELOCIMETRY** **57**

**III. INTRODUCTION** **59**

**IV. PIV VALIDATION OF BLOOD-HEART VALVE LEAFLET INTERACTION MODELLING** **61**

**ABSTRACT** **62**

<b>IV.1. INTRODUCTION</b>	<b>63</b>
<b>IV.2. METHODS</b>	<b>64</b>
IV.2.1. EXPERIMENTAL MODEL	64
IV.2.2. NUMERICAL MODEL	67
<b>IV.3. RESULTS</b>	<b>70</b>
<b>IV.4. DISCUSSION</b>	<b>75</b>
<b>IV.5. CONCLUSIONS</b>	<b>77</b>

**V. STEREOSCOPIC PIV MEASUREMENTS OF FLOWS BEHIND  
ARTIFICIAL HEART VALVE** **80**

**ABSTRACT** **81**

<b>V.1. INTRODUCTION</b>	<b>82</b>
<b>V.2. MATERIALS AND METHODS</b>	<b>83</b>
V.2.1. THE TESTING LOOP	84
V.2.2. 3C PIV: MEASUREMENT TECHNIQUE	87
<b>V.3. RESULTS</b>	<b>89</b>
<b>V.4. DISCUSSION</b>	<b>91</b>
<b>V.5. CONCLUSION</b>	<b>93</b>

**VI. HIGH SPEED PIV TECHNIQUE FOR HIGH TEMPORAL  
RESOLUTION MEASUREMENT OF MECHANICAL PROSTHETIC  
AORTIC VALVE FLUID DYNAMICS** **95**

**ABSTRACT** **96**

<b>VI.1. INTRODUCTION</b>	<b>97</b>
<b>VI.2. MATERIALS AND METHODS</b>	<b>98</b>
<b>VI.3. MEASUREMENT TECHNIQUE</b>	<b>98</b>
<b>VI.4. RESULTS</b>	<b>101</b>
<b>VI.5. DISCUSSION</b>	<b>106</b>
<b>VI.6. CONCLUSION</b>	<b>110</b>

**VII. FLOW VISUALIZATION THROUGH TWO TYPES OF  
AORTIC PROSTHETIC HEART VALVES USING STEREOSCOPIC  
HIGH SPEED PARTICLE IMAGE VELOCIMETRY** **111**

**ABSTRACT** **112**

<b>VII.1. INTRODUCTION</b>	<b>113</b>
<b>VII.2. MATERIALS AND METHODS</b>	<b>115</b>
VII.2.1. MOCK LOOP	115
VII.2.2. STEREOSCOPIC HIGH SPEED PIV SET-UP	118
<b>VII.3. RESULTS</b>	<b>120</b>
VII.3.1. BILEAFLET ATS VALVE	121
VII.3.2. MONOLEAFLET PHV	124
<b>VII.4. DISCUSSION</b>	<b>127</b>
<b>VII.5. CONCLUSION</b>	<b>129</b>

**VIII. PIV VALIDATION OF CFD BASED DESIGNS OF CENTRAL  
VENOUS HEMODIALYSIS CATHETER** **131**

**ABSTRACT** **132**

<b>VIII.1. INTRODUCTION</b>	<b>133</b>
<b>VIII.2. MATERIALS AND METHODS</b>	<b>134</b>
VIII.2.1. CATHETER DESIGNS	134
VIII.2.1.1. Three catheter designs studied by PIV and CFD	134
VIII.2.1.2. Four additional catheter designs studied by CFD only	135
<b>VIII.3. PIV ANALYSIS</b>	<b>136</b>
VIII.3.1. CATHETER PROTOTYPES	136
VIII.3.2. EXPERIMENTAL SETUP	137
VIII.3.3. MEASUREMENT PROTOCOL	138
VIII.3.4. CFD ANALYSIS	140
VIII.3.4.1. Comparison with PIV	140
VIII.3.4.2. Assessment of shear stress levels and blood residence time	141
<b>VIII.4. RESULTS</b>	<b>144</b>
VIII.4.1. CFD VALIDATION BY PIV MEASUREMENTS FOR THREE CATHETER DESIGNS	144
VIII.4.2. CFD ASSESSMENT OF SS AND RT IN THE TIP OF 7 CATHETER DESIGNS	146
<b>VIII.5. DISCUSSION</b>	<b>148</b>
<b>VIII.6. CONCLUSION</b>	<b>152</b>
<b><u>IX. CONCLUSIONS AND FUTURE PROSPECTS.</u></b>	<b><u>154</u></b>
<b><u>BIBLIOGRAPHY</u></b>	<b><u>158</u></b>
<b><u>SYMBOLS, ABBREVIATIONS AND UNITS</u></b>	<b><u>170</u></b>

**ABBREVIATIONS** **171**

---

**SYMBOLS** **172**

---

**UNITS** **173**

---



## *Samenvatting*

De belangrijkste doelstelling van dit proefschrift is het voorstellen van experimenteel onderzoek naar bloedstroming in cardiovasculaire apparaten met behulp van de Particle Image Velocimetry (PIV) techniek. Hierdoor wordt het potentieel van deze techniek geïllustreerd in zijn toepassing op de studie van de hemodynamische eigenschappen van bloedstroming, en wordt gewezen op het specifieke nut ervan in biomedisch ingenieurs gericht onderzoek.

Dit proefschrift is opgebouwd uit twee delen. Deel A - Background verstrekt een inleiding tot de anatomie en fysiologie van het menselijk hart en cardiovasculair systeem. Bijzondere aandacht gaat naar de eigenschappen van hartkleppen en hun mogelijke ziekten. Hierna wordt PIV beschreven als een experimenteel hulpmiddel voor vloeistofdynamisch onderzoek. Verscheidene modaliteiten van PIV die later in dit proefschrift worden gebruikt, worden voorgesteld. Deel B omvat een selectie van experimentele studies die tijdens mijn doctoraal onderzoeksprogramma werden uitgevoerd. Het wordt onderverdeeld in twee secties: De grootste sectie behandelt een vergelijking van verschillende benaderingen van PIV om de dynamica van de vloeistofstroming afwaarts van hartkleppen te bestuderen. De tweede sectie concentreert zich op vaattoegang. Beide secties sluiten af met een samenvatting waarin de voordelen en de beperkingen van de gebruikte methodologieën worden besproken en de toekomstige vooruitzichten worden voorgesteld.

**Hoofdstuk I.**, geeft, als inleiding, een beschrijving van de cardiovasculaire anatomie en fysiologie van het menselijk lichaam. De bouw van het hart, de systemische en pulmonaire bloedsomloop worden besproken om een beeld te hebben van de bloedstroming in het lichaam. Hier wordt ook de volledige hartcyclus voorgesteld, en worden de relatie tussen zijn individuele fasen en elektrocardiogram, druk- en stromingsverdeling besproken. Speciale aandacht gaat uit naar de hartkleppen, waarbij hun functie en onderlinge verschillen worden besproken. Verder worden klepgerelateerde hartziekten (valvular heart diseases - VHD) vermeld, die ofwel verworven (b.v. door ontsteking, ongeval, etc.), ofwel aangeboren kunnen zijn. Tot slot worden prothetische hartkleppen

(prosthetic heart valve - PHV) voorgesteld als voorbeeld van een gangbare behandeling van ernstige VHD's.

**Hoofstuk II.** concentreert zich hoofdzakelijk op het verklaren van het werkingsprincipe van de experimentele Particle Image Velocimetry techniek, en het beschrijven van zijn fundamentele componenten. Particle Image Velocimetry (PIV) is al geruime tijd een gevestigde techniek in de automobiel- en luchtvaartindustrie, maar werd slechts recentelijk geïntroduceerd in het biomedische onderzoeksgebied. Het belangrijkste doel van dit proefschrift is om de verschillende modaliteiten van PIV in hun toepassing op biomedische stromingsproblemen voor te stellen, en als dusdanig de rechtstreekse voordelen van deze bijzondere techniek in biomedisch ingenieursonderzoek aan te tonen. Onrechtstreeks kan de techniek ook dienen als referentie, ter validatie van numerieke stromingssimulaties (Computational Fluid Dynamics – CFD). Omdat er een aanzienlijke lagere kost mee geassocieerd is in vergelijking met PIV, is CFD uitgegroeid tot een populair hulpmiddel om, met behulp van virtuele computermodellen, de dynamica van vloeistofstroming te bestuderen. Niettemin zijn biomedische stromingsproblemen zeer complex en kunnen ze in veel gevallen nog niet met voldoende nauwkeurigheid gemodelleerd worden met CFD. Daarom is er de behoefte om deze CFD techniek steeds te valideren vooraleer hij kan gebruikt worden als alleenstaand, standaard onderzoeksmiddel in biomedische stromingsproblemen. Het belangrijkste voordeel van PIV is zijn niet-invasieve en niet-obstructieve aanpak, wat het de beste planaire visualisatietechniek maakt qua nauwkeurigheid. Om deze reden wordt PIV ook wijdverspreid toegepast in de automobiel-, luchtvaart-, en zeevaartindustrie, waar stroming telkens een beslissende rol speelt in de performantiecriteriën. Niettemin werd PIV tijdens mijn studie slechts in enkele gebieden van het biomedisch onderzoeks domein toegepast. De belangrijkste doelstelling was om verschillende PIV technieken toe te passen op verscheidene bloedstromingen om zodoende de geschiktheid van deze techniek om deze complexe stromingen kwantitatief te bestuderen, aan te tonen.

**Hoofdstuk III.** is een inleiding tot de onderzoeksgevallen die voorgesteld zijn in deel **B** van deze verhandeling. Dit hoofdstuk bevat ook een korte samenvatting van deel **A**.

**Hoofdstuk IV.** stelt de eerste PIV studie voor. Het doel van deze studie was het valideren van 2D Computational Fluid Dynamics (CFD) simulaties van een bewegende hartklep. Deze simulaties kwamen tot stand met een vloeistof-wand-interactie (fluid-structure interaction – FSI) algoritme, dat nu met experimentele metingen werd gevalideerd. Hiervoor werd de pulsatiele, laminaire stroming doorheen een monoleaflet klepmodel met een stijf klepblad gevisualiseerd.

De bemeten regio met het stijve klepblad was deel van een *in vitro* testcircuit waarin ze in serie stond met een pulsatiele bloedpomp, een compliantiekamer en een vloeistofreservoir. Standaard 2D PIV metingen werden uitgevoerd aan een hartslag van 60 bpm. Gemiddelde snelheidsresultaten van 36 fase-gekoppelde metingen werden geëvalueerd bij elke 10° van de pompcyclus. CFD in combinatie met specifieke FSI code gebaseerd op de ‘Arbitrary Lagrangian-Eulerian’ (ALE) methode werd gebruikt om de stromingssimulaties uit te voeren. De CFD resultaten konden ook een beeld geven van de afschuifspanningen op het klepblad.

Over het algemeen waren de CFD resultaten in goede overeenstemming met de experimentele PIV data. Hierdoor werd de FSI code om de stroming door en de beweging van een monoleaflet klep te simuleren, gevalideerd.

**Hoofdstuk V.** toont de eerste experimentele studie die de 3 componenten van de snelheid in rekening brengt. Voor de experimentele beoordeling van de stroming doorheen een PHV werd stereoscopische PIV gebruikt om aan te tonen dat deze techniek geschikt is om zulke complexe stromingen te kwantificeren door alle drie de snelheidscomponenten in het meetvlak in rekening te brengen. Aangezien de hardware vereisten, de configuratie en de opzet voor stereoscopische PIV veel complexer zijn dan voor standaard 2D PIV, is speciale aandacht nodig voor het ontwerp van het testcircuit om een optimale optische toegang te verzekeren. Zulk een testcircuit werd ontworpen aan de

University Polytechnica delle Marche in Ancona, Italië waar deze experimentele studie werd uitgevoerd. De stroming achter een bileaflet PHV werd gevisualiseerd in twee verschillende klepvlakken: 1 en 3 cm stroomafwaarts van de klep. Er werd geconcludeerd dat stereoscopische PIV de beste mogelijkheden biedt om het niet-stationaire stromingsgedrag doorheen een klep met twee klepblaadjes tijdens een hartcyclus te bestuderen.

**Hoofdstuk VI.** laat de tijdsresolutie zien van een hartcyclus wanneer stroming wordt gevisualiseerd door middel van hoge snelheids-PIV. Meer specifiek is de stroming doorheen een mechanische bileaflet PHV het doel van deze experimentele studie. Het bestudeerde stromingsveld komt overeen met de zone onmiddellijk stroomafwaarts van het klepvlak in de centrale doorsnede volgens de as van de hoofdstromingsrichting. Spatiale resolutie vergelijkbaar met deze in standaard PIV werd bereikt. De gebruikte combinatie van een Nd:YLF *high-repetition-rate double-cavity* laser met een hoge-snelheid CMOS camera laat een gedetailleerde data-acquisitie toe met uiterst hoge tijdsresolutie. Stromingseigenschappen die waargenomen werden omvatten inhomogene en niet-stationere fenomenen en de aanwezigheid van grote wervels in het stromingsveld. Verder werd aangetoond dat een analyse met een hoge tijdsresolutie nodig was om het gedrag van een bileaflet klep bij sluiting te kunnen vatten gedurende verschillende hartcycli. Er werd geconcludeerd dat door het nauwkeurig bevatten van hemodynamisch relevante tijdsschalen in de stroming, tijdsafhankelijke PIV karakterisering van de stroming nuttig en relevant is om in uitvoerige validatie van numerieke simulaties te voorzien en om ontwerpers te helpen om de performantie van PHV's te verbeteren.

**Hoofdstuk VII.** breidt de PIV techniek die in het vorige hoofdstuk werd voorgesteld, uit naar een stereoscopische configuratie met een tweede camera in de hardware set-up. Deze stereoscopische hoge-snelheids PIV metingen werden echter op een ander testcircuit toegepast, dat ontworpen is aan de University of Applied Sciences in Aachen, Duitsland. Deze nieuwe PIV methode werd toegepast om alle drie de snelheidscomponenten in een vlak achter een PHV te bestuderen in een gedetailleerd tijdsdomein. In deze studie wordt een klinisch gebruikte ATS klep met twee klepblaadjes vergeleken met

een prototype klep ontwikkeld aan de Technical University van Lodz, Polen. Deze laatste PHV heeft een enkelvoudig klepblad volgens het 'tilting disc' principe. De absolute snelheden werden berekend uit twee en drie snelheidscomponenten en onderling vergeleken in de verschillende bemeten gebieden. De meest significante discrepanties tussen de twee- en driecomponent absolute snelheidswaarden werden gevonden in de zones van Valsalva sinussen en in de belangrijke jet-stroom bij de monoleaflet PHV. Onze studie toont aan dat de derde snelheidscomponent in de stroming na een PHV geen sterke impact heeft op de algemene absolute snelheid. Dit is vooral het geval in het bileaflet klepmodel. Nochtans moet men opmerken dat in kleine zones vooral nabij de Valsalva sinussen en in de buurt van de klepbladen zelf, de snelheden loodrecht op het meetvlak hoge waarden kunnen bereiken tijdens de opgaande systolische fase. Dit moet men in het achterhoofd houden wanneer men (vaak 2D) numerieke simulaties wil valideren.

**Hoofdstuk VIII.** beschouwt het eerste geval van stromingsvisualisatie in vasculaire vaattoegang. De stroming in de tipzone van verschillende centraal veneuze katheters werd bestudeerd door middel van een gecombineerde numerieke en experimentele aanpak. CFD simulaties werden gevalideerd met PIV metingen door de gesimuleerde en experimenteel bemeten stromings- en afschuifspanningsverdeling in de tipzone van het bloedtrekkende ('arteriële') lumen van drie katheter-ontwerpen te vergelijken. Deze drie katheterontwerpen verschillen onderling enkel in het 'arteriële' lumen: het is cilindrisch en met de tip (1) recht afgesneden, (2) schuin afgesneden, of (3) recht afgesneden met een sleuf-vormige ingang. Na deze validatie werden nog vier bijkomende ontwerpen numeriek bestudeerd: een katheter (4) met twee zijgaatjes en een recht afgesnede tip of (5) idem maar schuin afgesneden, (6) een katheter met concentrische lumina en (7) een Ash Split gebaseerde katheter. In de tipzone van deze zeven katheterdesigns werd de afschuifspanning (shear stress - SS), de verblijftijd van het bloed (blood residence time - RT), en de zgn. Platelet Lysis Index als parameters gebruikt om de hemodynamische performantie van elk katheterontwerp te kwantificeren. Als conclusie wordt gesteld dat de bloedstroming door de concentrische catheter onderhevig is aan sterk verhoogde

schuifspanningswaarden. Het ‘Ash Split’ gebaseerde ontwerp heeft verhoogde RT waarden in het meest distale deel van de tip doordat de meeste instroom gebeurt doorheen de meest proximale zijgaatjes. Qua performantie wordt dit gecompenseerd door de lage gemiddelde SS. Een katheter met een recht afgesneden tip en eventueel twee zijgaatjes wordt aanbevolen wanneer men een optimale combinatie van minimale SS en RT wenst te bereiken. Deze simulaties werden gevalideerd door de PIV metingen en kunnen leiden tot meer performante katheters.

**Hoofdstuk IX.** bespreekt de voor- en nadelen van de voorgestelde modaliteiten van de PIV techniek, samen met toekomstige vooruitzichten. Gebaseerd op de gepresenteerde gevallen kunnen we zeggen dat PIV een geschikte techniek is om dit soort stromingen te bestuderen. Meer zelfs, door zijn nauwkeurigheid is het een standaard techniek geworden om CFD gebaseerde simulaties en ontwerpen te valideren. In de toekomst zal in het biomedisch onderzoeksveld steeds meer en meer gebruik gemaakt worden van CFD voor het kwantificeren van patiëntspecifieke stromingen. Niettemin staat deze bioCFD aan het begin van zijn evolutie en vereist het nog steeds een experimentele validatie bij complexe stromingen, zoals in het geval van vloeistof-wandinteractie.

## ***Summary***

The main goal of this dissertation is to present experimental investigations of blood flow dynamics in cardiovascular devices with the Particle Image Velocimetry (PIV). This is done in order to demonstrate the capability of this technique to study the haemodynamic properties of the blood flow and point out the usefulness in biomedical research.

This dissertation is organized in two major parts. Part **A** - Background provides an introduction into the anatomy and physiology of the human heart and cardiovascular system. The structure and functions of heart valves and their possible diseases are described in detail. Afterwards PIV will be described as an experimental tool for fluid dynamic investigation. Several different PIV setups used later in this dissertation are presented. Part **B** contains selected experimental cases performed during my doctoral research programme. It is subdivided into two sections: The major section covers a comparison of different PIV modalities to study the flow distribution behind heart valves. The second part focuses on vascular access in the superior vena cava. In the summary the benefits and limitations of the used methods are discussed and future prospects are suggested.

**Chapter I.** describes cardiovascular anatomy and physiology of the human body. The architecture of the heart and systemic and pulmonary blood circulation are here described in detail in order to understand the blood flow pathways. Here a complete cardiac cycle is depicted and its individual phases are described with relation to the Electrocardiogram, pressure and flow distribution. A special interest was given to heart valves, their functions. The differences among them were noted. Furthermore valvular heart diseases (VHD) are mentioned, as a consequence of either acquired (e.g. inflammation, accident, etc.) or congenital factors. Afterwards prosthetic heart valves (PHV) are presented as examples of a common treatment to severe VHDs.

**Chapter II.** is mainly focused to explain the working principles of the experimental method - Particle Image Velocimetry - and to describe its

fundamental components. Particle Image Velocimetry (PIV) is an already well established technique in automotive and aeronautical industry but only recently introduced in the biomedical field. The main goal of this dissertation is to present various modalities of PIV in biomedical flows. The aim is to demonstrate benefits of particular techniques for biomedical engineering and research. The PIV results can be used to serve as a reference to validate Computational Fluid Dynamic (CFD) codes. Modelling the flow with CFD is becoming very popular in biomedical engineering. It is not only due to the lower cost in terms of time and budget. Moreover, CFD is able to determine the results in regions, where experimental techniques don't have any access. However, the biomedical flows are very complex and in many cases cannot yet be truly determined with CFD. Therefore, there is a need to further validate this CFD technique before being used as a standard application for biomedical flows. The main advantage of PIV is its non-intrusive approach, which is nowadays the best planar visualization technique by means of accuracy.

**Chapter III.** is in fact an introduction to the research study cases presented in the **B** part of this dissertation. It also contains a brief summary of part **A**.

**Chapter IV.** presents the 1<sup>st</sup> experimental PIV study. The aim of this study was to validate the 2D CFD results of a moving heart valve based on a fluid-structure interaction (FSI) algorithm with experimental measurements. A pulsatile laminar flow through a monoleaflet valve model with a stiff leaflet was visualized.

The measurement section with a fixed leaflet was enclosed into a mock loop in series with a pulsatile blood pump, a compliance chamber and a reservoir. Standard 2D PIV measurements were made at a heart rate of 60 bpm. Phase averaged results of 36 phase locked measurements were evaluated at every 10° of the pump cycle. With the CFD in combination with FSI specific code, a flow simulation was performed based on the Arbitrary Lagrangian-Eulerian ALE method. The results of CFD also quantify the shear stress on this leaflet.

Generally the CFD results are in agreement with the PIV data in major flow regions, but there are still mismatches in some regions.

**Chapter V.** shows the first experimental study considering the third component velocity values. For the experimental assessment of the flow through prosthetic heart valves PHVs a stereoscopic PIV system is applied. Stereoscopic PIV is able to quantify the third velocity ( $w$ ) component in addition to the in plane components ( $u, v$ ). Since the hardware requirements and its configuration for stereoscopic PIV is much more complex than standard 2D PIV, the design of the testing loop has to be considered particularly in order to allow optimal optical access. Such a mock loop was designed at the University Polytechnica delle Marche in Ancona, where this experimental study was done. The flow behind a bileaflet PHV is visualized in two different valve planes, 10 and 30 mm downstream the valve.

**Chapter VI.** reveals the temporal resolution of the cardiac cycle when visualizing the flow by high speed PIV. Here the determination of the fluid dynamics behind a bileaflet mechanical PHVs is the aim of this experimental study. The investigated flow field corresponds to the region immediately downstream of the valve plane in the central cross-section within the axis of the main flow. The high speed CMOS cameras used for the first time in PIV were having low resolution (256x256 pixels) compared to CCD camera (higher than 1000x1000 pixels). In this study a high speed camera with 1024x1024 pixels is used and thus the same spatial resolution is achieved as in standard PIV. The used combination of a Nd:YLF high-repetition-rate double-cavity laser with a high frame rate (1 kHz) CMOS camera allows an acquisition with high temporal resolution. Features that are observed include the non-homogeneity and unsteadiness of the flow and the presence of large-scale vortices within the field of view. Furthermore, the different closing behaviour of a bileaflet valve in two consecutive cardiac cycles was observed by means of HiSpeed PIV.) By accurate capturing haemodynamically relevant time scales of motion, time-resolved PIV characterization results may provide comprehensive validation with experimental data on fluid dynamics numeric modelling. In addition, HiSpeed PIV provides comprehensive validation data for CFD modelling, if the acquisition is done in haemodynamically relevant time scales.

**Chapter VII.** extends the PIV technique presented in the previous chapter by a stereoscopic configuration including a second camera. However, this stereoscopic high speed PIV measurements are performed on a different mock loop, designed at the University of Applied Sciences in Aachen. This novel PIV method is applied to quantify all three velocity components behind a PHV. In this study we compare a clinically used bileaflet ATS valve to a monoleaflet prototype of tilting disc PHV designed at the Technical University Lodz. The absolute velocities calculated out of two and three velocity components were compared to each other in order to estimate the overall difference in the desired ROI. The most significant discrepancies between the two- and three-component absolute velocities were found at the regions of Valsalva sinuses and in a major jet stream of the monoleaflet PHV. Our study shows that the third velocity component in the flow behind a PHV doesn't have a strong impact on the overall absolute velocity, especially in the bileaflet model. However, it has to be also noted that in small regions mainly in the regions of Valsalva sinuses and in the vicinity of leaflets the out-of-plane velocity values are reaching quite a high values during the accelerating systolic phase. This should be kept in mind when validating numerical codes (CFD), which are commonly 2D.

**Chapter VIII.** considers the first case of vascular access flow visualization. Flow zones are assessed in different central venous catheter tip designs using a combined numerical and experimental approach. Hence CFD is validated with PIV by comparing simulated and experimentally obtained velocity field and shear strains in three catheter designs of the blood withdrawing 'arterial' lumen: cylindrical and with tip (1) cut straight, (2) cut at an angle, or (3) cut straight with a sleeve entrance. After validation, four additional designs were studied: (4) with two side holes and tip cut straight or (5) at an angle, (6) concentric lumens and (7) Ash Split based. In these seven designs, shear stress, blood residence time (RT), and Platelet Lysis Index are the parameters considered to quantify the quality of the haemodynamic properties of each catheter design. 'Ash Split' based design has elevated RT values in the distal tip zone as major inflow occurs through the most proximal side holes, but this is compensated by low average shear stress. A straight cut tip and possibly two

side holes are preferred when aiming at minimal shear stress and RT. CFD was validated by using PIV. These data may lead to more patent catheters.

**Chapter IX.** is discussing the benefits and drawbacks of the presented modalities of PIV and future prospects are given. Based on the demonstrated cases, PIV is suitable technique for studying these kinds of flows. Moreover, due to its accuracy, it has nowadays become also a standard technique to validate CFD based designs and simulations. The future directions in biomedical field tend to use CFD codes for the quantification of patient specific flow conditions across an artificial organ. Nevertheless, bioCFD is at the beginning of its evolution and still needs an experimental validation in complex flows such as in case of fluid-structure interaction. Based on the presented results, the flow through bileaflet valves is qualitatively better than through the monoleaflet. This assumption is concerning the velocity distribution and gradients, vortex structure formation and shear stress distribution. These aspects have significant impact on blood cells damage, which is the main concern of the mechanical prosthetic heart valves (PHV). Nevertheless, the blood damage imposed by bileaflet valves is still present and therefore there is a need of improving their design. There are different bileaflet PHV commercially available, which differ in the shape of the leaflet, opening angle and architecture of the hinges. In order to judge their quality, a detailed comparison study with PIV would be useful.

**A. Background:**  
**Cardiovascular anatomy,  
physiology, and Particle  
Image Velocimetry**



# I. Cardiovascular anatomy and physiology



## **I.1. Introduction**

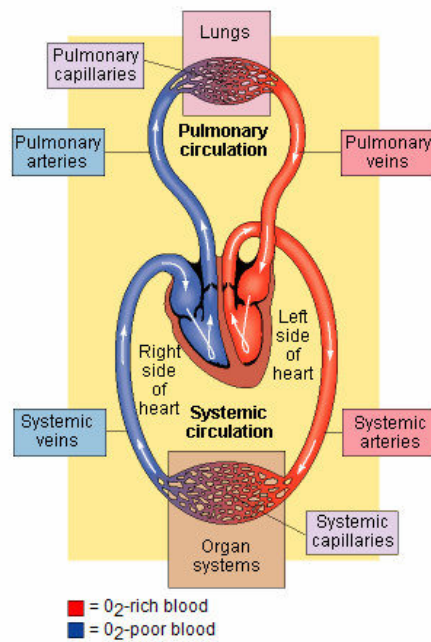
Thousands of years ago, the heart has been conceptualized as a symbol to refer to the spiritual, emotional, moral, and also intellectual core of a human being. It was considered as an organ responsible to take decision. The reason for this was probably the feeling of increased heart rate in any kind of strong emotional events. For its mythic history the heart is nowadays still used as a symbol, however, it mostly symbolizes “love”.

Despite the mythical assumptions, science discovered completely other functions of the heart: it is now known as the organ which is responsible for pumping the blood through the vascular system of the body under correct pressure conditions. The vascular system of the human body plays a significant role as it links all organs together in order to allow exchange of miscellaneous substances, contained in the blood. It consists of a tapered network of vessels through which blood flows. There are two categories in which blood vessels are divided: arteries carry blood away from the heart and veins carry blood back to the heart. The vascular system is working in a closed loop in which the blood is pumped by the heart. The main artery leading from the heart to the rest of the body is called the aorta. It divides into smaller branches which are linked to the different organs. Furthermore, as the blood flows, it enters smaller and smaller blood vessels, reaching the organs, different layers of tissues down to cellular level, dropping off nutrients and picking up waste products and carbon dioxide.

### **I.1.1. Systemic and pulmonary blood circulation**

The systemic blood circulation is a network consisting of the heart and vessels perfusing all organs except lungs, where a network of vessels is creating the pulmonary circulation. The blood flow in the pulmonary and systemic circulation is powered by the heart, which acts like a pump. The vascular loop of the human body is presented in figure I-I. The heart consists of four

chambers: the upper two are the right (RA) and left atrium (LA); the lower two represent the right (RV) and left ventricle (LV). In a healthy body, deoxygenated blood is pumped from the body through the RA and RV to the lungs. This is the pulmonary circulation, where the gas exchange takes place. In the lungs carbon dioxide (CO<sub>2</sub>), a waste product of cells, is released from haemoglobin and oxygen (O<sub>2</sub>) is bond. The flow then continues via the pulmonary veins through the LA and LV. The blood leaves the heart via the aorta. The aorta is the largest single blood vessel in the body. It branches off in numerous arteries and arterioles to carry the oxygenated blood to the head, internal organs and upper and lower extremities. This part of the loop represents the systemic circulation.

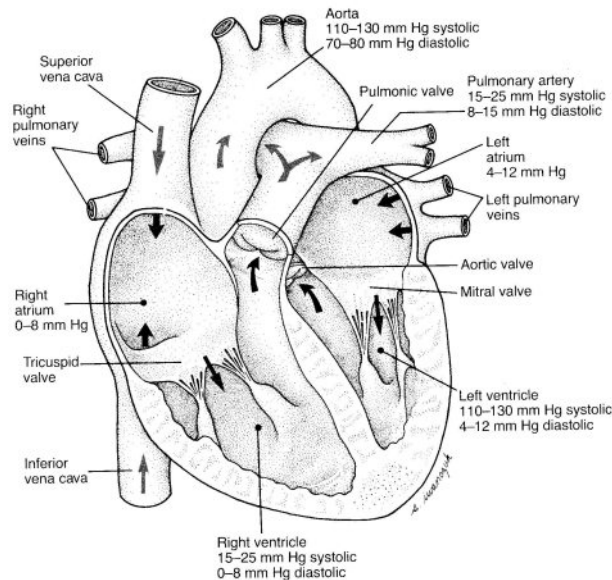


I-I. Schematic drawing of blood flow direction in the human heart and vascular system [1].

### I.1.2. *Anatomy of the heart*

The heart is divided in four chambers, two atria and two ventricles. There are also widely used expressions “right” and “left” heart referring to “right atrium

(RA) and ventricle (RV)” and “left atria (LA) and ventricle (LV)”. The upper chambers (atria) are anatomically separated from the ventricles by a fibrous ring. Each chamber of the heart has a sort of one-way portal embedded in the fibrous ring, the valve, which prevents blood from flowing backward. The valves consist of two or three leaflets. There are four valves in the heart: the tricuspid (three-leaflet) and bicuspid (two-leaflet) valves separate the RV and LV from RA and LA respectively. The semilunar (also called the pulmonary) tricuspid valves precede the entry towards the lungs and aortic valve towards the aorta. If these valves do not function appropriately, several complications may occur. Figure I-II illustrates the heart with its valves, where arrows indicate the direction of the blood flow in a healthy human body.



I-II. Anatomical scheme of the human heart with typical pressure values for an adult. The arrows indicate blood flow directions [2].

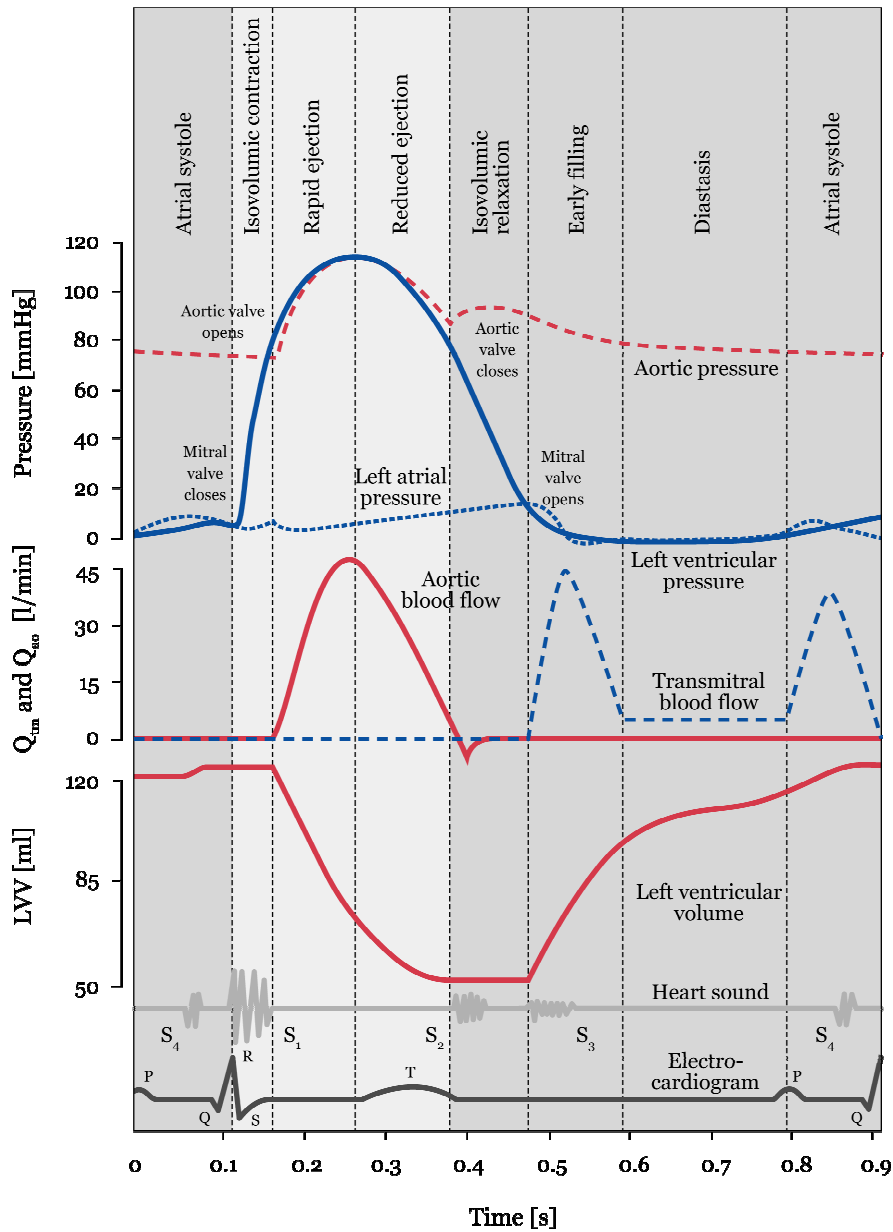
Veins from the head and upper body coalesce into the superior vena cava, which directs the blood to the RA. The second vein is the inferior vena cava, which rises from the junction of the veins leaving the legs and lower torso. The RA receives de-oxygenated blood and passes it to the RV. The pulmonary valve, separating the RV from pulmonary artery is closed, allowing the RV to be filled. The closure of the tricuspid valve prevents blood from flowing back into

the RA. The pulmonary vein is the blood vessel transporting oxygen-rich blood from the lungs to the LA. The LA passes the blood through the mitral valve into the LV. The LV is the most muscular part of the heart, which is pumping the fluid through aorta to the entire body. The structure and functions of the heart valves will be described in detail in I.1.5.

### I.1.3. *The cardiac cycle.*

A single “heart beat” consists of two phases, the diastolic and the systolic phase. During the diastolic phase the heart muscle is “relaxed” and blood flows into the chambers from the body and lungs. The tricuspid and the bicuspid valves are open allowing the ventricles to fill with blood (the pulmonary and aortic valves are closed during diastole). The ventricles then contract during the systolic phase and pump blood into the lungs and body. At this time the pulmonary and aortic valves open.

For the right heart, the exact same phases occur but at lower pressures (figure I-III). During the isovolumic contraction of the LV, pressure rises from 0 to around 80 mmHg (diastolic blood pressure).



I-III. An example of a cardiac cycle for a heart rate approx. 75bpm. Plots depicted from top to bottom accordingly: LA and LV pressure; aortic volume flow; LV volume; acoustic of heart and Electrocardiogram (ECG) [3]. (The pressure and volume flow values may vary according to the size and sex of the human body).

During this phase both the aortic and mitral valve are closed. When the ventricular pressure rises above diastolic aortic pressure (~80 mmHg), the aortic valve opens and blood is ejected from the LV into the aorta. The aortic

velocity profile shows a maximum velocity of about 1 to 1.4 m/s. The ventricular and aortic pressures further rise up to 120 mmHg. The diastolic portion of the heart cycle can be subdivided into four phases: (I) isovolumic relaxation, (II) rapid or early filling (E-wave), (III) diastasis (L-wave) and (IV) atrial contraction (A-wave). In the first phase, between aortic valve closure and mitral valve opening, LV pressure drops almost exponentially from the aortic pressure level to a pressure of a few mmHg existing in the LA. The next phase, i.e. early filling (E-wave), begins when pressure in the LV falls below that in the LA, causing the mitral valve to open and the LV to start filling. The third phase is diastasis (L-wave), with little extra filling of the LA. The fourth phase or atrial contraction of the LA (A-wave), contributes for an extra 15 to 25 % of the LV filling [4]. In healthy hearts, the mitral velocity profile has a first peak of about 0.7 m/s (E-wave) in early diastole and a second increase of velocity 0.5 m/s following the LA contraction (A-wave) [5].

#### I.1.4. *Blood*

Blood is a suspension of blood cells in plasma. Blood plasma is a fluid, which contains many vital proteins including fibrinogen, globulin(s) and the human serum albumin. It contains three kinds of blood cells: red and white cells and platelets. The rich composition of blood is also the reason for multitude of functions. Besides the gas exchange ( $O_2$  and  $CO_2$ ) between the organism and environment, blood has a number of other functions:

- Supply of nutrients such as glucose, amino acids and fatty acids (dissolved in the blood or bound to plasma proteins)
- Removal of waste such as carbon dioxide ( $CO_2$ ), urea and lactic acid
- Immunological functions, including circulation of white cells, and detection of foreign material by antibodies
- Messenger functions, including the transport of hormones and the signaling of tissue damage

- Regulation of body pH
- Regulation of core body temperature

The human blood is, generally speaking, a very complex multiphase fluid. Due to its complexity, the physical properties may vary according to the change of internal parameters like blood temperature [6; 7], hematocrit [8] and diameter of the vessel [9]. Blood is considered as a non-Newtonian fluid, which is a fluid changing its viscosity with the applied strain rate. The blood properties also vary according to the environment (e.g. humidity, heat, pressure) [10; 11]. The experimental simulations of the blood flow in this dissertation only concern the regions in right and left heart. Blood can be considered as a Newtonian fluid for the shear rates. Blood of a patient with an average hematocrit of 46 % [12] has a dynamic viscosity ( $\eta_{\text{blood}}$ ) of approximately 3.5 mPa.s [13] and a density between ( $\rho_{\text{blood}}$ ) 1052 and 1058 kg/m<sup>3</sup> [14].

#### I.1.5. *Heart valves*

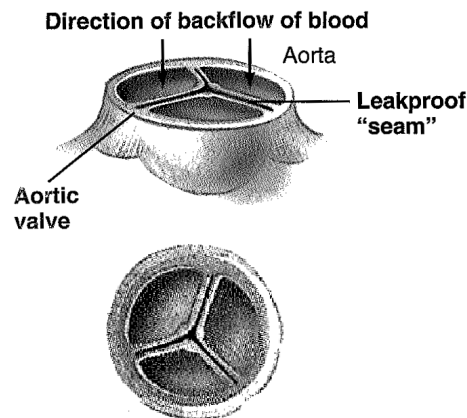
##### *I.1.5.1. Structure and function of the heart valves*

Cardiac valves have three functions: (1) preventing regurgitation of blood from one heart chamber to another, (2) permitting rapid flow without imposing important resistance to the flow, and (3) withstanding high-pressure loads. These valves work by several principles related to physics. However, the discussion here is limited to pressure gradients. Fluid flows from areas of high pressure to areas of low pressure. In the heart the valves open and close in response to pressure gradients, i.e., valves open when pressure in the preceding chamber is higher and close when the gradient reverses. These one-way valves are important in ensuring that the blood flows in the proper direction.

The atrioventricular valves have a mechanical support by means of muscles and tendons. The edges of the leaflets of these valves are fastened by tough, fibrous cords of tendon-like tissue, the chordae tendineae. These cords extend

from the edge of each cusp and attach to small, so-called papillary muscles, which protrude from the inner surface of the ventricular walls. When the ventricles contract, the papillary muscles also contract, pulling downward on the chordae tendineae. This pulling exerts tension on the closed valve cusp to hold them in position, thus helping them to remain tightly sealed in the face of a strong backward pressure gradient [1].

The semilunar valves differ strongly anatomically from atrioventricular valves, even though their function is principally the same. As the expression indicates, they are shaped like half a moon. These valves don't have any mechanical support by means of tendons or muscles which would help them to avoid reverting in a way as it present by atrioventricular valves. Therefore, it is clear that their structure has to be different. The semilunar valves consist of three equal leaflets. Once the valve is closed, the leaflets are forming a pocket-like geometry blocking the entrance from the ventricle to a vessel (figure I-IV).



I-IV. Aortic valve [1].

Due to their structural design, the prevention from reverting the leaflets into the ventricle is guaranteed by the form of the leaflets. A portion of each leaflet is overlapping the neighboring leaflet thereby sealing the separation between the ventricle and large artery.

### *1.1.5.2. Valvular diseases*

Heart valve treatments are required in case of disease or partial dysfunction. Valvular heart disease (VHD), a non-specific, all-encompassing name for various diseases affecting the heart valves, can be classified into two categories: congenital and acquired. Congenital valvular heart disease is present from birth, and occurs in about 0.6% of non-premature live births [15]. It can be caused by chromosomal abnormalities, but in most cases the causes of congenital valvular disease remain unclear. Acquired valvular heart disease is much more common than congenital VHD [15].

Acquired VHD is generally caused by a disease or injury to the heart. An autoimmune disease related to the streptococcus virus, acute rheumatic fever is a serious illness that can cause forms of VHD such as valvular stenosis (hardening of the valves). Other cases of VHD include tumors of the heart muscle, injury to the chest, lupus and many others. Some of the disease may take even more than 20 years to cause the patient noticeable problems. However, there are people who can live with a diseased valve the whole life [16] and never being diagnosed for valve dysfunction. In severe cases the only treatment for the diseased valve is valvular replacement or repair surgery.

The possible consequences of heart valve dysfunction can be improper closing and leak of blood into another quadrant of the heart (*regurgitation*) or not proper opening, because the valves are hardened (*stenosis*). Mitral valvular regurgitation causes the heart to work less efficiently and usually results in an enlargement of the heart chambers because there is more blood to pump to compensate for the leaking blood. However, in severe cases the heart is not strong enough to compensate for the efficiency loss and it results in congestive heart failure.

Valvular *stenosis* causes higher blood pressure in the heart because blood builds up behind the closed valve and forces the cardiac muscle to work harder to pump the blood through the heart. The heart usually compensates for that

by growing a thicker layer of muscle. In extreme VHD cases, valvular replacement or repair surgery is necessary.

A special interest for the experiments of this dissertation was to simulate the in vivo situation where the surgical replacement of the native valve is taking place by a prosthetic heart valves (PHV). The implantation of the mechanical prosthetic heart valves is still common treatment for the patients with severe VHD, however, many stems related to fluid mechanics have been reported in literature, rendering a PHV inappropriate for a life-long duty in a patient [17]. Therefore, it is important to improve the design of the mechanical PHV. To achieve this, it is necessary to quantify the fluid dynamics of the existing ones, which was one of the goal of this dissertation.

#### *1.1.5.3. Prosthetic heart valves*

The first implantation of a prosthetic heart valves (PHV) was successfully performed in 1952 by Charles Hufnagel [18].

More than 80 different models of artificial valves have been introduced since 1950 [19], but only about 50 have been used in the past 40 years [17]. Prosthetic valves are either mechanical or fashioned from biological tissue (e.g. from pigs). The latter are so-called *bioprostheses* or *heterografts*. The human biological prostheses are called *homografts*. Table I-1 [17] lists PHVs commercially used before 2004. The various PHVs differ from each other with respect to several characteristics, including durability, thrombogenicity and fluid dynamic properties. The properties related to fluid dynamics performance are principally depending on the valve geometry and architecture. The firstly implanted caged-ball valve by Hufnagel is nowadays not used anymore in clinics due to its poor performance and unsatisfactory clinical outcome. The designers of heart valves inclined either to a *monoleaflet* or a *bileaflet* model which were widely used up to 2002 [20]. *Monoleaflet* valves exist in two types: an elevating disc and a tilting disc valve. Only a tilting disc valve is well

accepted in clinics and some prototype trials have been performed recently [21]. Presently, however, the mostly implanted PHV are bileaflet models.

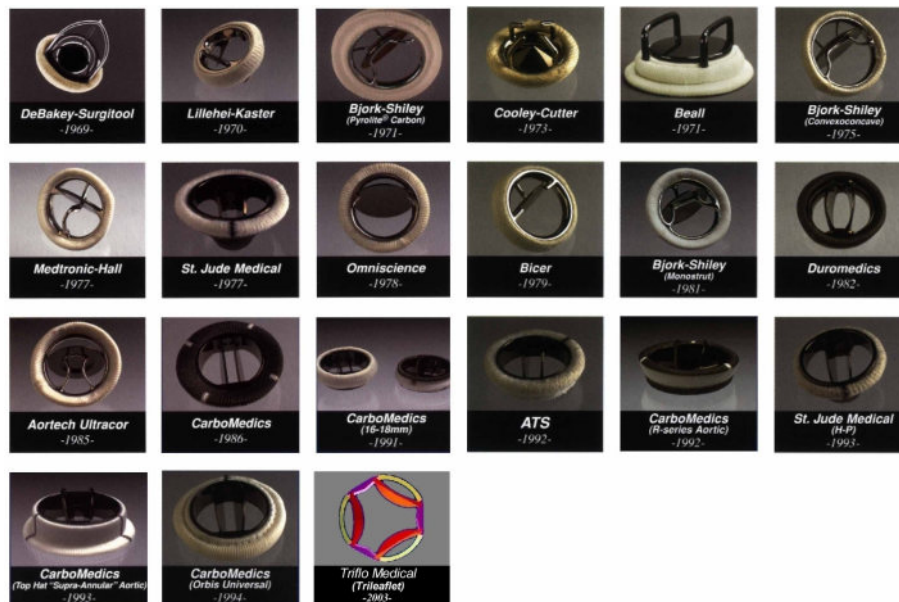
<b>Mechanical prostheses</b>	<b>Bioprostheses</b>
<ul style="list-style-type: none"> <li>• Monoleaflet Bjork-Shiley monostrut mechanical prosthesis</li> <li>• Sorin Monoleaflet allcarbon mechanical prosthesis</li> <li>• Medtronic-Hall mechanical prosthesis</li> <li>• Omnicarbon mechanical prosthesis</li> <li>• Ultracor mechanical prosthesis</li> <li>• Bileaflet St. Jude Medical Standard mechanical prosthesis</li> <li>• St. Jude Medical Haemodynamic Plus mechanical prosthesis</li> <li>• St. Jude Medical Regent mechanical prosthesis</li> <li>• CarboMedics mechanical prosthesis</li> <li>• Edwards Tekna mechanical prosthesis</li> <li>• Sorin Bicarbon mechanical prosthesis</li> <li>• ATS mechanical prosthesis</li> <li>• ON-X mechanical prosthesis</li> <li>• Medtronic Advantage mechanical prosthesis</li> <li>• Medtronic Parallel mechanical prosthesis</li> <li>• Edwards MIRA mechanical prosthesis</li> </ul>	<ul style="list-style-type: none"> <li>• Stented porcine Hancock porcine bioprosthesis</li> <li>• Carpentier-Edwards porcine bioprosthesis</li> <li>• Carpentier-Edwards Supra-A</li> <li>• Hancock II porcine bioprosthesis</li> <li>• Hancock Modified Office porcine bioprosthesis</li> <li>• St. Jude Medical-Biocor porcine bioprosthesis</li> <li>• St. Jude Medical-Bioplant porcine bioprosthesis</li> <li>• Medtronic Mosaic porcine bioprosthesis</li> <li>• Aortech Aspire porcine bioprosthesis</li> <li>• Labcor porcine bioprosthesis</li> <li>• St. Jude Medical Epic porcine bioprosthesis</li> <li>• CarboMedics Synergy St porcine bioprosthesis</li> <li>• Stented pericardial Carpentier-Edwards Perimount pericardial bioprosthesis</li> <li>• Mitroflow Synergy PC pericardial bioprosthesis</li> <li>• St. Jude Medical Biocor pericardial bioprosthesis</li> <li>• Sorin Pericarbon More pericardial bioprosthesis</li> <li>• Labcor pericardial bioprosthesis</li> <li>• Stentless porcine St. Jude Medical-Toronto SPV stentless porcine bioprosthesis</li> <li>• pericardial Medtronic Freestyle stentless porcine bioprosthesis</li> <li>• Cryolife-O'Brien stentless porcine bioprosthesis</li> <li>• Cryolife-Ross stentless porcine pulmonary bioprosthesis</li> <li>• Edwards Prima Plus stentless porcine bioprosthesis</li> <li>• Sorin PericarbonTM Freedom stentless pericardial bioprosthesis</li> <li>• Aortech Aspire stentless porcine bioprosthesis</li> <li>• St. Jude Medical Biocor stentless porcine bioprosthesis</li> <li>• Labcor Stentless Porcine Bioprosthesis</li> <li>• St. Jude Medical QuattroTM stentless mitral bioprosthesis</li> <li>• Shelhigh skeletonized super-stentless aortic porcine bioprosthesis</li> <li>• Shelhigh porcine pulmonic valve conduit</li> </ul>

Table I-1 Cardiac valve prostheses that have been introduced over the past 40 years [17].

Normally, mechanical PHVs are very durable and last at least 20 to 30 years [22; 23]. In contrast, bioprosthetic prostheses fail after 10 to 15 years in many cases[19]. Nevertheless, the mechanical PHVs don't achieve natural flow quality, moreover, the blood damage also due to the interactions of the leaflets,

hinges and housing of the valve is considerably high. However, the outstanding durability of the mechanical PHV is a benefit, which stimulates to improve the designs in order to bring the quality of the flow as close as possible to natural conditions.

The mechanical PHV are divided to a few categories according to the principle design. In figure I-V several design are shown. Caged ball valves have entrapped a sphere in monoleaflet tilting disc, elevating disc, bileaflet and trileaflet valves.



I-V. Examples of prosthetic mechanical valves [24].

To improve those properties, engineers need to clearly understand the conditions to which a PHV is exposed when working inside a heart. In this dissertation several cases are presented (Chapter V, VI, VII), where Particle Image Velocimetry (PIV) was applied to investigate the fluid dynamics behind PHVs and demonstrate their characteristics among different PHVs to the potential designers. Red blood cell damage (haemolysis) and thromboembolism are the main complications associated with the implantation of mechanical artificial heart valves in human beings. A serious complication associated with haemolysis is a thrombus formation. It can be related to high shear stress that

can be generate and, in addition, contact to foreign surfaces to which are blood cells exposed [19].

#### I.1.6. *Conclusion*

The first chapter of part A briefly introduced cardiovascular anatomy and its function. It was meant to point out the important role of blood as a carrier of essential substances, which flows through the heart and vascular system. In some treatments of diseases, invasive artificial devices are used in the heart or cardiovascular system. This procedure will have a direct impact on the blood flow and may lead to further complications during the treatment. Therefore, it is important to understand the impact of the treatment procedure (e.g. heart valve replacement) in order to determine the weak aspects. This could lead to improve the design of artificial devices or develop new prototypes of PHV.



## **I.2. Introduction to Central Venous Hemodialysis Catheters**



### I.2.1. Vascular access for extracorporeal therapy

The definition of an extracorporeal therapy, such as by an artificial kidney support system, is a procedure in which blood is taken from a patient's circulation to have a process applied to it in the circuit outside the body (extra corpus) before it is returned to the circulation. As such, a means to extract and return blood from the patient – a vascular access – has to be introduced. This access should be easily available for connection to the extracorporeal circuit and should provide the blood flow. After treatment, disconnecting should be possible relatively rapid. In addition, complication rates like bleeding, thrombosis and infection should be low and discomfort for the patient minimal. At present, different types of vascular access are available.

Fistulas can be placed over the whole body, but by preference in the upper extremity because of the lower complication rates [25]. After a period of maturation of about 6 weeks, the connecting vein in the AVF becomes more prominent and thick-walled. This process is called 'arterialisation'. Now an easy repetitive access to the circulation can be obtained by puncturing the dilated veins.

However, some patients develop a very acute need for extracorporeal therapy, such as patients with acute or end-stage renal disease. These patients often cannot rely on an AVF as a means of vascular access due to slow maturation of their fistula, combined the sometimes late referral of these patient to extracorporeal treatment [26]. Additionally, it may be impossible to create a suitable arteriovenous shunt in a patient. This makes the central venous catheter (CVC) a prominent second type of vascular access.

A catheter is generally a cylindrical tube with one or more lumens, that can be inserted into a blood vessel. A catheter inserted into the large veins leading to the right atrium (Superior Vena Cava – SVC; Inferior Vena Cava – IVC) is called a central venous catheter. The idea to use central venous catheters as a vascular access method for extracorporeal therapy stems from the successful

use in chemotherapy. Cannulation of the subclavian vein for dialysis purpose was first described by Erben et al. in 1969 [27]. They used two single lumen catheters inserted in both vena subclavia, both in the same vena subclavia, or one in a subclavian vein and the other in the femoral vein. In the beginning of the 1980's, double lumen catheters were introduced. Initially, this consisted simply of a blood drawing ('arterial') cylindrical cannula and a coaxially placed ('venous') cannula that returned cleansed blood to the circulation, which were replaced after each dialysis session. Catheter technology further evolved towards catheters with two lumina separated by a septum, and further to double lumen catheters with two separate lumina side-by-side.

In addition to its critical role in acute vascular access, central venous catheters soon became a prominent player as a more long-term, chronic means of vascular access due to several advantages as easy insertion, universal application (functional in nearly 100 % of patients) and minor hemodynamic stress to the cardiovascular system as compared to AVF.

The most recommended insertion site for chronic catheter placement is via the right internal jugular vein. With the body of the catheter in the superior or inferior caval vein, the catheter tip is either located in the caval vein itself, at the junction of the caval vein with the right atrium, or completely in the right atrium.

Complications associated with catheter use can be classified in two categories: immediate or early complications, and delayed complications. Immediate complications occur within minutes or hours of insertion of the catheter

The onset of delayed complications normally happens after several days's use of the catheter. The major delayed complications can be divided in three groups: (a) infection, (b) thrombosis, and (c) stenosis.

A satisfactory performance catheter design is characterised by a homogeneous inflow and outflow of blood. Zones with low blood velocity or stagnant zones should be avoided as this may promote blood clotting.

Many catheter designs are marketed nowadays. However, the geometry and tip design of catheters have been determined mainly by methods of trial and error. No real benefit of one catheter type over another has been found in studies comparing in vivo catheter blood flow rate, infection rate, or catheter survival. However, very little fundamental research has been performed to assess the influence of specific design features of catheter tip designs (such as side holes), on the catheter's hemodynamic performance. Until present, knowledge of the internal flow and shear stress distribution inside central venous catheters, and insight in how the tip design influences these important parameters of clinical and hemodynamic performance, is non-existent. The presented results in chapter VIII. may lead to a better understanding of performance among different design catheter. Results may be used to design a new catheter type.



## II. Particle Image Velocimetry

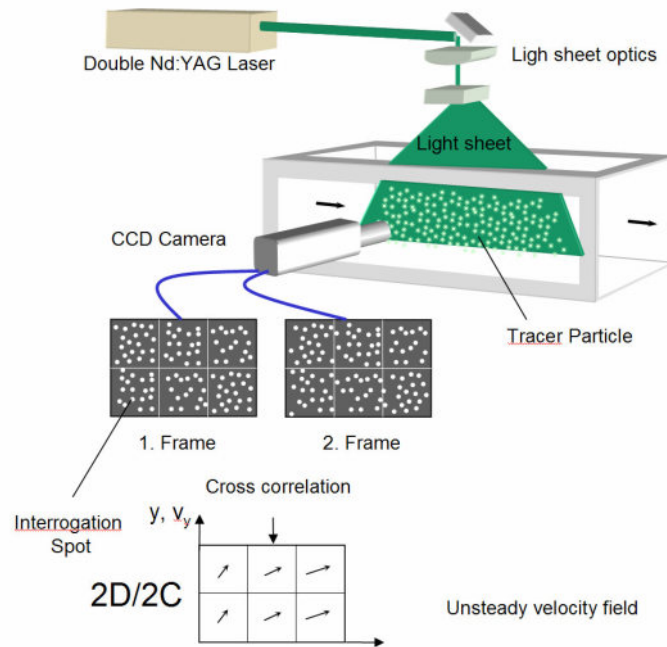


## II.1. Introduction

Particle Image Velocimetry (PIV) is one of nowadays frequently used non intrusive method for visualizing the flow velocity distribution in fluids. PIV is an optical technique based on image processing. It uses a planar approach where the investigated plane of the measurement section is illuminated by a sheet of light. The fluid contains particles, which were added to the fluid prior to measurement. A camera is recording the illuminated particles crossing the sheet of light. The images of the particles are acquired in sequence in discrete time steps. Comparing the position of the particles among the related images, a displacement can be determined and over a known discrete time step the velocity in magnitude and direction can be calculated.

*PARTICLE* stands for the tracer particles inserted in the fluid, *IMAGE* refers to a media, containing the measured signal – back scattered light from the particles and *VELOCIMETRY* means measurement of the velocity of the particles.

Standard PIV is a technique, where two components of the velocity are determined in a two-dimensional plane. The *region of interest (ROI)* has to be illuminated by a powerful, pulsed and often monochromatic *light* source (e.g. Laser) two times within a short time interval. A *camera* acquires two images of the backscattered light from the particles synchronized to the illumination. By comparing the first and the second recorded particle image, a displacement of the particles can be recognized. The displacement between the particle images and the known time delay between the consecutive illuminations is resulting in a two component velocity vector. The experimental setup of a PIV system typically consists of several subsystems like: Laser, optics, particles, camera, synchronizer and software. The detailed information about the components of the PIV system as well as the description of the evaluation of the results will be explained in the following subchapters. The schematic set-up of PIV is demonstrated in figure II 1.



II-1. General PIV set-up, where the laser is illuminating the desired ROI in the flow. The CCD camera is recording particles on the 1<sup>st</sup> and 2<sup>nd</sup> image frame in a given time delay. Cross correlation function is calculating the velocity vectors according to the particle displacement comparing the interrogation spots of the 1<sup>st</sup> to the 2<sup>nd</sup> image frame.

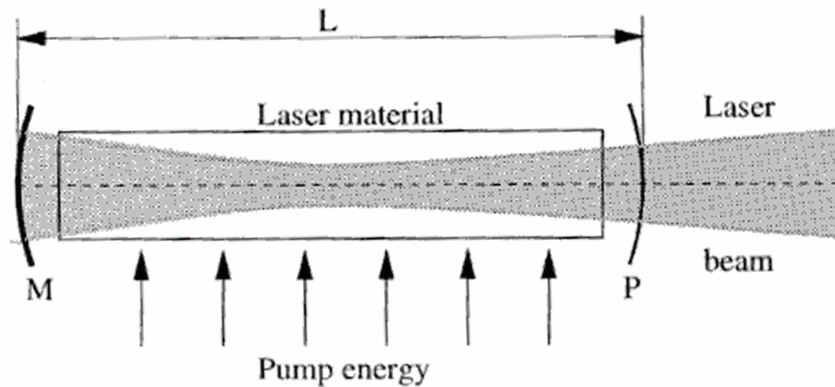
## II.2. Illumination of the ROI

The illumination in a planar arrangement is achieved by a thin light sheet (LS) inside the measurement section. This plane is defining the ROI together with the used camera in the measurement set-up. The ROI is illuminated twice with consecutive emitted light pulses in a chosen time interval. This process has to be perfectly time controlled. Pulsed lasers are very often used for PIV due to the following reasons: short pulse length in order to freeze the particle motion, high light energy to illuminate tiny  $\sim 1\mu\text{m}$  particles and monochromatic light to simplify the light sheet generation. The higher the pulse energy of the emitted light, the more intense the backscattered light from the particles. The maximum possible size of the ROI depends from the amount of laser energy used. The laser delivers a beam of a monochromatic light. This beam is shaped

into a plane of laser light of a few millimeters thickness by passing through an array of lenses called light sheet optics (LSO). The LSO is oriented in a way to illuminate the desired measurement plane of the ROI (figure II 1.).

### II.2.1. *Lasers.*

LASER, is an abbreviation for **L**ight **A**mplification by **S**timulated **E**mission of **R**adiation. It is an optical source that emits photons in a coherent beam. It has the ability to emit monochromatic light with high energy density. In figure II-II a typical general configuration of a laser is shown. As shown in figure II-II, every laser consists of three main components.



II-II. Basic parts of the laser [28]. Laser material, pump energy source and mirrors M and P.

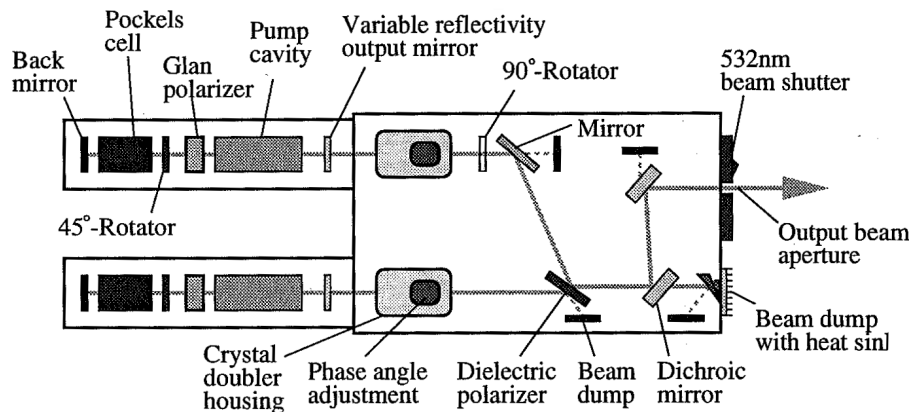
The *laser material* consists of an atomic or molecular gas, semiconductor or solid material. The *pump source* excites the laser material by the introduction of electro-magnetical or chemical energy and the arrangement of *mirrors (M and P)* allows an oscillation within the laser material. There are gas and solid laser material. For PIV solid lasers are mostly used [28].

#### II.2.1.1. *Neodym-YAG (Nd:YAG) lasers*

Nd:YAG (neodymium-doped yttrium aluminium garnet;  $\text{Nd:Y}_3\text{Al}_5\text{O}_{12}$ ) is a crystal that is used as a lasing medium.

Nd:YAG lasers are mostly used solid state lasers in PIV. The  $\text{Nd}^{3+}$  ion is incorporated in yttrium-aluminium-garnet (YAG) rod. To pump the energy a flash lamp (one or more) are surrounding the rod. Those lasers have high amplification and good mechanical and thermal properties.

Commercial lasers uses YAG rods up to 150 mm long with up to 10 mm diameters. The highest energy they can achieve per pulse is around 600 mJ. Besides energy, beam profile of a laser is another important parameter for PIV measurements. Ideally it needs to have Gaussian intensity distribution of the generated light in order to illuminate the ROI homogeneously over the entire area. Normally, the quality of the beam by Nd:YAG lasers reach only 80% of the Gaussian intensity distribution in the near (<20 mm) and around 95% in the far field (>10 m). However, these values can vary even among products of the same manufacturer. This is mostly due to the manual alignment of the mirrors surrounding the laser material, as the ones illustrated in figure II-II.



II-III. Double oscillator laser system with critical resonators [28].

There are various types of resonators with different types of mirror curvatures. In figure II-II confocal resonators are illustrated. In the pumping chamber the Nd:YAG rod and the flashlamps are located, surrounded by ceramic reflectors for efficient pumping of the laser rod. The output mirror has a plane surface featuring partially reflective coating towards the pump cavity. The opposite surface has an antireflection coating. The Nd:YAG laser only emits the

strongest wavelength, 1064 nm. Since there are advantages to operate with visible light, a crystal doubler implemented in the laser beam is changing the wavelength from 1064 to 532 nm. The wavelength of 532 nm is in the green range of the light spectrum. By including a quality switch (Q-switch) inside the cavity of the laser, it is possible to operate with short pulse lengths  $\sim 5-7$  ns. A Q-switch normally consists of polarizer, beam path correlating prism and a Pockels cell, which changes the polarization of the laser beam depending on the Pockels cell voltage. A Pockels Cell is a device which contains a photo refractive electro-optic fluid. When a voltage is applied to this fluid it can change the polarization or phase of the light beam [29]. Depending on the orientation of the fluid either the polarization can be altered or a phase change can be introduced. The lasers for PIV usually have two cavities to generate two separate beams with equal light intensity in a discrete controlled time interval. There is also an arrangement of mirrors to redirect the laser beams from both cavities to the same aperture to achieve an overlap of the two beams.

The case studies presented later in chapters IV., V., VIII. have been carried out by using Solo PIV I laser (New Wave Research, Fremont). It is a double cavity solid state laser with a maximum energy of 30 mJ/pulse per cavity. Technical details are listed in [30].

#### *II.2.1.2. Neodym-YLF (Nd:YLF) lasers*

Solid-state lasers using  $\text{LiYF}_4$  crystal as the matrix material, doped with neodymium have higher efficiencies at higher repetition rates. Nd:YLF (Neodymium-doped yttrium lithium fluoride) laser can have wavelength outputs of 1.313  $\mu\text{m}$ , 1.053  $\mu\text{m}$ , 527 nm, 523 nm, 351 nm, or 263 nm. The cross-section of YLF is about half compared to YAG rods. The energy storage limit is inversely proportional to the ratio of the stimulated emission cross-section. Therefore higher densities are obtained in the lower cross-section materials [31]. Nd:YLF lasers are capable of reaching higher repetition rates around 10 kHz by having higher efficiency in the range of 1~8 kHz repetition rates

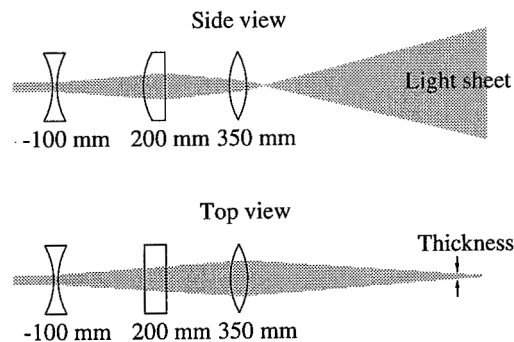
compared to Nd:YAG systems. In our studies presented in chapters VI. and VII. a New Wave Pegasus laser was used [32].

### II.2.2. *Laser safety*

All lasers used in PIV have the capability of causing burn marks on the skin. According to the emitting light power, the lasers are classified in 5 major classes [33]. The most severe safety concern is eye injury. The property of the lasers that is of primary concern with regard to eye hazard is their combination of high power density and focus of a beam by the eye lens. The eye lens focuses the laser beam to a spot on a retina and the high energy response will burn light sensitive cells. The collimated parallel laser beam is dangerous to the eye also over long distances. Retinal damage is possible in the wavelength spectrum between 400 to 1400 nm. In particular, radiation between 400 and 700 nm is the most hazardous, because the spectral transmission of the human eye is for this wavelength the highest [31]. Laser used in PIV operates in latter mentioned interval of wavelength.

### II.2.3. *Light sheet optics (LSO)*

In theory, assuming the laser beam uniformly round in endless distance, a single cylindrical lens would be sufficient to create LS. However, the beam is normally divergent and therefore the LSO is an array of lenses arranged in an axis of laser light beam. An example of the lenses array is demonstrated in figure II-IV.



II-IV. LSO using two spherical lenses and one cylindrical lens [28].

The standard models include in a single unit a focal distance adjustment to set the LS thickness in the illumination plane. A cylindrical lens generates the LS in various angles. The collimator is used to project the beam waist of the laser beam into the ROI, in order to generate a LS with appropriate thickness. The quality of the light sheet is an important issue when illuminating the ROI. Ideal quality is achieved when there is equal intensity of the illumination over the entire ROI. Due to the Gaussian distribution of the laser beams, the highest intensity would be in the middle of the created LS. Therefore, normally, the LS size is always larger than the desired ROI. Moreover, the laser beam divergence has also an impact on the quality of the LS, thus lasers with small divergence angle are preferred.

Guiding the laser beam to the LSO plays an important role. The best way to avoid energy loss of the generated laser beam is to mount the LSO directly on the laser head. The laser head then would be mounted close to the measurement section to illuminate the desired ROI. This setup is sometimes impossible due to space limitations. Moreover, the ROI vicinity has to stay free of obstacles to allow clear view for the cameras observing the ROI. Moreover, most laser heads are big, bulky and heavy boxes - quite hard to handle.

The second option is to mount the laser head on a special optical table or bench together with an array of precisely adjusted mirrors which can reflect the laser into the LSO. This setup is easier to handle but the disadvantage is the safety

of the environment. In addition it is quite difficult to precisely adjust the mirrors and maintain the same conditions for several days or weeks. Normally high reflective surface coated mirrors are utilized, but even in that case - depending on the number of mirrors- there are certain energy losses.

Using an optical fiber could be an elegant solution for latter difficulties because the flexibility of the entire set-up is maximized. In most of the cases there are no fibers available for standard PIV lasers. Here the pulse length is the limiting factor: With 5-7ns pulse length and  $\sim 30\text{mJ/pulse}$  the damage threshold of most of the available fibers is reached. The great disadvantage is also the loss of the energy proportional to the small aperture diameter of the fiber and its length. Moreover, the divergence of the laser beam at the fiber output is enormous and needs a specially designed LSO to gain a good quality LS.

The method used in experimental cases described in part B is using an articulated arm. This solution is a combination of the advantages of the surface coated high reflective mirrors and the flexibility of the fiber, but still limited due to the solid tubing. The articulated mirror arm (figure II-V) is an integrated light guide for delivering controlled laser illumination to the LSO.



II-V. Articulated mirror arm as interface between the laser head and LSO [34].

In addition, the optical alignment of the laser-arm assembly is highly stable. The arm interfaces to Nd:YAG PIV lasers, both mini- and large models, assembled on static or mobile bench units. Such a light arm can safely deliver high power laser pulses to the experiment [34].

#### II.2.4. *Particles*

First of all, particles or seeding should match the density of the fluid in order to truly follow the fluid motion. Moreover, the size of a particle should be in correspondence of the measured ROI and thus it should have a size of a few pixels on the image.

However, if the particles are too small the back scattered light might be too low to get a satisfying signal to noise ratio. There are several parameters for the right choice of particles to visualize the flow in particular fluids to ensure good signal to noise ratio. In most applications a compromise has to be found. The main properties of the particle to be considered are: size, shape, scattering properties, material, density and chemical stability.

Tiny particles of  $1\mu\text{m}$  or less (e.g. droplets of oil) needs to be utilized in gas flow applications. Therefore a high power light source for illumination is required in order to detect the light scattered by the tiny tracer particles . In liquid flows larger particles can usually be accepted which scatter much more light. Thus, light sources of considerably lower peak power can be used here.

Major measurement errors arise from the influence of gravitational forces once the density of the particles  $\rho_p$  does not match with the density of the fluid  $\rho_{fluid}$ . The impact also strongly depends on the size of the particles  $d_p$ . According to *Stokes drag law* it is possible to calculate gravitationally evoked velocity  $u_g$  (Equation II.1) under acceleration  $g$ . We assume the particles being spherical, added to a fluid having a dynamic viscosity  $\eta$  at very low Reynolds numbers [28].

$$u_g = d_p^2 \frac{(\rho_p - \rho_{fluid})}{18\eta} g \quad (\text{II.1})$$

In analogy to equation (II.1) we can estimate the velocity lag  $u_s$  of a particle in a continuously accelerating fluid with acceleration  $a$ :

$$u_s = u_p - u_f = d_p^2 \frac{(\rho_p - \rho_{fluid})}{18\eta} a \quad (\text{II.2})$$

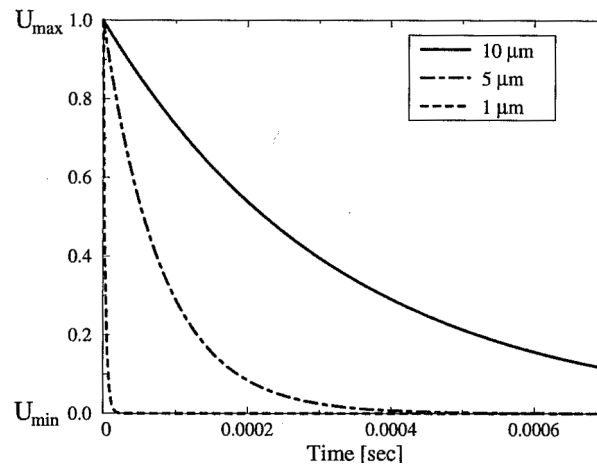
where  $u_p$  is the velocity of the particle and  $u_f$  is the velocity of the fluid. The step response of the particle velocity  $u_p$  follows an exponential law if the density of the particle is much greater than that of the fluid:

$$u_p(t) = u_f \left[ 1 - \exp\left(-\frac{t}{\tau_s}\right) \right] \quad (\text{II.3})$$

with the relaxation time  $\tau_s$  given by:

$$\tau_s = d_p^2 \frac{\rho_p}{18\eta} \quad (\text{II.4})$$

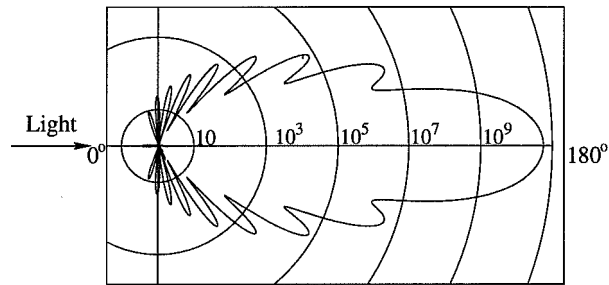
Once the fluid acceleration is not constant or at high Reynolds number, the motion of particles becomes much more difficult to solve. However, the relaxation time remains a convenient parameter for the tendency of particles to attain velocity equilibrium within the fluid. In figure II-VI the time response result of particles with different diameters present in a strongly decelerating air flow is illustrated.



II-VI. Time response of oil particles with different diameter in decelerating air flow[28].

It is easier to find solid particles of different sizes and matching the density of e.g. water than e.g. air, because the density is much higher. Different materials can be chosen like polystyrene, aluminum, glass or many kinds of synthetic materials which have good scattering properties. The size and density are parameters, which according to equation II.2, depend on each other. The latter means, that if  $\rho_p$  is much higher than  $\rho_{fluid}$ , the size of the particles must be small enough to follow the flow of the fluid with nearly no velocity lags. Compromises have to be made in order to choose optimal particles for the measurements.

The intensity of the scattered light depends not only on the size and material of the particle but also on the orientation with respect to the incident light and its polarization. Small particles scatter less polarized light [35], but for most of the standard PIV applications small (1-50 $\mu\text{m}$ ) particles are preferred due to the small velocity lag. To increase the intensity of scattered light, high power lasers are used. Figure II-VII illustrates the scattering behavior of a 1 $\mu\text{m}$  glass particle in water according to MIE's scattering theory. A detailed description of the scattering behavior of small particles is given in literature [36].

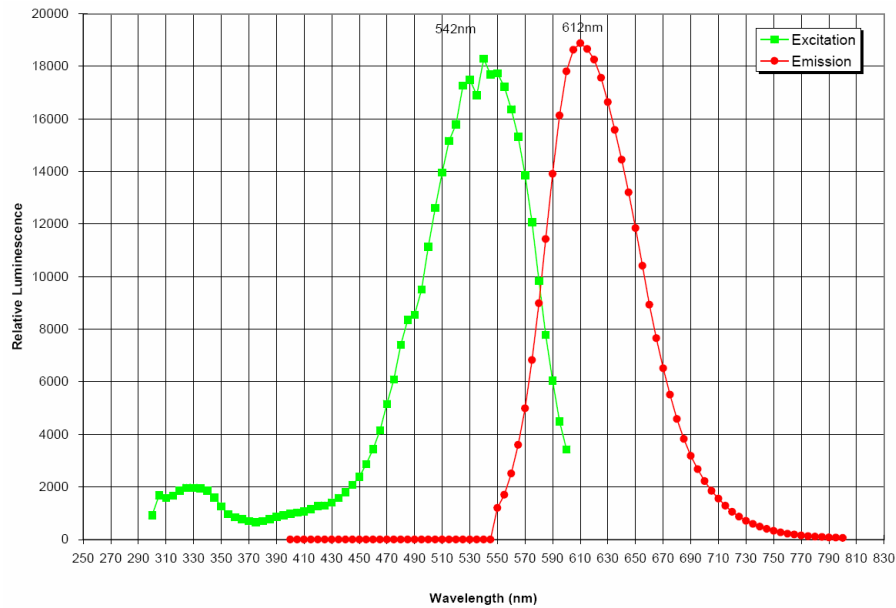


II-VII. Light scattering of 1  $\mu\text{m}$  glass particle in a water illuminated by 532 nm wavelength of the light [28].

Even though forward scattered light has the highest intensity, in standard PIV a  $90^\circ$  observation angle is typical because of the optical setup of laser and camera. The backward scattered light can be acquired in some special cases of Stereo PIV applications, where the cameras are observing the particles under an angle between  $10^\circ$  to  $80^\circ$ . There is a certain limitation in using larger particles in order to increase the light scattering, because the large particles might not follow the fluid flow but will act as a second phase in the fluid. Hence the measured movement of the particles differs from the actual flow.

Depending on the material or coating of the particles the scattered or fluorescent light might have the same or different wavelength. Fluorescent particles with e.g. Rhodamine-B coating illuminated by a green light send back red light. The benefit of having scattered light from the particles in a different wavelength is related to the possibility of avoiding the reflections of obstacles illuminated within the ROI. This is achieved by placing a band-pass filter in front of the CCD sensor of a camera which is filtering the wavelength of the laser and only allow the wavelength of the light produced by fluorescent particles to pass.

In figure II-VIII a spectrum is plotted of the ratio between excitation and emission wavelength of Rhodamine-B coated fluorescent particles later used.



II-VIII. A graph of a ratio between the spectrum of excitation and emission wavelength of Rhodamine-B coated micro spheres in a water [courtesy of Duke Scientific Corporation].

### II.3. Signal recording

At the early stage of PIV analog devices have been used for image recording. Photographic film has a very high spatial resolution - 100 line/mm for T-Max and 300 line/mm for Technical Pan on 24x36 mm, or even 100x125 mm films. In comparison, the resolution of digital cameras was typically 500x500 pixels. However, digital cameras are using a very precise grid of pixels compared to random locations of grains on a film. Clever methods were developed to enhance the accuracy of the interrogation of digital images. Moreover, the resolution of digital cameras increased rapidly to 1,000·1,000 pixels, and currently 11-megapixel cameras are essentially equivalent to 100 line/mm 35 mm film [37].

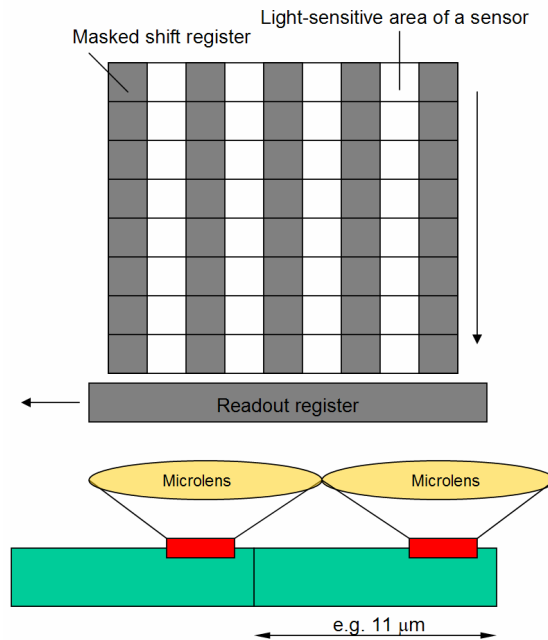
This step from analog to digital recording was one of the most important changes in the PIV technique together with the availability of smaller laser systems. This change profoundly influenced the usability and, hence, the popularity of PIV. Of course, many researchers had been using digital cameras

in preference to film for years. For example, film recording was seldom used in Japan. But, in the early 1990s, several investigators, most notably Willert and Gharib [38] and Westerweel [39], published results indicating that the low resolution of digital cameras was not as serious an issue as others had supposed, and that digital PIV could be accurate enough to provide useful results. The advantages of digital cameras are especially the possibility of shutter timing control, digital storage media, faster measurement frequencies and double frame acquisition. The digital enhancement of PIV made it possible to measure high velocity flows where pulse separations in the order of a couple of microseconds is required [37].

### II.3.1. *CCD Cameras*

A charge-coupled device (CCD) is an image sensor, consisting of an integrated circuit containing an array of linked, light-sensitive capacitors. It converts the light into an electric charge. The individual CCD cells are the so called “pixels” which stand for picture elements. Normally the arrays are in a rectangular form and the pixels are squares. The classical CCD pixel array building a complete sensor is schematically drawn in figure II-IX. For PIV it is important to acquire a pair of images in a very short time interval, so that the particle displacement is around 10 pixels. In some cases it can be even greater, if the cross correlation (chapter II.4.) between the images is still possible. The read-out time of a conventional CCD is in the order of a few milliseconds, whereas the time delay in PIV is in the order of microseconds. Therefore special CCD sensors are used in cameras designed for PIV. There are two sensors suitable for PIV: full-frame interline transfer CCD (figure II IX) or a frame transfer (figure II-X). The interline transfer CCD sensor is consisting of pixel rows sensitive to the light and masked rows. On the light sensitive pixels the signal is recorded and afterwards it is shifted to the masked rows. Consequently the signal will be serially passed to read out register. Because of the small size of active sensor surface compared to complete size of the sensor, micro lenses are

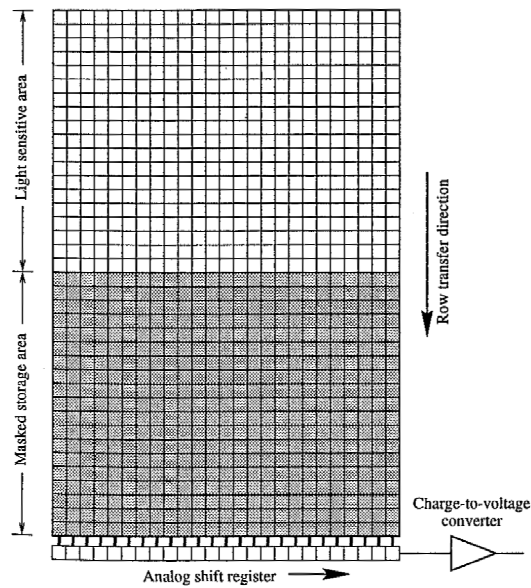
embedded in front of the pixels, to focus the light only on the light sensitive part of the surface.



II-IX. Scheme of a Typical CCD Interline-Transfer-Sensor geometry.

When the complete information from all rows is readout, another image can be taken. The readout time varies among different manufacturers of CCD cameras but depends strongly from the resolution.

A frame transfer CCD (figure II-X) is consisting of equal full frame CCD (figure II-IX) but only one half of the sensor is exposed. Once the image is recorded, the signal is rapidly - about  $1\mu\text{s}$  per row - transferred to the other masked half of the CCD sensor. Then the camera is able to record another image, while in the masked part of the CCD sensor the read-out of the signal takes place.



II-X. Frame transfer CCD layout [28].

Such a CCD can record two consequent images in a very short time delay – the so called double shutter mode [28]. Certainly, another pair of images can be acquired, once both previous are completely downloaded from the masked sensor.

More common are full frame interline transfer CCD sensors where each pixel has a neighbouring masked storage cell. Consequently, similar as in the previous case, the masked storage areas are receiving rapidly the charge from the pixels after the first exposure and the second image can be acquired.

Another one of the most important characteristics of a CCD camera used for PIV is its sensitivity and spectral response. The sensitivity of pixels is related to the quantum efficiency (QE): the ratio between the collected photons and the number of incident photons per pixel. The main influence on this ratio is the design of the pixel, its aperture, material and thickness of the optically sensitive area. The spectral response is characterized by the quantum efficiency for different wavelengths. The micro lenses of the interline transfer imagers increase the light sensitivity by focusing the light only on the light sensitive part of the sensor.

In PIV experimental studies presented later in chapter IV., V. and VIII. a 12bit CCD camera Sensicam Qe (PCO, Germany) [40] based on a full frame interline transfer CCD, was used. It has a resolution of 1376x1040 pixels<sup>2</sup> with a pixel size of 6.45x6.45  $\mu\text{m}^2$ . More detailed technical description is listed in Table II-1. The camera is depicted in figure II-XI.

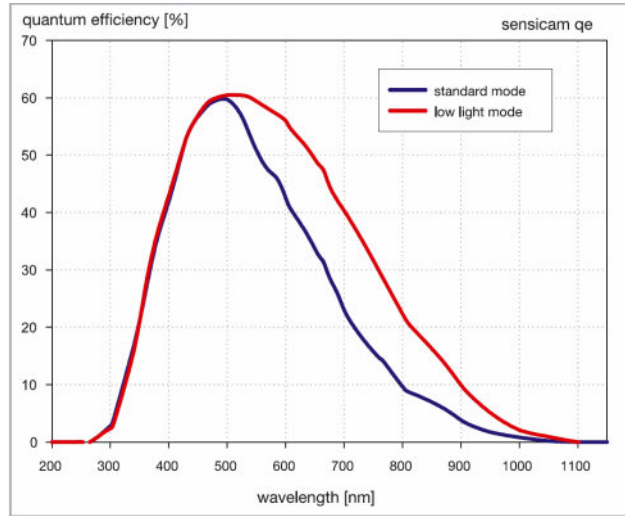


II-XI. PCO Sensicam Qe camera with mounted objective lens [40].

	<b>Unit</b>	<b>setpoint</b>	
Resolution (hor x vert)	Pixel		1376 x 1040
Sensor format / diagonal	inch / mm		2/3" / 11.14
Imaging frequency rate	Hz	full frame	10
Pixel scan rate	MHz		16
Spectral range	nm		290...1100
Exposure time	s		500 ns..3600 s
Smear	%		<0.002
Region of interest	pixel		down to 32x32
Trigger, auxiliary signal		internal / external	software / TTL level
Power consumption	W		36
Mechanical dimensions camera (w x h x l)	mm		93x78x210
Weight	kg	camera	1.6
Operating temperature range	°C		5 - 40
Operating humidity range	%	non condensing	10 - 90
Storage temperature range	°C		from -20 to 70
Optical input			c-mount with adjustable back focal length
Data interface			PCI local bus, Rev. 2.1, burst rate 132 Mbyte/s
Cooled CCD temperature	°C		-12
Quantum efficiency	%	at 500 < $\lambda$ < 600 nm	50 - 60

Table II-1. Technical data of Sencam QE from PCO [40].

According to figure II-XII the QE for the used camera reaches its maximum for a wavelength range between 500 nm and 550 nm. The measurements described later are performed at a wavelength of 532 nm – the wavelength of a standard Nd:YAG PIV laser.



II-XII. Quantum efficiency (QE) distribution for Sensicam QE CCD camera [40].

One of the advantages of this camera is the possibility to set the area of sensitive pixels. This can be used, when the dimensions of the desired ROI are smaller than the possible recording area. The possibility of inactivating pixels, which are outside the ROI, is decreasing the size by means of bytes of the recorded images. Thus the time for downloading the images from the buffer is shorter, digital storage capacity needed is lower and also the image processing is faster.

### II.3.2. *CMOS Cameras*

The main difference between a CCD imager and a Complementary Metal–Oxide–Semiconductor (CMOS) image sensor is the way the light-to-voltage conversion takes place in each pixel. This difference in readout techniques has significant implications for sensor architecture, capabilities and limitations. The key advantage of CMOS based cameras is their feasibility to capture the images with frequency in order of several kHz. The other differences between CCD and CMOS cameras are described by Litwiller [41].

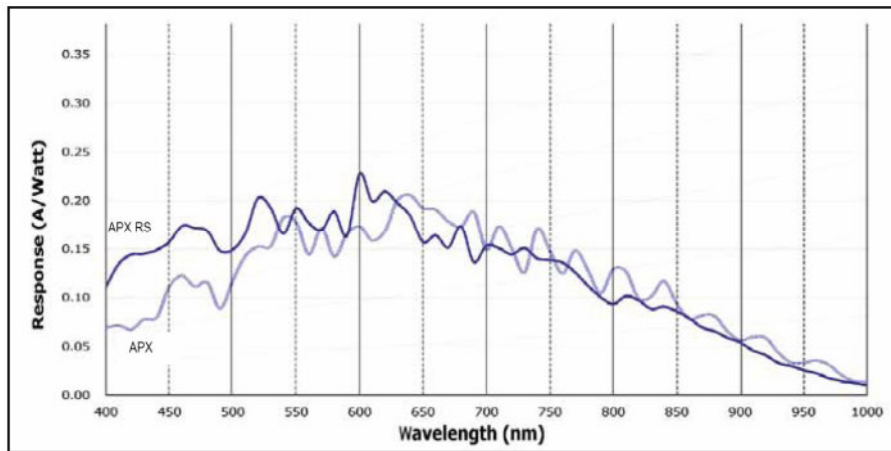
The PIV measurement cases presented in the chapters VI. and VII. were utilizing CMOS cameras: the APX RS from Photron [42] (figure II-XIII). The

maximum recording frequency is up to 250000 fps, depending on the resolution. At the full resolution of 1024x1024 pixels the maximum recording frequency is 3000 fps.



II-XIII. CMOS high speed camera Photron APX RS.

According to the spectral response of the APX RS (figure II-XIV) the maximum QE is for the wavelengths around 600 nm.



II-XIV. A plot of the spectral response of the ultima APX RS and APX camera from Photron [43].

## II.4. Image processing.

Image processing is one of the last steps in the experimental procedure. It includes algorithms which are determining the final results for the flow visualization.

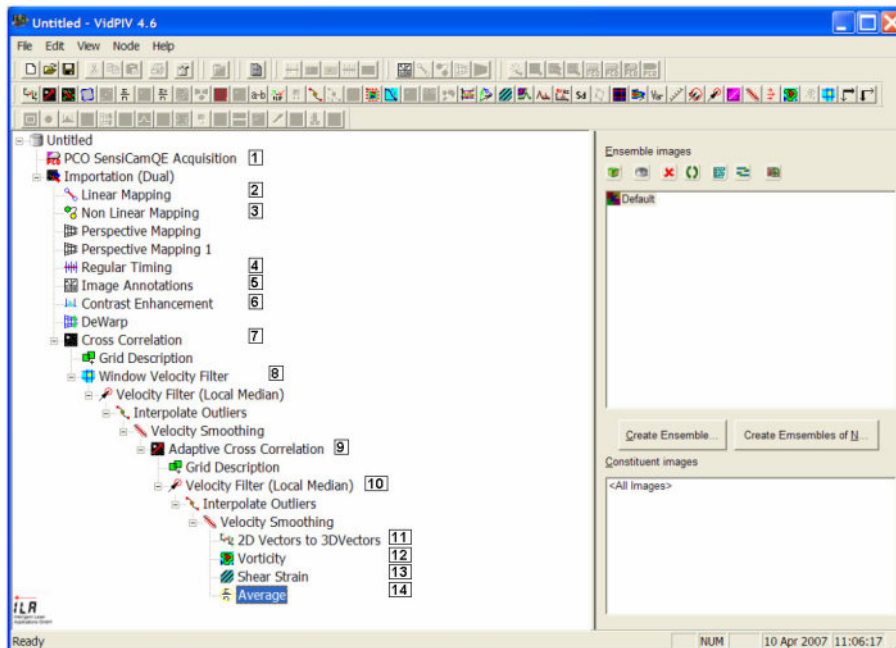
The cross correlation algorithm is one of the main mathematical methods used in PIV. It compares the pattern of the recorded particles in small areas – interrogation areas - on the acquired images and determines the relative displacement of these patterns. It is based on statistical comparison between the first and the second image. The determined mean displacement of the particles and the known time delay between the two illuminations results in a velocity vector. The interrogation area size for the cross correlation must be appropriate to the velocity gradient within the entire recorded image. The cross correlation function strongly depends on the visibility of the particle pattern (signal to noise ratio), size of the particles and its displacement. If the displacement of the particles is too long  $> 10$  pixels, small interrogation windows might not recognize the pattern of the particles between the pairs of images anymore. If the images of the particles are too small it might cause an

error known as peak locking [44]. The exhausting description of image processing in PIV is well documented in [28; 45].

The software used for data evaluation may be laboratory specific, self developed or commercially available. There are certain differences among available software, but the main characteristics are accuracy, affinity to peak-locking and the availability of advanced evaluation strategies. PIV challenges are organized every second year since 2001, to validate the software accuracy [46; 47]. The results are concerning several parameters among different study cases and PIV methods.

In the research cases described here, a commercial package of VidPIV (ILA GmbH, Juelich, Germany) software was used. According to PIV challenge results, the VidPIV software belongs to the top five among all participants.

VidPIV uses a sophisticated data management system that handles through a single interface all the aspects of data acquisition, processing and storage. To achieve this it uses highly structured project files organized in hierarchical layout. Project files appear as tree structures where all the data, measurement parameters and links between processing operations are stored (figure II-XV).



II-XV. A screen-print of the VidPIV software with tree like structure of the process nodes.

The tree-structured presentation of the interface has several key advantages. The data management is handled through a single interface window. All the hardware controls, image processing and analysing parameters, images and flow maps are accessed directly from this single interface, avoiding the confusion of multiple document windows. The evaluation strategy is fully user controllable and can be easily adapted to different experimental setups.

The right panel shows a list of the captured images and derived data respectively according to the selected node of derivative process on the left panel. There are also editing and export tools available.

The left panel called “Node View” shows a list of hardware control and process nodes applied to the captured images in the tree like structure. The top panel consists of several rows of icons, which represent derivative procedure or hardware control nodes which can be added to the tree structure.

In figure II-XV numbers indicate following procedures:

- 1- image recording or importation – There are several cameras supported in VidPIV. The settings for the camera can be adjusted. An Image importation node can be used, when the images already exists. A wide range of file types is supported [48].
- 2- Calibration mapping linear – This is used in standard PIV with a single camera system under a 90° straight view to the ROI
- 3- Calibration mapping nonlinear or perspective –These methods are used when the distance ratios change within the image: e.g. a perspective view of the camera to the ROI under a certain angle or if there are objects causing an optical distortion. The perspective calibration is used especially by stereoscopic PIV technique.
- 4- Timing – this node is responsible to set the timing between the two consecutive images during the PIV acquisition.
- 5- Image annotations – via this node the user is able to exclude certain regions (occluded regions) of the acquired images, where he does not want to calculate the velocity. This will decrease the time of image processing.
- 6- Image preprocessing – *Contrast enhancement* can sometimes improve the signal to noise ratio. *Image dewarping* is a necessary tool when calibrating and processing images by stereoscopic PIV
- 7- Cross-correlation node – this is the first process where velocity vectors are calculated. The interrogation area and distances between the vectors can be selected in a sub-node “grid description”. In the properties of the cross correlation node, Whitaker peak fit and phase correlation [49] can be selected.
- 8- Filter functions – The window velocity filter is excluding all the vectors above a maximum and below a minimum displacement threshold set in the properties of the nodes. This will avoid some random vectors falsely calculated. It should be used with care when the minimal and maximal

velocities in the entire flow are unpredictable, in order not to eliminate also valid vectors. Mean and median filter might as well be used.

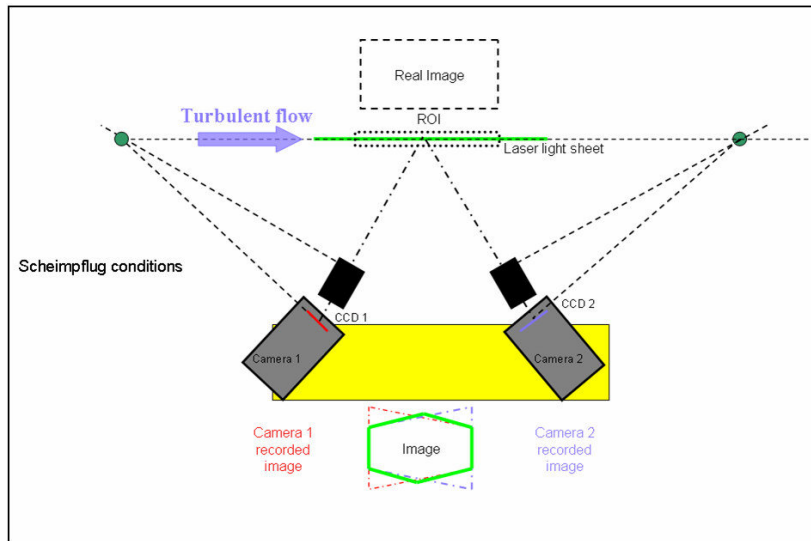
- 9- Adaptive cross-correlation - is an iterative method that allows multiple cross-correlation passes. The first pass always uses a standard cross correlation node. At each analysis pass, adaptive cross-correlation uses the vector map generated by the previous pass to refine the search for matching particle images, until convergence is achieved over the whole velocity field. Adaptive cross-correlation has many advantages over standard one-pass cross-correlation (7), in terms of dynamic range, tolerance of velocity gradients and reduced peak-locking.
- 10- Filtering, interpolating and smoothing – The median filter is used to eliminate spurious vectors which do not fit to the neighbouring vectors by using the mean value and the standard deviation of the selected e.g. 3x3 neighborhood vectors. The filtered vectors are interpolated by their neighbors. Velocity smoothing is used here to allow the iterative procedure to stabilize, so that no oscillation in the results can occur [50].
- 11- 2D to 3D vectors – Node for stereoscopic PIV, where the recombination of the vectors from different cameras take place and the results are displayed in 3D view.
- 12- Vorticity – can be calculated according to equation VII.2.
- 13- Shear strain – is calculated according to equation VII.2.
- 14- Average – statistical average values can be calculated out of the entire instantaneous velocity records.

There are several other features of VidPIV software that can be chosen, nevertheless, it will not be described here, because they weren't used for later described experimental cases in this dissertation.

#### II.4.1. *Calibration of the images.*

Calibration is needed to convert the recorded image size in pixels to real units of the ROI. This is done by placing a flat target with an array of markers (e.g. crosses, circles or dots) with known distances in the ROI. An image of the target plane is acquired. The distances of the markers in real units are used for calibrating the pixel image. For planar measurements with no optical distortions a linear calibration is suitable where only four points determine the linear transfer functions for mapping  $x$  and  $y$  in pixels to real world coordinates. Mappings are an essential part of PIV image processing, since they establish the dimensional correspondence between sensor plane and measurement plane in order to express the measured velocities in physical units. The quality of their implementation has a strong effect on the overall accuracy of the measurements, and as such cannot be overemphasized [48]. The actual size of the image coordinates in pixels is converted to real SI units of the target coordinate system.

A different approach is used when calibrating the ROI under a certain angle, especially in case of stereo PIV, when at least two cameras are arranged under the Scheimpflug condition (figure II-XVI). Once the camera is focusing on a ROI for a perspective angle, the acquired image is not focused over the complete region. This is due to the limited focal depth, when looking under an angle on a flat surface. The Scheimpflug conditions must be fulfilled in order to have the entire ROI in focus. These conditions are based on the rule, which says, that the CCD plane, the measurement plane and the plane of the camera lens must be intersecting in only one point as illustrated on figure II-XVI. The key role plays here the arrangement of the camera body and the lens. This is achieved by a special tilt mount where the camera lens and the camera body with the CCD sensor can be tilted against each other.



II-XVI. Stereoscopic PIV configuration with two cameras arranged in Scheimpflug conditions. Note the trapezoidal shape of camera 1 and 2 are mirrored. Only the overlapping region can be used as a valid ROI for the PIV measurements.

Due to the perspective camera view, the acquired images have a trapezoidal shape. Consequently the real distances in the ROI have different magnifications for opposite sides of the trapezoid. A Minimum of around 50 markers is recommended, when calibrating the ROI in order to achieve good accuracy.

Calibration in stereoscopic PIV has to be done individually for each camera, but on the same target plane. The images of the calibration target are acquired for each camera. A net of mapping datum marks are assigned to the markers on the acquired images for both cameras respectively. Consequently with help of certain geometrical reconstruction it is possible to determine three-dimensional displacement field from obtained two perspective planar calibration images. This reconstruction was presented by Willert [51]. Once the calibration is performed, image dewarping algorithm is applied to the particle images of the PIV measurement. Image dewarping is geometric back projection of the perspective deformed images to the planar view at  $z=0$ , which is based on the magnification ratio and angles among the CCD sensor, LS and lens [28].

Calibration in stereoscopic PIV has to be done individually for each camera, on the same target plane at  $z=0$ mm. The images of the calibration target are acquired for each camera and datum marks with real world coordinates are assigned to the markers on the acquired images for both cameras. A transfer function from pixel space to real world coordinates and vice versa is calculated. This transfer function uses the datum mark positions known in pixel and real world coordinates, to determine the coefficients for the quadratic or rational transfer function by a least square fit.

After evaluating the displacement for each view, a geometrical reconstruction of the two velocity fields allows to determine the three-dimensional velocity field from the known angles between the cameras [28]. This reconstruction was presented by Willert [51].

#### II.4.2. Pre-processing of the images.

The particle images should be acquired with best quality to achieve successful measurements. Sometimes it might be useful to use some pre-processing of the images which could enhance the signal to noise ratio. For example, the background subtraction can be used to remove unwanted reflections from images prior to cross-correlation analysis. In case of weak back scattered light from the particles or a different illumination for the two laser pulses, a contrast enhancement can increase the signal to noise ratio as well.

#### II.4.3. Timing of the PIV performance.

VidPIV includes a comprehensive range of control functions for synchronising the operation of all the PIV system components. These functions pass timing parameters to the ILA synchronizer, from where trigger signals are sent to the cameras and the laser. Additionally, the laser pulse separation can be entered for imported or acquired images using the timing node prior to calculating the velocity results.

#### II.4.4. Annotations of the images.

PIV images often contain areas where there is no valid information. These areas are excluded from the analysis. In addition, drawing of markers and text tools can help enhance the visual information contained in the images. A series of common resources called annotations are possible to use. They can be shared by all image processing nodes in a processing tree. One of the main advantages to use this feature is, that the annotated areas are not processed in cross-correlation and all other functions related to image processing. This might drastically decrease the time needed for the evaluation and moreover decrease the memory demand for the storage of PIV files.

### **II.5. Conclusion.**

One of the main features of PIV, is its unique ability to capture instantaneous flow fields and thus allow the detection of spatial structures in unsteady flow fields quantitatively. This is not possible with any other experimental flow measurement technique. Other benefits of PIV are: non intrusive, high accuracy and fast data evaluation. PIV has the major benefit of providing two dimensional velocity fields with up to three components in a relatively short amount of time compared to single point methods like Laser Doppler Anemometry (LDA) [52]. The measurement performance of PIV at the very beginning was rather poor compared to nowadays state of the art. The set up of the equipment and processing of the acquired images was more difficult and time consuming. By using digital cameras the technique was enhanced to Digital Particle Image Velocimetry (DPIV), but in most literature only PIV abbreviation remains and so it will be used in this dissertation. Moreover, due to the fast evolution of digital cameras and the increasing capacity and speed of computers nowadays only the digital technique is used.

An increasing interest is to use PIV data for the validation of numerical codes in Computational Fluid Dynamics (CFD). There is a common opinion that CFD is less time consuming and a cost effective solution to study fluid dynamics.

However, the improvement of CFD codes is still going on and therefore PIV results are considered as one of the most accurate for comparison. Even though the absolute measurement uncertainty of PIV is close to 1-5% it is still, as many other experimental techniques, strongly user and software dependent. The most sensitive factors, which are controllable by the operator are: perfect optical alignment, precise calibration, homogeneous seeding density and proper use of processing algorithms.

**B. In vitro study of blood  
flows by Particle Image  
Velocimetry**



### III. Introduction

Part A of this dissertation introduces briefly the anatomy and physiology of the cardiovascular system and of heart valves in particular. It also describes the Particle Image Velocimetry in a more detailed manner to clarify its principles and different experimental approaches. The main scope of part B is to introduce selected experimental set-ups and respective results.

There are two sections in part B, PIV measurements behind prosthetic *heart valves* on the one side and in *vascular access* on the other side. The 1<sup>st</sup> section starts with a case of simulated leaflet of an aortic valve in a simplified aortic root. For this a special model was designed in order to validate a 2D CFD simulation. This experiment utilizes a standard PIV approach for 2D velocity map assessment. The 2<sup>nd</sup> case was focused on 3-dimensional flow visualization behind PHVs. A stereoscopic PIV system coupled to a traverse unit enables to capture the flow at two planes parallel to the PHV's valve plane. The flow distributions behind two different types of PHV, a monoleaflet and a bileaflet, were compared. These measurements were done on the mock loop designed at the University Polytechnica delle Marche in Ancona, Italy. The same mock loop is used for the measurement of the simulated blood flow in 3<sup>rd</sup> case. In this study, to achieve detailed temporal resolution we make use of high speed PIV. Finally stereoscopic high speed PIV is used to capture the feasibility of capturing the third component with high temporal resolution.

We also demonstrate the significance of PIV for validating CFD codes to simulate the blood flow in vascular access. This section is mainly focused on the flow study of a central venous catheter used as a vascular access for hemodialysis. Finally, a result of an image based patient specific model of a vascular graft is demonstrated.

Both sections, heart valves and vascular access oriented, are finalized in a summary, in which the benefits and drawbacks of used methods are discussed and future prospects suggested.



## IV. PIV Validation of Blood-Heart Valve Leaflet Interaction Modelling\*

---

\* The content of this chapter is accepted for publication in International Journal of Artificial Organs 28.02.2007

**PIV validation of blood-heart valve leaflet interaction modelling.**

Radoslav Kaminsky, Kris Dumont, Hans-Joachim Weber, Michael Schroll, Pascal Verdonck

---

## Abstract

The aim of this study was to validate the 2D CFD results of a moving heart valve based on a fluid-structure interaction (FSI) algorithm with experimental measurements. Firstly, a pulsatile laminar flow through a monoleaflet valve model with a stiff leaflet was visualized by means of PIV. The inflow data sets were applied to a CFD simulation including blood-leaflet interaction.

The measurement section with a fixed leaflet was enclosed into a standard mock loop in series with a Harvard Apparatus Pulsatile Blood Pump (Harvard Apparatus, MA, USA), a compliance chamber and a reservoir. Standard 2D PIV measurements were made at a frequency of 60 bpm. Phase averaged velocity magnitude results of 36 phase locked measurements were evaluated at every 10° of the pump cycle. For the CFD flow simulation, a commercially available package Fluent Inc. was used in combination with in-house developed FSI code based on the Arbitrary Lagrangian-Eulerian (ALE) method. Then the CFD code was applied to the leaflet to quantify the shear stress on this leaflet.

Generally the CFD results are in agreement with the PIV evaluated data in major flow regions, thereby validating the FSI simulation of a monoleaflet valve with a flexible leaflet. The applicability of the new CFD code for quantifying the shear stress on a flexible leaflet is demonstrated.

## IV.1. Introduction

Detailed knowledge of the flow field downstream and forces acting upon the heart valve apparatus is critical for the design of new prosthetic heart valve (PHV) and for a better understanding of biomechanical actors in valvular heart disease (VHD). This is particularly true for tissue engineered aortic valves. It is still a challenge to transplant an in vitro cultured valve into the aorta, where it is subjected to high pressures and shear forces acting on the newly seeded cells. Measuring these mechanical forces in a direct way is not possible yet, but advanced numerical techniques may be used to assess the biomechanical shear forces indirectly. Ideally, numerical computations fully account for the interaction between the blood and the leaflet moving within the fluid, without predefining the blood field or the valve leaflet motion.

A number of computational fluid dynamics (CFD) studies investigating the unsteady blood flow through artificial heart valves have been presented previously [53; 54; 55; 56; 57; 58; 59; 60; 61; 62]. Several CFD simulations have been compared to experimental data sets [57; 63].

The aim of numerical modelling of flexible heart valve leaflets is to use these models in a later phase for the development of guidelines for bioreactor and tissue engineering (TE) studies of aortic heart valve leaflets. An important haemodynamic parameter influencing the endothelial cell layer is the shear stress (SS) on the leaflet. Cells seeded on TE constructs are matured and conditioned in a bioreactor. Although flow and pressure can be regulated in a bioreactor, the magnitude of SS on the cells is unknown. Maturing them in a bioreactor requires a gradual increase of SS [64; 65; 66]. Little is known about how a protocol for these TE constructs should look like and there is a need for standardization [64; 66].

This FSI-CFD algorithm should allow assessment of SS exerted on the valve inside the bioreactor and, hence, could help to develop a protocol with gradually

increasing SS. In this way, the endothelial cells would be able to adapt to the flow and gradually orientate in the direction of the flow [67].

The aim of this study was to validate a new 2D FSI algorithm for the flow simulation through a stiff heart valve leaflet, fixed in a tube with a sinus bulb acting as a half of an ascending human aorta. CFD simulations showing excellent agreements with experimental results will help us to use the algorithm in predicting the motion of flexible leaflets, decreasing manufacturing and experimental costs of a new prosthetic heart valve design.

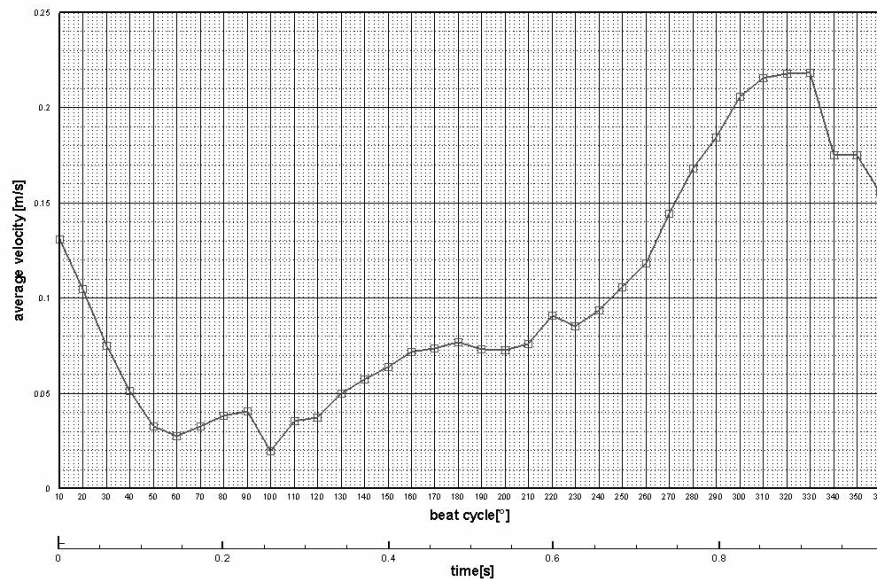
## IV.2. Methods

### IV.2.1. *Experimental model*

The flow visualization through a stiff leaflet was investigated using an in vitro mock loop. A unique measurement section was manufactured to model a half of a left ventricular outflow tract and a human aorta and one leaflet of an aortic heart valve. The test section is 100 mm wide and the height of the channel is 10 mm. In the middle of the channel a leaflet is clamped. A sinus is present behind the leaflet, modelled as a geometry having semicircular contour, across the channel. Inflow and outflow diffusers were used to guide the fluid to and out of the measurement section. The diffuser channel starts with an inlet diameter of 10 mm, which is equal to the inner diameter of the tube connecting the diffuser to the pump, and ends with a rectangular outlet of 10x100 mm<sup>2</sup>, which equals the area of the inlet of the measurement section. The height of the outlet remains 10 mm and the width increases from 10 mm to 100 mm on both sides (4° angle). The base of the channel is therefore trapezoidal. The measurement section is 120 mm long and the outlet of the measurement section is connected to the diffuser of which the width decreases from 100 mm to 10 mm. At the end of the diffuser a 10 mm inner diameter tube is connected. This design was utilized in order to achieve 2D flow at the middle of the measurement section in main flow direction. In order to check the two-

dimensionality of the flow, we measured the cross-plane velocity in the middle of the measurement section upstream the leaflet position. The cross plane velocity was measured at  $310^\circ$  and didn't exceed 0.01 m/s, which is less than 3% of the absolute velocity in main flow direction. The measurement section was made of a transparent material (Plexiglas) to allow optical access necessary for the PIV measurement performance.

A Harvard Apparatus Pulsatile Blood Pump (Harvard Apparatus, MA, USA) was generating the flow with a systole/diastole ratio of 40/60. The average velocity over the cycle was measured at the inlet of the measurement. The pump was generating the flow of the working fluid (distilled water), stored in reservoir, through the mock model into the compliance chamber. From the compliance chamber the fluid flows directly to the reservoir. The average velocity at measured degrees of the cycle is shown in figure IV-I. The Reynolds number ( $Re \sim 1782$ ) was calculated according to the average velocity through the entire beat cycle.



IV-I. Plot representing the average flow velocity at the inlet of the measurement section as a function of time (lower axis: in ms, upper axis: in degrees of the cycle).

For the stiff leaflet (i.e., negligible flexibility) we used a PVC strip (Young's modulus  $2900\text{-}3400 \cdot 10^6 \text{ N/m}^2$ , thickness 0.5 mm, height 11.6 mm and width 98 mm). The width of the leaflet was 2 mm less than the channel width in order to avoid friction forces at the side walls. The flow leakage at the sides was assumed negligible compared to the entire flow through the channel. The leaflet was attached with three water proof sticky tape strips clamped in the upper part of the channel with a simple clamp mechanism. The 10 mm wide and 30 mm long thin tape was glued to the leaflet in the middle and its both end sides. One end of the strips was attached to the leaflet, while the other was attached to the upper part of the housing inside the channel so that the strips were acting like hinges. The upper part of the housing consists of 2 components. Between both components the strips were clamped to fix the leaflet in a specific position, in particular, below the sinus bulb. The leaflet was attached close to the clamp, so that it only allowed the rotational degree of freedom.

A standard 2D PIV (ILA GmbH, Juelich, Germany) system was used to perform the experiments. A pulsed Nd:YAG laser reaching the maximum energy of 25 mJ was used as a light source. A CCD Sensicam QE camera was used to record images stored in bitmap format.

Red fluorescent particles, micro-spheres of about 50  $\mu\text{m}$  diameter, were added to the working fluid. Applying a red band-pass filter in front of the CCD sensor only red light ( $\lambda_{\text{band}} = 590 \pm 20 \text{ nm}$ ) was visible for the camera. Fluorescent particles emitted the red light ( $\lambda_{\text{emission}} = 580 \sim 620 \text{ nm}$ ) once they cross the green laser LS ( $\lambda_{\text{excitation}} = 532 \text{ nm}$ ). Measurements were done under control of the synchronizer which gets the trigger signal from the piston of the pump. Angle trigger phase locked mode was chosen for acquiring the PIV images every  $10^\circ$  of the cycle. In total 36 measurements have been performed. Note that the trigger was not set at either of the absolute end positions of the piston, but somewhere in the middle between them. This was chosen only because of technical reasons. For evaluating the PIV images we used the commercial

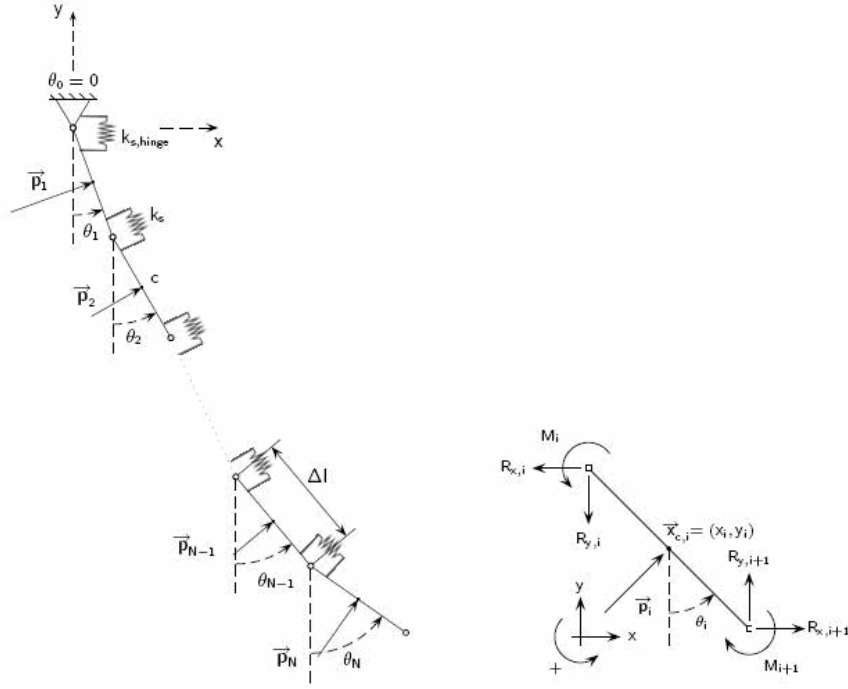
VidPIV software package with iterative window deformation [50; 68; 69], B-spline grey value interpolation [70] and phase correlation [49].

#### IV.2.2. *Numerical model*

There are different strategies to tackle numerically the FSI problem. One possibility is to develop new software and solution methods for each of these coupled applications. This is referred to as the monolithical approach or the direct method [71]. On the other hand, one can make use of existing methods and software packages which have been developed for either fluid or structure related applications and consider iterative methods [72], also known as partitioned methods [71] for FSI. As such, separate solvers are used for the fluid and the structure problem [73]. The coupling between both, with an exchange of updated meshes and boundary conditions, is done in an iterative way. The latter approach has been applied in this study. Using Fluent (Fluent Inc., New Hampshire, US) as a fluid solver, a structure solver has to be coupled to the fluid solver in an iterative way.

The ALE remeshing technique of Fluent requires at least one cell in the gap between the valve leaflet and the wall. As a result, the valve will never close completely. However, the gap can be made as small as required by local refinement of the mesh.

A new 2D structural model of a flexible heart valve leaflet (figure IV-II) illustrates how the 2D flexible heart valve leaflet with a length  $l$  is modelled [74; 75]. The leaflet consists of  $N$  equidistant segments with length  $\Delta l = l/N$  connected to each other with frictionless pivots and with torsional springs, characterized by the spring constant  $k_s = EI/\Delta l$ , where  $E$  is the Young's modulus of the material and  $I$  is the moment of inertia of an individual segment of the leaflet.



IV-II. Schematic of the implemented material model for a flexible leaflet: segments are connected with frictionless pivots and angular stiffness (left panel). Forces acting on a single segment of the flexible leaflet (right panel).

The material model is based on earlier studies by David et al. [76]. If the pressure distribution  $p$  on the leaflet is given by the fluid solver Fluent, the unknown variables are the positions  $\underline{X}$  of the segment centres, the angles  $\theta$  defining the position of the leaflet, and the reaction forces  $R_x$  and  $R_y$  in the  $x$ - and the  $y$ -direction, respectively. A detailed description of the iterative procedure can be found in [66].

The equation describing the material model is written as

$$G(\underline{p}, \underline{X}, \theta, \underline{R}_x, \underline{R}_y) = 0$$

Two equations (2D model) express that the length of the leaflet segments has a constant value  $l$ . Furthermore, Newton's 2<sup>nd</sup> Law of Motion states that the acceleration of a particle is equal to the vector sum of forces acting upon that particle, divided by its mass. This conservation of momentum results in an

equilibrium equation of the forces in the x-direction, and in the y-direction and the rotational equilibrium equation.

$$\left\{ \begin{array}{l} G_{i,1} = 0, \\ G_{i,2} = 0, \\ G_{i,3} = 0, \\ G_{i,4} = 0, \\ G_{i,5} = 0 \end{array} \right. = \left\{ \begin{array}{l} x_i = x_{i-1} + \frac{\Delta l}{2} \cdot \sin(\theta_{i-1}) + \frac{\Delta l}{2} \cdot \sin(\theta_i), \\ y_i = y_{i-1} - \frac{\Delta l}{2} \cdot \cos(\theta_{i-1}) - \frac{\Delta l}{2} \cdot \cos(\theta_i), \\ m \cdot \ddot{x}_i = -R_{x,i} + R_{x,i+1} + p_i \cdot \cos(\theta_i), \\ m \cdot \ddot{y}_i = -R_{y,i} + R_{y,i+1} + p_i \cdot \sin(\theta_i), \\ I \cdot \ddot{\theta}_i = M_i - M_{i+1} + \frac{\Delta l}{2} \cdot (R_{x,i} + R_{x,i+1}) \cdot \cos(\theta_i) \\ \quad + \frac{\Delta l}{2} \cdot (R_{y,i} + R_{y,i+1}) \cdot \sin(\theta_i) \end{array} \right.$$

The equations are linearized with Newton linearization and solved iteratively upon convergence.

A grid convergence study was performed. Two different grid densities, i.e.,  $\pm 2100$  cells with the leaflet divided in  $N=10$  segments and  $\pm 4650$  cells with the leaflet divided in  $N=15$  segments, were studied with a time step ( $\Delta t$ ) of 0.001 s. Two subsequent cycles were calculated in order to have results independent of the initial zero flow in the entire fluid domain. The stiffness  $EI$  of the aortic valve leaflet used in this model equals  $2.7 \cdot 10^{-5} \text{ Nm}^2$ . Young's modulus  $E$  for normal aortic valve leaflets found in literature is between  $1 \cdot 10^6 \text{ N/m}^2$  and  $2 \cdot 10^6 \text{ N/m}^2$ . We chose  $E$  equal to  $1.5 \cdot 10^6 \text{ N/m}^2$ . The thickness of the leaflet varies between 0.2 mm and 1.4 mm, yet, like most researchers, we used a value of about 0.6 mm for the leaflet thickness of the aortic valve. With the moment of inertia  $I = bh^3/12$  (with  $h$  = thickness of the leaflet and  $b = 100 \text{ mm}$  the reference width of the 2D model) the above mentioned value of  $2.7 \cdot 10^{-5} \text{ Nm}^2$  was obtained. The hinge stiffness,  $k_{s,hinge}$ , is somewhat lower than the leaflet stiffness. For both meshes the same value for  $k_{s,hinge} = 0.0075 \text{ Nm/rad}$  was used.

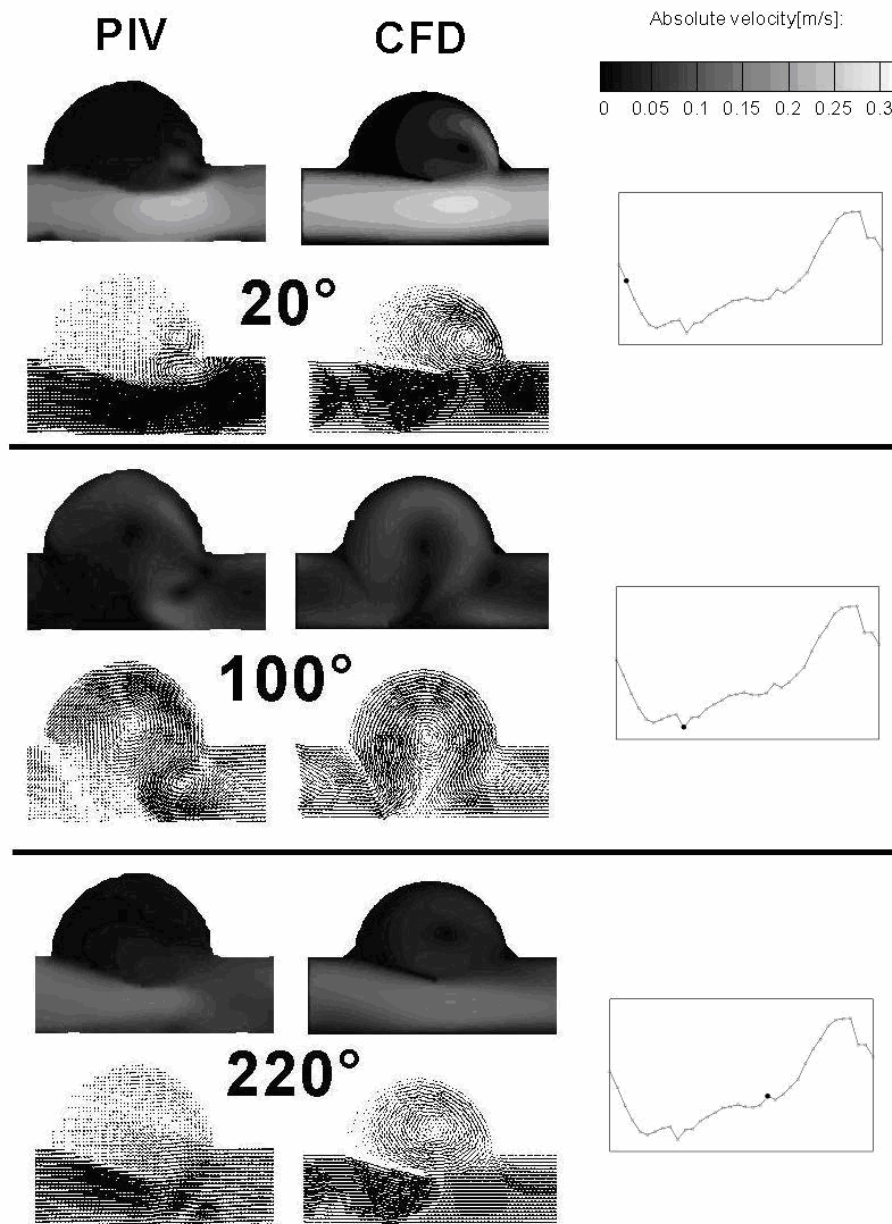
A similar iteration procedure was used for modelling the valve with a stiff leaflet. The equation of motion for the leaflet with angle  $\theta$  is  $M = I \cdot \ddot{\theta}$ , where  $M$  represents the moment on the leaflet (result from the pressures),  $I$  the

moment of inertia and  $\ddot{\theta}$  the acceleration of the leaflet. The stabilization of the iterative procedure is here treated with the derivative  $\frac{\partial M}{\partial \ddot{\theta}}$  [74; 75]. For the detailed validation study we opted to model the stiff aortic valve leaflet, in order to reduce the complexity of the validation study and also to increase the accuracy of the validation process, because the numerical flexible leaflet consists of  $N$  equidistant stiff leaflets.

### IV.3. Results

The measured flow velocity field downstream the stiff monoleaflet model with PIV was compared with the Computational Fluid Dynamics (CFD) simulation for 36 different time-points of the cardiac cycle.

The general agreement between the CFD results and the PIV experimental measurements can be seen from the contour and velocity plots through the stiff leaflet in selected time steps (figure IV-III, left panel: PIV, right panel: CFD). However, there are several mismatches over minor local regions. Especially at the point of  $20^\circ$  PIV reveals two small vortices above the distal tip of the leaflet rotating counter wise to each other. In contrary, CFD determines in the same region a single vortex larger than the both small vortices of PIV results. Moreover, at the phase of  $220^\circ$  there is a large vortex filling the entire sin us area with magnitude up to 0.1 m/s presented by CFD, but experimental results at this region show rather velocities close to 0 m/s.



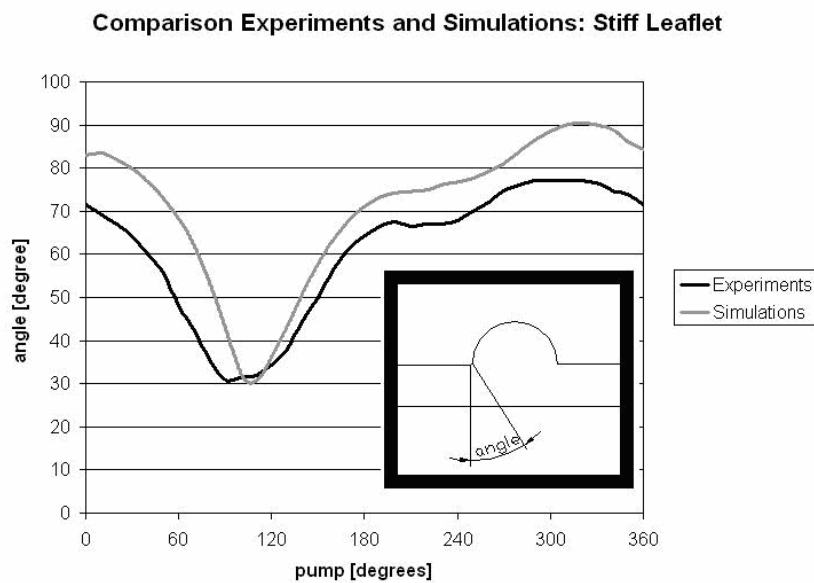
IV-III. Velocity fields (presented in absolute velocity magnitude in grey scale and vector plots) through the stiff monoleaflet at three positions of the piston pump: 220° (valve opening), 20° (valve closing) and 100° (valve closed): (i) left panel: PIV measurements and (ii) right panel: CFD simulations. On the right side the black circles in the average velocity plots indicate the respective visualized steps (more detailed in figure IV-1).

Experimental data have been evaluated through a number of iterative adaptive cross-correlation algorithms. The achieved resolution was 16x16 pixels. This

means that the distance among the calculated vectors was 16 pixels (equal to 0.5 mm) both in  $x$  and  $y$  direction over a region of interest of  $40 \times 20$  mm<sup>2</sup>, thus covering the entire demonstrated flow field. The peak systolic phase angle position resulting from the simulation was higher, with a value of  $90.8^\circ$  compared to  $77.8^\circ$  in the experimental model. A similar difference was found in an earlier study [75].

During the acceleration period in the early systolic phase a residual vortex is remaining in the sinus from the previous diastolic period of the cycle. This vortex vanishes during the systole. The fluid below the leaflet accelerates up to 0.32 m/s. During the deceleration period of the cycle two vortices develop. One is located downstream the sinus and, later on, a larger vortex develops in the sinus itself, which helps closing the valve.

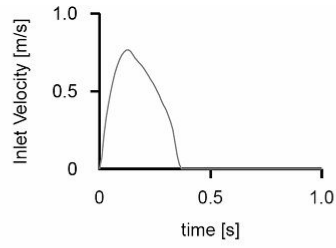
The stiff leaflet reached at the peak systolic phase an angle position of  $77.8^\circ$ , starting from an initial position of  $32^\circ$  (figure IV-IV).



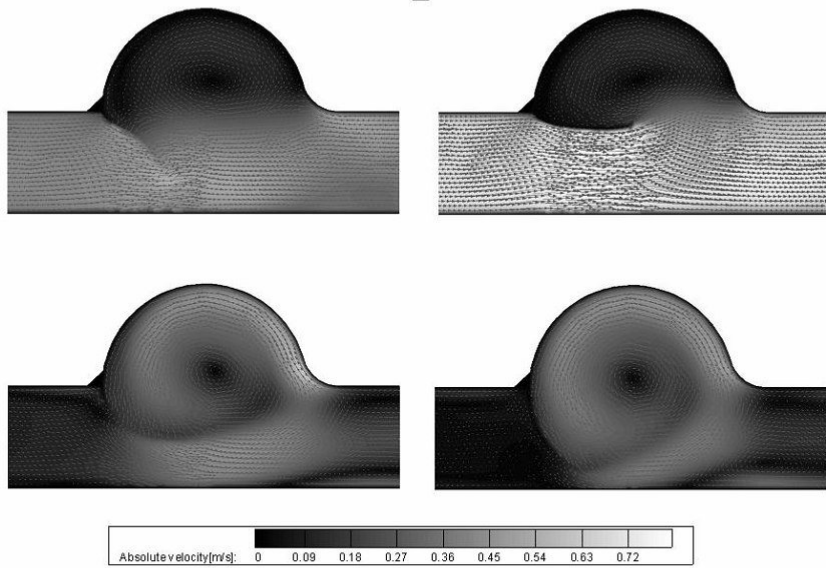
IV-IV. Comparison of the stiff leaflet excursion between the experiments and the CFD simulations.

We also investigated the flow around the flexible leaflet with the FSI code. In general the flow behaviour is similar, however, particular differences in some

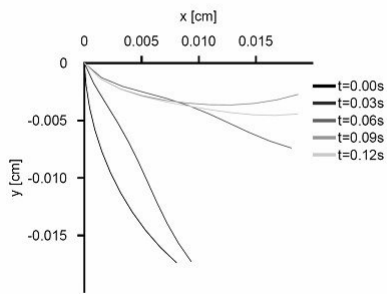
minor regions were observed (figure IV-V). These results were assessed in time at equal beat frequency 1 Hz. Figure IV-Va shows the inlet velocity for the CFD-FSI calculation. Figure IV-Vb demonstrates the velocity magnitude in four different time steps, two during early acceleration and two during valve closing phase. The flexible leaflet changes its shape during opening and closing, as can be seen on figure IV-Vc and IV-Vd. The SS values on the leaflet throughout the cycle are plotted in figure IV-Ve.



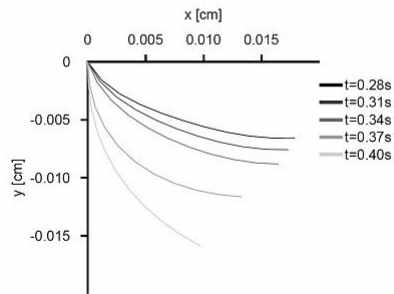
(a) Inlet velocity for the CFD-FSI calculation with flexible leaflet.



(b) Vector plots (top at 0.035s and 0.09s, bottom at 0.34s and 0.4s of the flow cycle)



(c) Leaflet shape during opening phase.



(d) Leaflet shape during closing phase.

IV-V. CFD results with a flexible leaflet: (a) inlet velocity; (b) vector plots and (c) leaflet shape for different time instances.

## IV.4. Discussion

In this case PIV was directly used to compare the results to a CFD model in order to estimate the uncertainties in the investigated ROI. From CFD perspective, the challenging task was not only to calculate the flow through the valve, but also to model the dynamic interaction of the aortic valve leaflet with the surrounding blood and to calculate the local deformations and stresses in the structure. Vierendeels et. al. [66] presented in detail a model based on the available commercial fluid solver Fluent (Fluent Inc., New Hampshire, US), which makes use of an ALE approach. The software allows for the simulation of flows where the shape of the structure is changing with time. Although this software is capable of solving a wide range of engineering and biomedical problems, it does not account for the interaction between the fluid and the structure. For that reason, we developed an iterative method based on the available Fluent software.

When comparing the numerical results with experimental evaluations we didn't find significant differences in the major area of evaluated region of interest (ROI). However, in some regions some mismatches were found. Two small vortices were captured above the distal end of the leaflet by PIV compared to a large vortex also with higher velocity magnitude was determined by CFD at the phase of  $20^\circ$ . At the phase of  $220^\circ$  CFD simulations shows the vortex almost completely filling the sinus region whereas the PIV results shows velocity magnitude close to 0 m/s in the same region. The complex flow behind a valve, a moving solid object in a fluid, is a challenge for simulations. Therefore advanced FSI codes are developed and ask for validations. Even though there is an agreement in major ROI between PIV and CFD it is clear that simulations are still not in the level of truly and completely predict the correct results. It has to be mentioned that even though the experimental and CFD results are compared in a 2D space, the experimental model is a 3D geometry. In order to confirm that the third velocity component in the measured ROI was not significant, we first evaluated the 3rd velocity component at  $310^\circ$  of the cycle which is the time step near peak systole. We

found that the values in the middle of the channel in the main direction are relatively low compared to the main flow velocity.

For easier handling we chose distilled water as a working Newtonian fluid. We assumed that a blood analogue was not required for validating the CFD results. When doing further investigations about blood like fluid interacting with a valve, one needs to change the parameters of the working fluid in the numerical experiments.

Due to the limitations of the chosen CFD code the leaflet didn't allow to touch the bottom of the channel during the simulations. However, as the gap is very small compared to the channel, we didn't observe major differences in the flow field at that region. Although a good qualitative and quantitative agreement is shown in figure IV-III, the opening angle of the stiff leaflet in the experimental set up is lower than the one calculated by CFD (figure IV-IV). A few reasons for this difference between the CFD simulations and experimental results can be found. The width of the channel in the measurement section is slightly larger than the width of the leaflet, thereby introducing leakage flow at the sides. In those regions there are significantly lower forces acting on the leaflet. Furthermore, since the tested valve is fixed to the top of the inflow channel using three strips of adhesive tape, a small amount of fluid can leak over the top of the valve among these strips. When the valve is closed and the fluid starts to move forward, the fluid passing underneath the valve will force the valve to open. Since some of the fluid will leak over the valve, the valve will possibly not open as far as without the leakage.

In a later stage, this model could be used to assess the wall shear stress on the valve leaflets during a complete cardiac cycle, fully accounting for the delicate interaction between blood flow and stiffness properties of the valve leaflets. Therefore, the possibility of modelling flexible leaflets was already implemented in this CFD-FSI model.

When comparing simulations of the flexible heart valve model to the stiff one, we found numerically similar flow behaviour in general. The few differences

between both techniques (e.g., the exact position of the vortex core, the leaflet's excursion, the region of distribution of maximal and minimal velocities) appeared mostly during the acceleration and deceleration period.

Currently available heart valves are nonviable valves and all have disadvantages in one way or another. Most of their shortcomings could be solved by tissue engineering, where it is theoretically possible to grow a valve with patient specific biological material, consisting of viable tissue. Until now, most research efforts failed in the final stage of implantation of the valve in aortic position, which seems to indicate that the preconditioning of the valve should be optimized to train the valve in withstanding the high forces in *in vivo* conditions. There is overwhelming evidence that the function and integrity of cells exposed to flow is highly dependent on the nature of the flow regime, which determines the magnitude and direction of the shear forces exerted on the cells. Therefore, in order to set up a protocol for cultivating, maturing and growing a tissue engineered cardiovascular device, it is important to assess and to control the shear forces exerted on the fragile freshly seeded cells. These shear stresses can be easily calculated in simple flow geometries, as in cell culture devices, but not in the more complex *in vivo* environment or inside a bioreactor. This is where numerical techniques (CFD) can help.

To tackle this type of problem, the stiff leaflet model needed to be extended to a flexible leaflet model, as one of the goals was to predict the shear stresses on a tissue engineered valve construct, cultivated in a bioreactor. Adding the flexibility of the valve leaflet resulted in a complex iteration procedure. However, available software code, demonstrates that FSI of the flexible heart valve is feasible in this setting.

## **IV.5. Conclusions**

Our 2D experimental PIV validation of a CFD simulation on the model of a heart valve with a stiff leaflet confirms the simulated CFD results. However,

there are several mismatches between the results of both methods. A new FSI algorithm is available to model the interaction between blood and a flexible leaflet taken from a tissue engineered heart valve.



# V. Stereoscopic PIV Measurements of Flows Behind Artificial Heart Valve†

---

† The content of this chapter is accepted for a publication in a forthcoming book of Springer TAP series in November 2007: "Particle Image Velocimetry - New Developments and Recent Improvements".

Chapter: **PIV measurements of flows in artificial heart valves.**

Radoslav Kaminsky, Stephan Kallweit, Massimiliano Rossi, Umberto Morbiducci, Lorenzo Scalise, Pascal Verdonck, Enrico Tomasini

---

## Abstract

In the past five decades many different models of prosthetic heart valves (PHV) have been designed and optimized in order to enhance their haemodynamic properties. These properties are not only material dependent but the major influence results from the mechanical assembly of the particular PHV. For the experimental assessment of the flow through such PHVs PIV is generally an accepted method due to its non invasive optical approach and accuracy. In this chapter we are presenting a stereoscopic PIV method in order to explain its suitability for the quantification of such flows. The choice of the experimental procedure for testing the PHVs is strongly dependent on the optical access of the designed in vitro testing loops simulating the human heart and vascular system. The hardware requirements and its configuration for stereoscopic PIV is much more complex than standard 2D PIV, therefore the conditions and design of the testing loop have to be realized to allow the desired flow measurement. The flow in heart valves as an unsteady periodically generated flow, is obtained by averaged phase locked measurements. The properties, advantages and drawbacks of stereoscopic PIV technique to visualize the flow behind a PHV will be discussed.

## V.1. Introduction

The fluid dynamic through PHVs has been shown to play a critical role in the clinical outcome for patients undergoing cardiac valve implantation. This is particularly true when mechanical valves are implanted.

Common to all mechanical PHVs is the incidence of:

- thromboembolic complications, primarily due to platelet activation [8, 24] which appears to be intimately related to the non-physiological flow characteristics of the blood through PHVs. As pointed out by Bluestein et al. [77; 78] the vortices shed by valve's leaflets in fully open position induces flow that increases the risk of free emboli formation by activating and aggregating platelets.
- mechanical trauma to red cells, which could cause the rupture of the membrane of the erythrocytes, leading to hemolysis (a more exhaustive discussion can be found in [79; 80]).

For the reasons mentioned above, fluid dynamical characterization must be performed in the risk analysis for those devices.

However, the fluid dynamics of PHVs is particularly complex, as testified by a great number of studies performed by using Laser Doppler Anemometry (LDA) technique (see[81], for example), with high spatial gradients and shear stresses, especially as far as mechanical heart valves are concerned. The fine-scale characteristics of such flows (e.g. turbulence production, vortex shedding, flow separation, stasis) need experimental techniques with high spatial and temporal resolution for the estimation of the cause of haemodynamics related complications such as hemolysis, platelet activation, and thrombus formation. This is only possible by knowing the precise velocity field and stress distribution obtained by using these techniques.

LDA is a widely applied tool for fluid dynamic investigations that has been used for more than three decades. It constitutes the golden standard for velocity measurements, in virtue of its peculiar features, (i.e. non-invasivity, high spatial and temporal resolution, excellent accuracy). The application of LDA in the evaluation of PHVs function has been well documented [81]. Estimation of SS related blood damage in heart valve prostheses was assessed in an *in vitro* comparison of 25 aortic valves [82; 83]. However, the complete analysis of the relevant flow area using the LDA technique is very time consuming, taking longer to investigate both the whole fluid domain, and the whole cardiac working cycle of a PHV. In virtue of its multipoint measurement characteristics, it furnishes full-field measurement of instantaneous velocity vectors, in the fluid domain of interest. Nowadays, PIV has gained sufficient temporal and spatial resolution to estimate velocity fields - depending on the degree of instability in the flow [84]- providing a powerful tool for studying the safety and efficiency of implantable medical devices.

In this chapter we present the application of stereoscopic PIV to study mechanical PHV fluid dynamics. So far this PIV technique has been rarely used for investigating the challenging issue of PHVs fluid dynamics.

## **V.2. Materials and Methods**

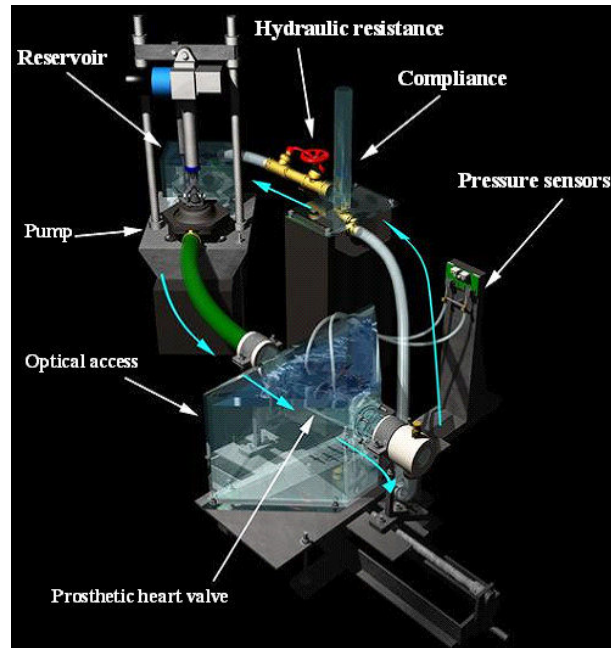
The stereoscopic PIV technique was applied to study the fluid dynamics of the Carbomedics (Sorin Group Canada, Inc.) valve, a typical bileaflet mechanical PHV with two flat half-disk leaflets and with a 27 mm tissue annulus diameter (figure V-I).



V-I. Carbomedics bileaflet valve inserted in a tube, ready to be embedded to the mock loop.

#### V.2.1. *The testing loop*

Measurements were carried out in pulsatile flow working conditions, in the testing loop depicted in figure V-II. A challenge in performing flow measurements downstream of prosthetic heart valves by means of laser based techniques is to develop a dedicated optical access for carrying out LDA, 2D and 3C (three component) PIV measurement. The reason for the design of the testing model in figure V-II was to realize an experimental set up particularly designed for studies to be performed with the experimental techniques mentioned above [85; 86; 87; 88].



V-II. Scheme of the mock loop simulating left heart and vascular system.

The testing loop mainly consists of a test chamber, a reservoir and a pulsatile flow volumetric pump. The test bench has an optically clear valve housing segment to allow unobstructed optical measurements of the aortic flow with different measurement techniques. The test chamber consists of a prismatic box with a trapezoidal section (73.5x65x50 mm) in which the 30 mm internal diameter cylindrical glass pipe hosting the prosthesis is mounted. The oblique sides of the box are 45 degrees inclined with respect to the centre axis of the glass pipe, giving an optical access normal to the view direction of the cameras. This configuration assures the minimum error in the out-of-plane velocity component, when measured with stereoscopic PIV [89].

A Delrin-made coupling system presses the cylindrical glass pipe, maintaining a central alignment of the former. The cylindrical pipe, submerged in a prismatic chamber, is fixed by mechanical compression.

The rest of the testing loop is a three-element Windkessel model which simulates the arterial systemic load. A discharge tank mimics the left atrial chamber. The left ventricular function can be simulated at various cardiac

outputs and heart rates by means of a volumetric pulse generator, i.e., an electro-mechanical pushing plate device with a variable stroke volume in the range of 40 to 300 ml. The volume of the modelled left ventricle is approximately 80 ml. This allows the prescription of pulsatile flow through the valve prosthesis. The design of the hydraulic circuit allows prescribing plug flow velocity pattern entering the valve.

Distilled water was used as working fluid ( $\eta=1.14 \times 10^{-3}$  Ns/m<sup>2</sup> at 15 °C temperature). What we did, was to apply the Buckingham theorem, which is the basis of dimensional analysis. The theorem states that if we have an equation (Navier-Stokes) involving a number K of physical variables, and these variables are expressible in terms of L independent fundamental physical quantities, then the original expression is equivalent to an equation involving a set of P dimensionless variables (  $P = K - L$  ) constructed from the original variables.

As previously stated [85], measurement results can be translated into the physiological domain, accounting for the principle of dynamical similarity theory [90]. The unsteady blood flow can be described by two dimensionless numbers, the Reynolds number (Re):

$$\text{Re} = \frac{4Q}{\pi \nu D} \quad [\text{V-1}]$$

and the Womersley number (Wo):

$$\text{Wo} = \frac{D}{2} \sqrt{\frac{\omega}{\nu}} \quad [\text{V-2}]$$

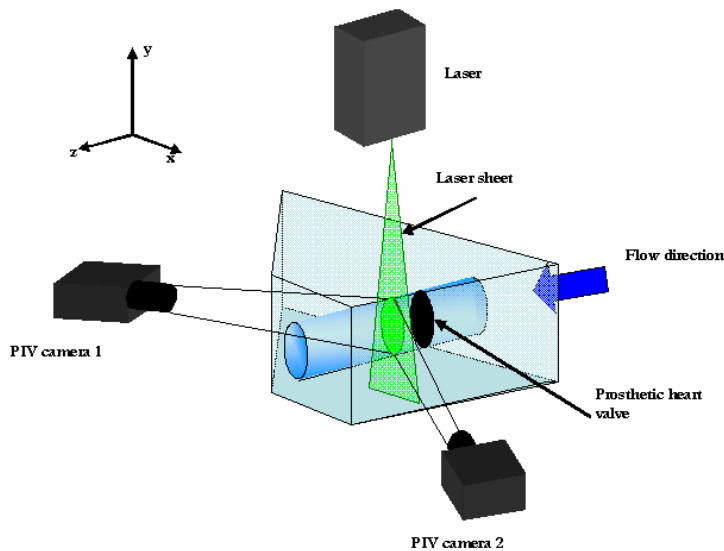
where  $Q$  is the flow rate,  $D$  (30 mm) is the diameter of the cylindrical glass tube,  $\nu$  is the kinematic viscosity and  $\omega$  is the pulsation of the command waveform. In the present study, distilled water was used as working fluid ( $\eta=1.14 \times 10^{-3}$  Ns/m<sup>2</sup> dynamic viscosity, at 15 °C temperature). A test bench using distilled water as a working fluid is equivalent to the same test conducted using blood if both Reynolds and Womersley numbers (for distilled

water and blood tests) are equal. To obtain the blood-analogue ( $4 \times 10^{-3} \text{ Nsm}^{-2}$  dynamic viscosity) working conditions (70 beats/min, 4 l/min cardiac output, 100 mmHg mean aortic pressure), corresponding to a mean Reynolds number of 710 and a Womersley number of 20. The use of a Newtonian working fluid is an approximation widely adopted by researchers involved in *in vitro* studies on PHVs fluid dynamics.

### V.2.2. 3C PIV: measurement technique

In the 3C stereoscopic-PIV configuration, two CCD Sensicam QE [40] cameras were used together with a Nd:YAG New Wave [30] double-cavity laser ( $\lambda=532\text{nm}$ ).

The two cameras, capable of recording 1376x1040 pixel double-images, were inclined by 45 degrees with respect to the principal direction of the flow (z axis in figure V-III). Thus, the angle formed by the axes of the two cameras was 90 degrees, assuring an optimal measurement of the cross-plane velocity.



V-III. Schematical view on the stereoscopic PIV set-up.

The cameras are arranged in the Scheimpflug configuration by means of rotatable lens and camera body seats. The schematic of the test bench for

stereoscopic PIV measurements, similar to the one adopted in [85], is displayed in figure V-III.

The laser beam was guided from the source to the cylindrical optics via an articulated light arm. The optics converted the laser beam to a LS, a plane with a thickness of about 2 mm, defining the ROI along the x-y plane. Red fluorescent ( $\lambda_{\text{excitation}} = 527 \text{ nm}$ ,  $\lambda_{\text{emission}} = 580 \sim 620 \text{ nm}$ ) micro spheres ( $d_p = 50 \mu\text{m}$ ,  $\rho = 1.05 \text{ g cm}^3$ ) have been added to the flow as seeding particles. A red bandpass ( $\lambda_{\text{band}} = 590 \pm 20 \text{ nm}$ ) filter placed in front of the CCD sensor eliminated the excitation wavelength and thus the wall reflections of the glass tube and the prosthetic heart valve.

Commercial VidPIV 46XP (ILA GmbH, Juelich) software is used for data evaluation. The calculation of instantaneous velocity vector maps in the region downstream the PHV was done by means of cross-correlation of successive images: a first correlation, including Whitaker peak fit and phase correlation [49] was performed on 32x32 pixel (16 pixel shift) interrogation boxes; then a local median filter was applied, and filtered vectors were interpolated; on smoothed data an adaptive correlation function was applied on 16x16 pixel (8 pixel shift) interrogation boxes. This processing step includes subpixel shifting, and window deformation [50; 68] using grey value reconstruction by B-spline interpolation [70]. The complete algorithm is performed iteratively.

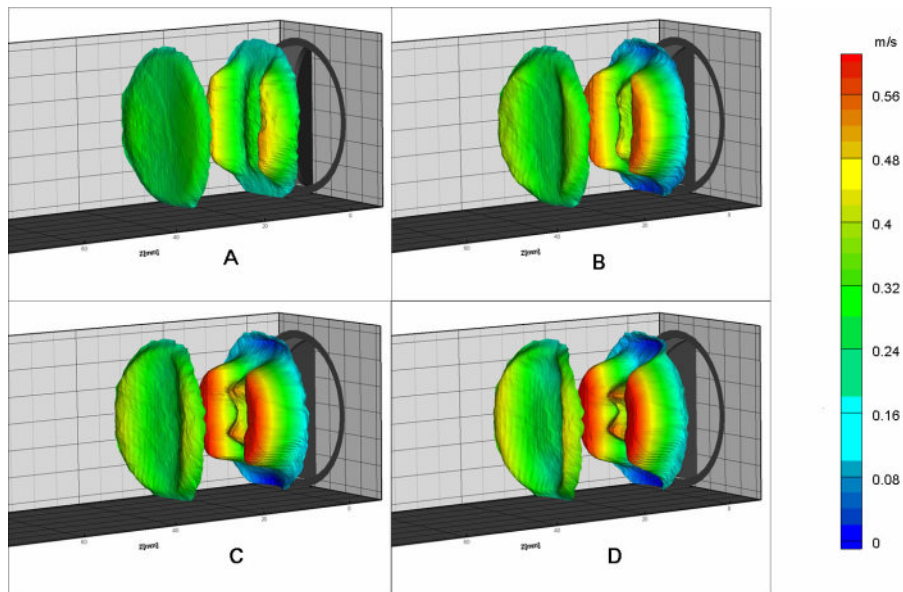
A synchronizer (ILA GmbH, Juelich) was controlling the acquisition sequence to guarantee a synchronised recording of images to the generated laser pulses. Recording was done in phase locked mode.

The mismatch between the RI of the fluid and the surrounding material can be corrected using a non-linear mapping function (chapter II.4.1.). In order to minimize optical distortions affecting the data, the camera calibration was done by applying a cubic polynomial mapping grid: datum markers are placed in the middle of crosses which are distorted by the RI mismatch, so the distance (in pixels) among them vary in the distorted image; by knowing the real distance, distortion in the image can be numerically corrected.

The images were analyzed with a multi-grid technique, starting with a 64x64 pixel correlation window in the first step and a 32x32 pixel correlation window in the second step. Commercial ILA software is used for both data evaluation and stereoscopic PIV calibration. The planes at  $z = 1$  and 3 cm were considered in the 3D measurements where  $z = 0$  corresponds to  $z$ -coordinate of the valvular plane. For statistical purposes 100 pairs of images have been taken to calculate phase averaged results.

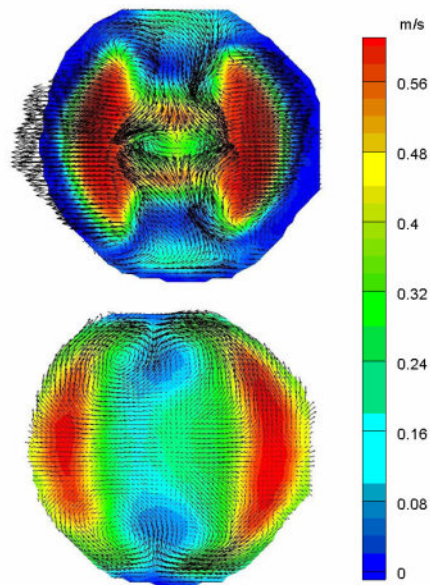
### **V.3. Results**

We measured the flow in a cross-sectional plane parallel to the valvular plane, located 1 cm and 3 cm downstream of the valve, so that the out-of-plane structures in the velocity field correspond to the main direction of the flow. This choice was suggested by the fact that it has been widely assessed that the mixing process, as the one associated to prosthetic valves fluid dynamics, is intimately connected with the transient of turbulence [91]. The streamwise vortices generated in a jet flow, in addition to ring type vortices, have been found to mix fluid streams even more efficiently. Good statistics were assured by choosing an adequate sample size. The stereoscopic PIV technique allowed to evaluate and compare the three-dimensionality of the flow field downstream of two prosthetic valve models, and to catch the specific features of both the jets and the vortical structures in the chosen planes of investigation. The classic three jet configuration outgoing from the valve around the systolic peak is displayed in figure V-IV, where it is clearly evident that the jets outcoming from the side orifices of the bileaflet PHV reach velocities higher than the central orifice jet.



V-IV. Results of velocity magnitude behind a bileaflet valve. The values are color scaled. The flow is visualized in four different time instance during the acceleration systolic period at 1 and 3cm downstream the valve (A – 330, B – 390, C – 450, D – 510 ms after the start of the PIV acquisition).

Figure V-V displays the contour map of the out of plane velocity (i.e., the velocity component in the main flow direction) superimposed to the in plane vector field at peak systole. Measured planes are parallel to the valve plane and located 1 and 3 cm downstream of the latter.



V-V. Stereoscopic PIV: contour map of the out of plane (axial) velocity component magnitude superimposed to the in plane vector field behind the bileaflet valve at peak systole (510 ms the initiation of PIV measurement). The measurement plane is 1 (top) and 3 (bottom) cm downstream of the valve plane. 2D view presents color scaled absolute velocity and vectors indicate in plane velocity as a result of two velocity components.

The three jets coming from the valve orifices are clearly evident, together with areas of backflow. It is possible to appreciate also the topology of the in plane flow field in the bulk region, strictly related to the vortices wakes released by the leaflets. Due to the vector velocity field show in figure V-V, it is obvious, that the secondary flow plays a significant role.

#### V.4. Discussion

Flow through PHV is a typical example of complex fluid domains dominated by massive unsteady flow separation, and flow patterns rapidly changing in time. The experimental investigation of such complex spatio-temporally developing flows has always been a challenging task.

The flow field downstream of a prosthetic heart valve is fully three-dimensional, so stereoscopic PIV seems to be eligible for the evaluation of the flow pattern behind implantable devices [89]. Recently stereoscopic PIV technique has been proposed as a measurement solution for a deep and complete analysis of PHVs' fluid dynamics in commercial circulatory loop models [92; 93].

The accuracy in the determination of the out-of-plane displacement (i.e., velocity) is related to the angle between the two cameras [94]. The larger this angle (up to  $90^\circ$ ), the more accurate is the determination of the out-of-plane displacement. With a restricted optical access, a smaller angle must be used, and a cost of accuracy in determining the third velocity component must be paid.

As recently assessed by Grigioni and colleagues [95], several problems arise in performing 3D PIV on heart valve substitutes, due to the fact that with a commercial test facility it may not be feasible to configure the set up in order to attain an angle of  $90^\circ$  between probes' axes, without image distortions. This limitation was overcome in the present study, due to the great modularity and manoeuvrability of the used circulatory loop model, which can be considered particularly useful from a validation point of view.

However, in the application of PIV technique as a reliable measurement solution for the complete fluid dynamic analysis of prosthetic heart valves related, several methodological and technological problems remain to be solved. The evaluation of second order moments of turbulence, i.e., variance, Reynolds stresses, etc., is strongly dependent on the accuracy [96] and could require the acquisition of a great number of images per measurement plane, which was not done in our study. Due to the limited time and storage capacity, we acquired only 100 image pairs in a phase locked measurement.

## **V.5. Conclusion**

Stereoscopic-PIV provides the best opportunity to examine the non-stationary flow behaviour during a heart valve cycle. Flow stagnation may be considered for thrombosis prediction, and the three-dimensionality of the vortices shed by the leaflets may be investigated more in detail, being involved in platelet activation and emboli formation.



# VI. High Speed PIV Technique for High Temporal Resolution Measurement of Mechanical Prosthetic Aortic Valve Fluid Dynamics‡

---

‡ The contents of this chapter were published in

International Journal of Artificial Organs, 2007; 30: 153-62

**Time-resolved PIV technique for high temporal resolution measurement of mechanical prosthetic aortic valve fluid dynamics.**

Radoslav Kaminsky, Umberto Morbiducci, Massimiliano Rossi, Lorenzo Scalise, Pascal Verdonck, Mauro Grigioni

---

## Abstract

Prosthetic heart valves (PHV) have been used to replace diseased native valves for more than five decades. Among these, mechanical PHVs are the most frequently implanted. Unfortunately, these devices still do not achieve ideal behaviour and lead to many complications, many of which are related to fluid mechanics. The fluid dynamics of mechanical PHVs are particularly complex and the fine-scale characteristics of such flows call for very accurate experimental techniques. Adequate temporal resolution can be reached by applying time-resolved PIV, a high-resolution dynamic technique which is able to capture detailed chronological changes in the velocity field. The aim of this experimental study is to investigate the evolution of the flow field in a detailed time domain of a commercial bileaflet PHV in a mock-loop mimicking unsteady conditions, by means of time-resolved, high speed, 2D PIV. The investigated flow field corresponded to the region immediately downstream of the valve plane. Spatial resolution as in a standard PIV analysis of prosthetic valve fluid dynamics was used. The combination of a Nd:YLF high-repetition-rate double-cavity laser with a high frame rate CMOS camera allowed for a detailed temporal resolved acquisition of the flow downstream of the PHV. Features that were observed include the non-homogeneity and unsteadiness of the phenomenon and the presence of large-scale vortices within the field, especially in the wake of the valve leaflets. Furthermore, we observed that analysis allowed the different behaviours exhibited by the bileaflet valve at closure to be captured in different acquired cardiac cycles. By accurately capturing haemodynamically relevant time scales of motion, time-resolved PIV characterization can realistically be expected to help designers in improving PHV performance and in furnishing comprehensive validation with experimental data on fluid dynamics numeric modelling.

## VI.1. Introduction

The evaluation of the fluid dynamical behaviour of PHV is considered of fundamental importance to determine the correct functionality of these devices, especially in regard to quantities related to potential blood damage [81; 97; 98; 99; 100; 101; 102]. Currently, implanted valve substitutes must exhibit intrinsic characteristic features such as a low transvalvular pressure gradient and durability (especially mechanical heart valves), assuring an acceptable clinical outcome for patients who have received a cardiac valve implantation. However, complications (e.g. leakage, mechanical failure) may still arise after implantation of PHVs, in some cases with asymptomatic failure of the implanted device [103]. This aspect implies that clinical conditions must be periodically and strictly monitored, and that fluid dynamical characterization must be performed as a critical point in the risk analysis.

The fluid dynamics of PHVs is particularly complex, highly unsteady, non-homogeneous and turbulent, especially as far as mechanical heart valves are concerned. The fine-scale characteristics of such flows (e.g. turbulence production, vortex shedding, flow separation, stasis) call for very accurate experimental techniques in terms of both spatial and temporal resolution. To this end, LDA, the golden standard for non-invasive fluid dynamic investigations, has been widely applied in the evaluation of PHVs [81; 82; 83; 99; 104; 105; 106; 107], in virtue of its high spatial and temporal resolution and excellent accuracy. However, the complete analysis of the relevant flow area using the LDA technique is very time consuming, taking longer to investigate both the whole fluid domain and the whole cardiac cycle.

PIV systems using standard cameras and lasers are limited in terms of repetition frequency and thus are also limited in terms of their sequential image capturing capability. Until new devices became available recently, it was not possible to perform the analysis of changes in the continuous flow field in the high temporal resolution associated with PHVs using standard PIV

systems. Recent technical developments in laser optics have allowed the introduction of high-speed PIV. This new approach, taking advantage of high temporal resolution digital video cameras, enables time-resolved investigation of turbulent flows associated with prosthetic valves.

The purpose of this experimental study is to investigate in detail the fluid dynamics downstream of a bileaflet mechanical prosthetic aortic valve using a high-speed, high time-resolution PIV system to map the entire flow field. The time-resolved analysis allowed the evolution of the fluid structures in the flow field downstream of the valve to be studied in time during single simulated cardiac cycles. In particular, the high temporal resolution of the technique allowed the behavior of the bileaflet valve model at closure to be investigated.

## **VI.2. Materials and methods**

The valve model considered in this experimental study is the Carbomedics (Sorin Group Canada, Inc.) valve (27 mm tissue annulus diameter, maximum opening angle 78°), a typical bileaflet mechanical prosthetic valve with two flat half-disk leaflets (figure V-I).

Measurements were carried out in pulsatile flow working conditions, in the mock loop described in previous chapter.

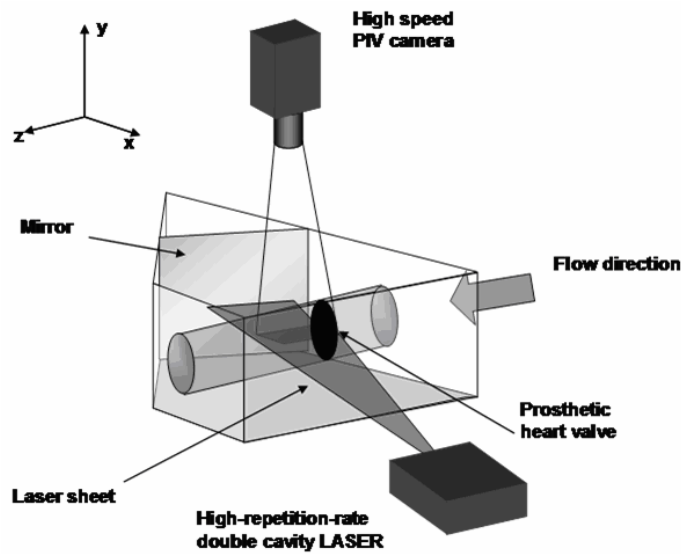
## **VI.3. Measurement technique**

High speed PIV technique essentially uses the same measurement principle as standard PIV technique [108], but with an acquisition rate that is three orders higher.

The combination of a Nd:YLF high-repetition-rate double-cavity laser with a high frame rate CMOS camera allowed a detailed, temporally resolved acquisition of the unsteady flow downstream of the valve model under investigation. The Nd:YLF laser generated the green light ( $\lambda = 527$  nm) which

was used as a light source for the PIV measurement. In this case we used a double-cavity Nd:YLF laser Pegasus (New Wave Research Inc., Fremont, CA, USA) with a maximum repetition-rate of 10 kHz and a maximum pulse energy of 10 mJ. The laser beam was guided from the source to the cylindrical optics via an articulated light arm. The optics converted the laser beam to a LS, illuminating the ROI along the plane x-z (figure VI-I). The light plane was adjusted to a width of approximately 1 mm (the LS thickness should be adjusted to be approximately four times greater than the out-of-plane displacement of the seeding particles [28]). A mirror was used to avoid shadowed areas in the ROI caused by the furthest leaflet from the laser source, when opened. For the image acquisition a Photron APX RS CMOS camera (Photron Europe Limited, Marlow Bucks, UK) was employed.

The ROI was placed in the central plane of the glass tube downstream from the valve plane. The LS was orthogonally oriented both to the datum of the valve, and to the CMOS camera: a schematic of their position, together with the chosen plane of investigation, is shown in figure VI-I. Red fluorescent ( $\lambda_{\text{excitation}} = 527 \text{ nm}$ ,  $\lambda_{\text{emission}} = 580 - 620 \text{ nm}$ ) microspheres ( $d_p = 50 \text{ }\mu\text{m}$ ,  $\rho = 1.05 \text{ g/cm}^3$ ) are added to the flow as a seeding of particles. A red bandpass ( $\lambda_{\text{band}} = 590 \pm 20 \text{ nm}$ ) filter was placed in front of the CMOS sensor to eliminate the excitation wavelength and, thus, the wall reflections of the glass tube and the heart valve. A micro-Nikkor 60 mm f2.8D lens was connected through the camera via an F-mount.



VI-I. Schematic of the test chamber, in terms of optical access. A test chamber was devised with the cylindrical glass tube lodged inside.

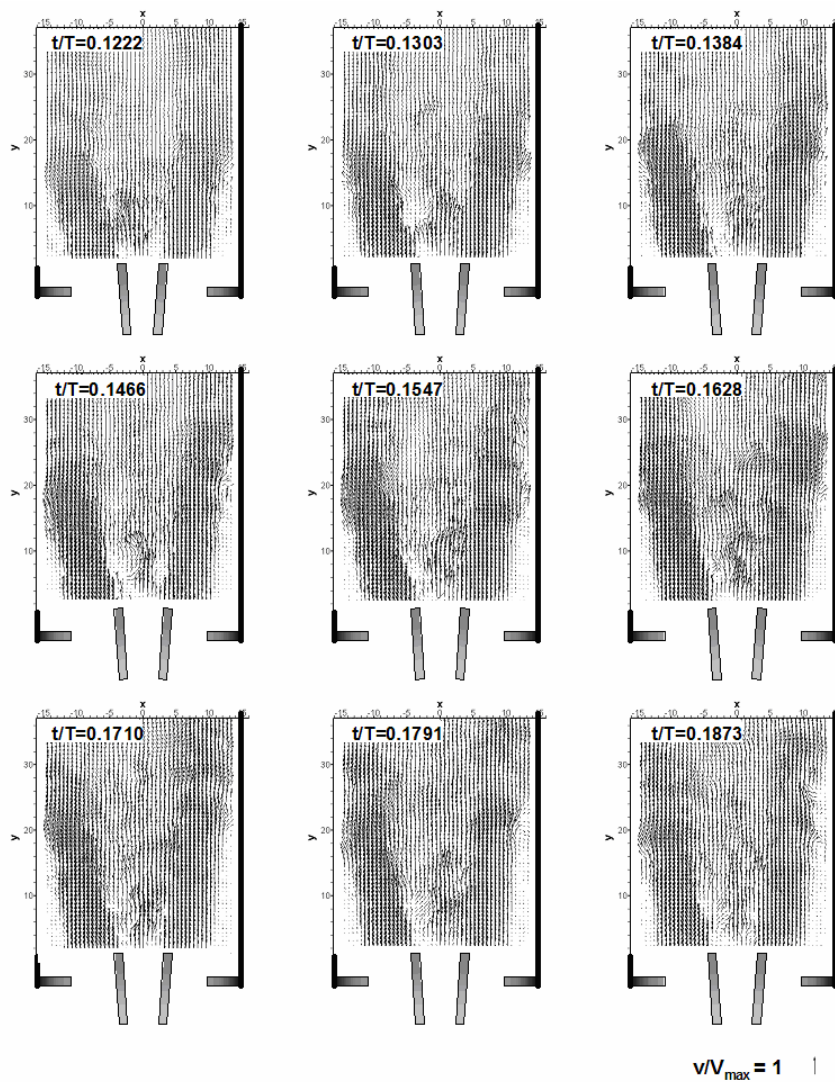
Commercial VidPIV 46XP software (ILA GmbH, Juelich, Germany) was used for data evaluation. The calculation of the instantaneous velocity vector field in the region downstream of the PHV was done by means of a cross-correlation of successive images, as follows: a first correlation, including Whitaker peak fit and phase correlation [49] was performed on 32x32 pixel (16 pixel shift) interrogation boxes; then, a local median filter was applied and filtered vectors were interpolated; based on smoothed data, an adaptive correlation function was applied on 16x16 pixel (8 pixel shift) interrogation boxes. This processing step includes subpixel shifting, and window iterative deformation [50; 68; 69] using grey value reconstruction by B-spline interpolation [70]. The complete algorithm is iteratively performed. A synchronizer (ILA GmbH, Juelich, Germany) controlled the acquisition sequence to guarantee a synchronized recording of images to the generated laser pulses.

Recording 3000 frames per second, we achieved a measurement time resolution of 333.33  $\mu$ s. (i.e.,  $f_{ia} = 3000$  Hz is the image acquisition frequency). We kept the measurement frequency  $f_m = 1500$  Hz, performing the following correlation sequence: 1st image with 2nd image; 3rd image with 4th image, etc..

The camera recorded images of the ROI, which was set to 1024x512 pixels. As for the spatial resolution, the size of the evaluated area was 35.5x27.8 mm<sup>2</sup>. In this area a grid of 60x45 vectors was calculated; on this basis, a spacing of 0.6 mm corresponds to 9 pixel units. This means that we used a spatial resolution similar to a standard PIV analysis of prosthetic valve fluid dynamics. Since there is a mismatch in the RI of the fluid and the surrounding material, in order to minimize optical distortion which affects the data, camera calibration was performed by applying a known offset nonlinear mapping grid (VidPIV software). Datum markers are placed in the middle of crosses which are distorted by RI mismatch, so the distance (in pixels) among them vary in the distorted image; by knowing the real distance, the error in the image can be numerically corrected.

#### **VI.4. Results**

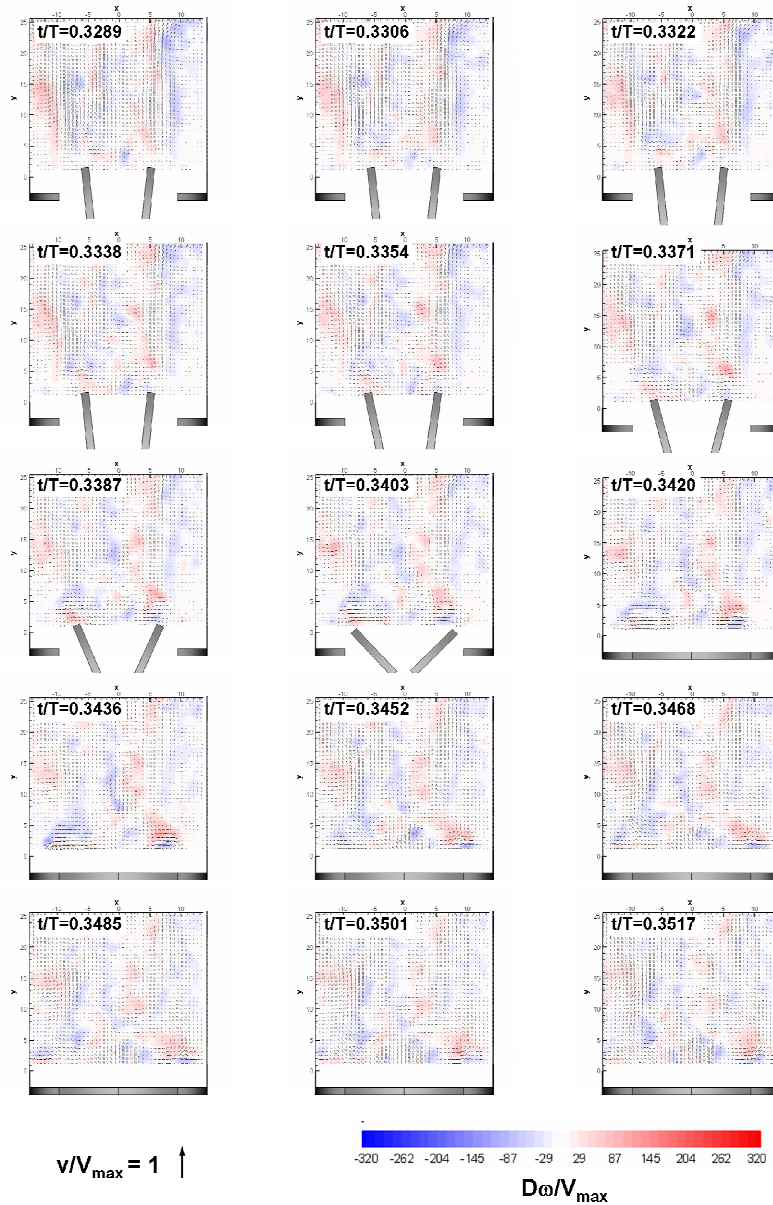
The results presented have been made nondimensional with respect to the reference velocity value (the maximum velocity magnitude at peak systole,  $V_{ref}$ ), to the diameter of the cylindrical aortic conduit ( $D$ ), and to the time duration of the cardiac cycle ( $T$ ). The analysis of the vortical, spatio-temporally developing flow downstream of the bileaflet valve model is given in figure VI-II at nine different time instants during the cycle. In particular, the PIV measured velocity vector field evolution around peak systole (late acceleration  $t/T < 0.15$ , peak systole, early deceleration  $t/T > 0.16$ ) is shown: the three-jet configuration outgoing from the valve around the systolic peak is clear from figure VI-II, together with the evolution of the vortices shed by the leaflets. Jets outgoing from the side orifices of the prosthetic device are slightly skewed towards the walls. This phenomenon is due to the boundary action exerted by the trailing vortices shed by the leaflets in the central region. These vortices cause a reduction of the effective area useful to the fluid axial flowing: as a consequence, the side jets reach the highest velocity values at a distance of about half a valve diameter from the valve plane, around the systolic peak.



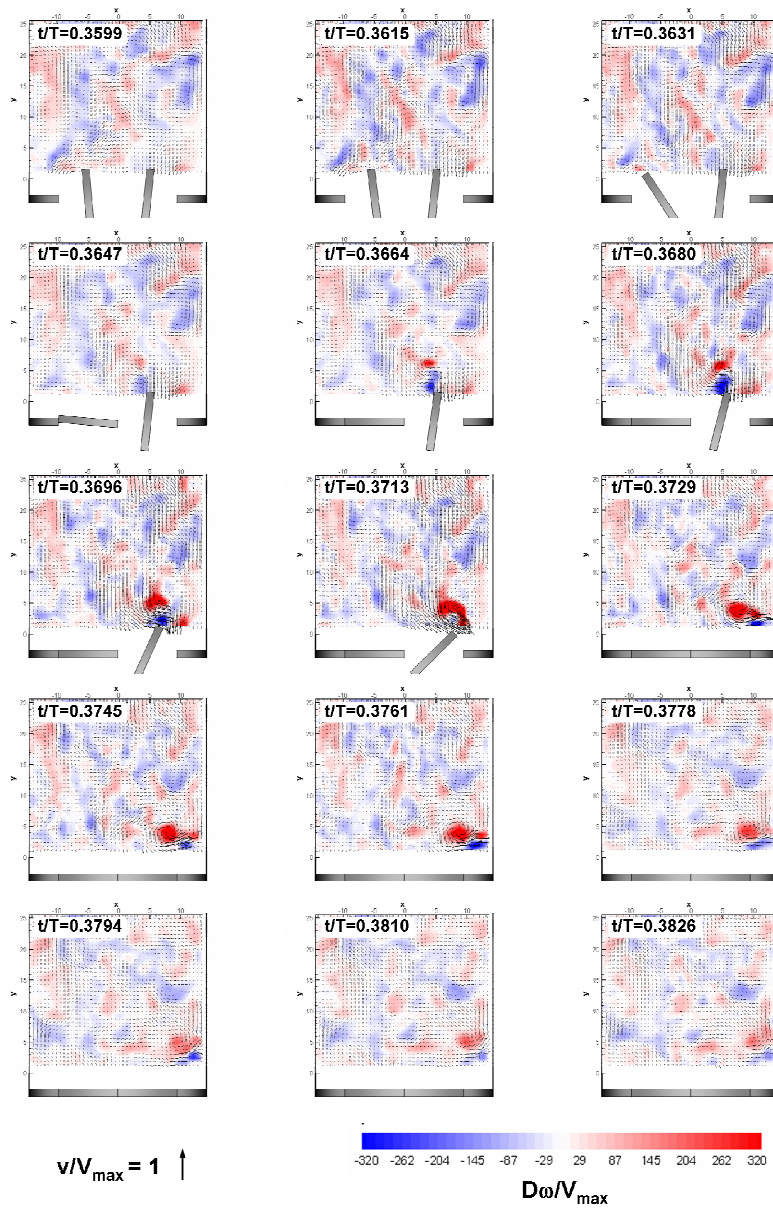
VI-II. Sequential presentation of the velocity vector field evolution downstream of the bileaflet valve model around peak systole  $t/T=0.1547$  (late acceleration, peak systole, early deceleration).

These side jets leave re-circulating regions on the walls of the test chamber duct, and their position and extension changes in time. The extension of the three jets clearly involves the whole investigated fluid domain. The loss of organization in the flow field increases in the deceleration phase due to inertial effects, in a manner that is typical for intermittent turbulent flows in the transitional range. This loss of organization greatly involves the jet from the central orifice (figure VI-II,  $t/T>0.16$ ).





VI-III. Sequential presentation of the flow field evolution downstream of the bileaflet valve model at closure (cycle A). An almost simultaneous closure for the two leaflets can be observed, as demonstrated by the symmetry of the velocity vector field and the vorticity magnitude with respect to the longitudinal axis of the valve conduit. Here is the non dimensional vorticity expressed where  $D$  is the tube diameter,  $\omega$  the vorticity and  $v_{\max}$  the maximal velocity.



VI-IV. Sequential presentation of the flow field evolution downstream of the bileaflet valve model at closure (cycle B). Contrarily to cycle A (figure VI-III), a strong asymmetry in the flow field testifies to asynchronous behavior of the two leaflets, with the closure of the left leaflet coming before the closure of the right one. A counter-rotating vortex is clearly present over the right leaflet. Consecutive flow fields that could be measured by using standard PIV may be measured with a limited time delay of about 5 ms.

As an example of the capability of the time-resolved PIV technique to capture fluidic structures rapidly evolving in time, the flow field of the bileaflet valve at

closure was investigated in detail. An analysis of cycles was studied: the closing behaviour of the investigated valve in two distinct, consecutive simulated cardiac cycles (keeping the same experimental conditions) is shown in figure VI-III (cycle A) and figure VI-IV (cycle B). In particular, the flow field evolution during cycle A (figure VI-III) puts in evidence a simultaneous closure for the two leaflets, as demonstrated by the symmetry of both the velocity vector field and the vorticity magnitude with respect to the longitudinal axis of the valve conduit. The vorticity is here expressed non dimensional. Conversely, a strong asymmetry in the flow field testifies to the asynchronous closure of the two leaflets in cycle B (figure VI-IV): the supra-avalvular vortical blood flow affects the specific closing behaviour of the individual leaflets, with the closure of the left leaflet taking place before the closure of the right one. It can be noticed, in figure VI-IV, that both the earlier closure of the left leaflet and the presence of backflow create a counter-rotating vortex that pushes the right leaflet to close. This vortex still persists in the supra-avalvular region after the closure of the right leaflet.

We undersampled the frames acquired with time resolved PIV, in order to test if time-resolved PIV is capable of capturing flow structures otherwise undetectable with the traditional multipoint technique. We verified the velocity results of two image pairs taken with a time delay of 5 ms [91], which can be considered as representative measurement of conventional PIV analysis of PHVs fluid dynamics. Figure VI-IV shows that with standard PIV acquisition frequency, the evolution of the supra-avalvular vertical flow interacting with the right leaflet at closure could not be captured. Notably, improved temporal resolution provides greater detail of the flow compared to standard PIV performed with the same spatial resolution and with a dual-head diode-pumped Nd:YLF laser source like the time-resolved PIV.

## **VI.5. Discussion**

Flow through PHVs is very complex and dominated by massive unsteady flow separation and structures rapidly changing in time. The experimental

investigation of such complex spatio-temporally developing flows has always been a challenging task, suffering both from hardware and software limitations. The level of complexity is increased significantly in the case of involved interaction with deformable walls and moving structures [109].

In vitro experiments to study the local fluid dynamics inside of artificial devices involve the use of advanced techniques such as LDA and PIV [102; 107; 110]. However, the PIV technique, which has the undoubted advantage of performing full-field measurements, has suffered from poor temporal resolution until now, revealing limitations in the analysis of transient phenomena. This drawback leads to a partial lack in detailed information, with the consequence that certain ‘micro’ aspects of a mechanical valve performance (especially flow disturbance) cannot be evaluated.

It is worth noting that in the past, PIV investigations of PHVs were carried out with time delay higher than 1 ms (5 ms [87]: in 6 phases during systole [94]; and from 10 to 1 ms [111; 112]). With such recording frequency it is not possible to identify fast events in flow dynamics of a PHV such as e.g. rebound of the valve leaflet [109]. The time-resolved PIV technique allows limitations in the analysis of rapid transient flow phenomena to be overcome.

In the present study, the use of a dual-head diode-pumped Nd:YLF source configuration made it possible to generate pulses with better energy distribution and to accommodate a broader range of experimental conditions than is possible with double-pulsed single cavity arrangements at such measurement frequencies.

Very recently, time-resolved PIV was applied to the study of the in vitro flow field associated with PHVs in the left ventricle [113], and it was demonstrated that it produces very detailed information comparable to the LDA results [114]. In the present investigation we have staged in vitro experiments to understand and to characterize the processes involved in the operation of mechanical PHVs in the aortic position. The use of the time-resolved PIV technique, by assuring high sampling rate, made it possible to fully resolve the temporal evolution of

the flow downstream of a bileaflet mechanical valve model and to map its complicated dynamics, characterized by very high non-homogeneity and unsteadiness. Moreover, time-resolved PIV enabled us to catch the different flow field evolution in the supra-avalvular region of the bileaflet model at closure, in two simulated cardiac cycles. This phenomenon, caused by different closing behavior of the individual leaflets, would not always have been evident at conventional sampling rates (figure VI-III). Moreover, when the proposed method is applied to the study of PHV fluid dynamics, it allows the analysis of complete, single working cycles. This cannot be performed with conventional PIV, where an “equivalent cycle” is measured by acquiring single phases of different cardiac cycles and performing a phase averaging of them. Time resolved PIV characterization, therefore, which accurately captures haemodynamically relevant time scales of motion, can realistically be expected to be helpful in the design progress of reliable mechanical heart valves by improving their performance.

Starting from time-resolved PIV measurements, the analysis of fluidic patterns in comparative terms could be made to discriminate between normal and malfunctioning prosthetic devices, by evaluating the level of spread in valve behaviour cycle by cycle [115]. The application of time-resolved PIV to measure the flow through PHVs could also be helpful in the validation of numeric codes for studies in CFD [116]. In fact, numerical methods are suggested as useful to overcome the intrinsic difficulties in performing quantitative observations of local flow disturbances by any of the currently available laboratory techniques (both LDA and PIV may suffer from poor resolution in particular districts of the in vitro set-up where the illumination is not optimal or the experimental procedures do not have access to the ROI). This method, expected to be a low-cost tool, could lead to a better understanding of the dynamics of flowing blood. CFD, for its capability of solving with a high degree of resolution both the flow field downstream of a heart valve, and the complex blood patterns within the valve itself, is a complement and an alternative to LDA and PIV techniques. However, to gain further confidence of valve designers and medical practitioners, CFD must also undergo comprehensive validation with

experimental data. Such validation requires the use of high-resolution flow measuring tools and techniques [117; 118; 119]. As stated by Grigioni et. al. [120], the study of PHV fluid dynamics, because of its unsteadiness, interaction between fluid and valve, geometrical complexity and high velocity gradients, requires particular care to be taken in the numerical model development. To confirm that numeric modelling of the flow through PHVs is still a challenge, the validity of some widely used computationally expedient assumptions were discussed by Ge et. al. [121]. They concluded that time- and space-resolved simulations are needed for a numerical approach to provide accurate prediction of flow in prosthetic devices.

A possible limitation of the investigation may be that the measured flow fields do not represent an average (i.e. sample size is one). We decided to describe the fluid dynamics of two single working cycles of the valve with high temporal resolution, searching for cycle-by-cycle differences in the valve's behaviour: phase averaging of velocity data has the effect of hiding the different behaviours of the valve shown by our results. Thus, our results are unable to provide details on the turbulence associated with PHVs. Besides supplying instantaneous flow field information, PIV measurements are also used to obtain true-mean flow field and turbulence statistics by collecting a large number of vector maps and ensemble averaging them for that purpose. However, as mentioned earlier, this was not our aim at this stage of the investigation.

In the future, measurement of the ensemble averaged time-resolved velocity vector components with the reachable minimal experimental uncertainty could yield to an estimation of turbulence descriptors characterized by greater accuracy. This could be helpful to gain knowledge on the turbulence time scale of interest in prosthetic valve fluid dynamics. In fact, while for the spatial turbulent scale the ideal resolution is set by the dimensions of red cells and platelets, how to define the ideal temporal resolution is still open to conjecture (i.e., an interaction between blood corpuscles and smallest eddies takes place whenever the size of red cells/platelets and the smallest eddies are comparable,

resulting in the dissipation of eddies and energy transfer to the cell membrane). A possible approach could be to consider blood damage as an all-or-none phenomenon, setting the ideal temporal resolution as the lowest time of exposure to the higher stress value. However, this approach is not fully persuasive because it does not account for sublethal damages to blood cells.

Another limitation of the investigation may be identified in the simplified physical model of the aortic root as a stiff cylindrical duct, an assumption that introduces a smaller degree of similarity with respect to the in vivo fluid domain geometry. The role played by the sinuses of Valsalva in the fluid dynamics of the aortic root and in the behavior of the leaflets has been widely demonstrated (for a more in-depth discussion on the role played by the sinus of Valsalva see, for example, [120; 122; 123]).

The different behavior exhibited by the PHV in two different cycles at closure (under the same experimental conditions) could be ascribed to the unsteadiness of mock loops. However, according to [124], cyclic variations exist in the pulsatile flow, and the present investigation could also be seen as mimicking this behavior.

To maximize the ability of this technique to catch all relevant parameters of the flow, a stereo configuration of the cameras could be applied to reveal the 3rd velocity component. This out-of-plane component would obtain information about secondary flow development, however, it would require even more costly configuration of the hardware [92; 93; 125].

## **VI.6. Conclusion**

The type of measurements proposed in the present experimental study, which can be repeated in more realistic physical models, is a new powerful tool to be applied in the design of new devices. One area that is ripe for development is the extension of time-resolved PIV to measure velocities through a volume: higher camera and laser repetition rates may lead to an increase in both temporal and volume velocity information.

# VII. Flow Visualization Through Two Types of Aortic Prosthetic Heart Valves Using Stereoscopic High Speed Particle Image Velocimetry<sup>§</sup>

---

<sup>§</sup> The content of this chapter is accepted for publishing in  
Artificial Organs, 04.05.2007

**Flow visualization through two types of aortic prosthetic heart valves using stereoscopic high speed particle image Velocimetry.**

Radoslav Kaminsky, Stephan Kallweit, Hans-Joachim Weber, Tom Claessens, Krzysztof Jozwik, Pascal Verdonck

---

## Abstract

A novel method, Stereoscopic high speed PIV, was applied to quantify all three velocity components behind a prosthetic heart valve (PHV) in detailed time domain. In this study we compared a clinically used bileaflet ATS valve to a monoleaflet prototype of tilting disc PHV. The absolute velocities calculated out of two and three velocity components were compared to each other in order to estimate the overall difference in the desired region of interest. The most significant discrepancies between the two- and three-component absolute velocities were found at the regions of Valsalva sinuses and in a major jet stream of the monoleaflet PHV.

## VII.1.Introduction

Various studies on PIV have already demonstrated the benefits of visualizing the flow behind PHV. The first planar methods involving an image processing technique to investigate the flow behind a heart valve were first introduced by Affeld et al. [126], Lim et al. [127] and Daily et al. [128]. At that time, PIV analogue video techniques were used to acquire images. They were not only limited by their long interexposure time, but also by the required storage capacity and computer power for the subsequent calculation of the cross correlation algorithm among the acquired images.

A milestone in PIV was reached due to the advent of digital cameras for image acquisition and the fast evolution in computer performance. The era of the digital PIV (DPIV) approach started [129] and increased the capabilities of flow visualization behind the PHV. The evolution of digital cameras and computers paralleled the improvements of the PIV algorithms overall increased the accuracy and capability of PIV. A chronological summary of PHV studies by means of PIV up to 1997 was published by Brücker [130]. Also, a summary of laser techniques used for flow dynamics studies of PHVs was presented more recently in 2004 by Grigioni et al. [91].

The 2D PIV was the very first PIV technique variation. It is able to determine both components of the in-plane velocity vectors, and has widely been used during the past two decades [91; 130]. It has been proven, however, that the out-of-plane component (third velocity component) of the flow behind the heart valves can provide additional valuable information [85; 86; 94; 131; 132; 133]. Stereoscopic PIV has been developed to assess this out-of-plane velocity component. The technique was documented for the first time in 2003 in an investigation of the flow behind the PHVs [131; 132; 134]. A special case was demonstrated therein: a cross-sectional (instead of a longitudinal) cut of the mock aorta was measured [85; 86; 94; 132; 133; 134]. An extension of the stereoscopic PIV equipment with a traverse unit enables the possibility of

capturing the flow in a three-dimensional space by means of measuring more than one parallel region of interest in a discrete distance from each other [86; 133]. Further evolution of cameras and lasers allowed increasing the temporal resolution. A few studies on PHV fluid dynamics have been carried out with high speed cameras acquiring up to 1000 images per second. They were synchronized to a laser with the same pulse repetition rate. This combination is known as “High Speed” or “Time Resolved” PIV [109; 113; 114; 135]. Even higher rates of up to 3000 images per second at a resolution of 1024 x 1024 pixels have nowadays become feasible (see VI.) [109; 136]. High Speed PIV is able to generate the fully resolved temporal evolution of the flow downstream the PHV and also to map its complex dynamics characterized by its high non homogeneity and unsteadiness. Moreover, Time Resolved PIV permits to monitor the different flow fields in the supra-avalvular region of the bileaflet model at closure in two simulated cardiac cycles [136]. Different closing behaviour of the individual leaflets between the two cycles is a phenomenon, which, at conventional sampling rates, cannot always be detected. The “high speed” approach allows the analysis of complete, isolated working cycles, which is in contrast to conventional PIV, where the results are represented as a phase-locked average of instantaneous measurements over hundreds of cycles. Thus, it is possible to accurately capture the motion of the leaflets to determine in particular their closing behaviour.

PIV has already been used to assess the flow dynamics behind a PHV. However, we expect that the out of plane component may reach significant values compared to the in plane components, an issue which has not been studied before in particular in high temporal resolution. Therefore, in this study for the first time two high speed cameras were used in a stereoscopic configuration to acquire the time resolved velocity distribution over two different PHV's, and to assess the contribution of the out-of-plane velocity component. The frequently implanted ATS bileaflet PHV is taken as a reference in this study. Its flow dynamics have then been compared with the flow dynamics behind a prototype of a monoleaflet tilting disc PHV by means of stereoscopic high speed PIV.

To simulate the physiological conditions of a working aortic heart valve in a human body, an experimental set-up was designed with specific parameters matching the characteristic properties of the left heart, the aorta and the peripheral circulation. Such parameters include heart rate, cardiac output, aortic and ventricular pressure, as well as the material and shape of the ventricle and the aortic root and the placement of the PHV. A bileaflet and a monoleaflet PHV were inserted in this aorta to study their particular flow dynamics behaviour during a simulated cardiac cycle.

## **VII.2. Materials and methods**

### *VII.2.1. Mock loop*

The experimental set-up requires a transparent design and must allow for optimal optical access for the planned PIV approach. There are commercial and lab-specific mock loops available which allow measuring velocities by means of optical techniques. Commonly available commercial heart valve testing devices usually incorporate only rigid ascending mock aortas. In this study a commercially available Vivitro mock loop (Vivitro Systems Inc., Victoria, Canada) was used and adapted in order to replace the original mock aorta made out of rigid glass by a flexible and transparent silicone aorta.

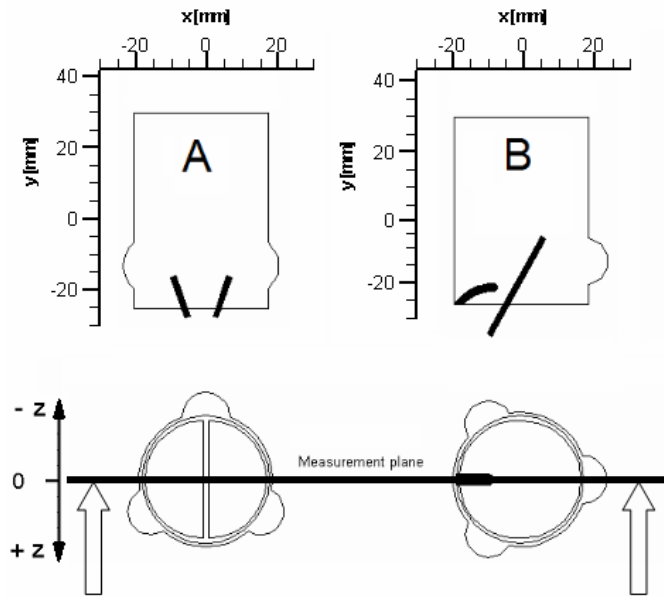
In order to bring the set-up closer to physiological conditions, the mock aorta should resemble a human aorta in terms of geometric and wall material properties [24; 137]. In particular, the diameter and wall elasticity (windkessel function) in radial as well as in longitudinal direction are important parameters to be matched. Such an aorta was designed at the University of Applied Sciences in Aachen, division Juelich, Germany [24]. It shows a high tearing resistance to sustain the anastomoses holding the valve. The thickness of the artificial aortic wall is homogeneous and well defined, and, as such,

avoids aneurysm-like inflation during systole. Moreover, it contains the sinuses of Valsalva to simulate physiologic flow and cusp dynamics.

The flexible silicone mock aorta had an internal lumen of 27 mm and wall thickness of about 1 mm. The modifications of the system and the mock aorta itself were performed to allow PIV measurements behind the aortic PHV. Further modifications were made on the measurement section in order to optimize the optical access and facilitate the stereoscopic approach (see section about the stereoscopic high speed PIV setup). An additional compliance chamber had to be designed to achieve a physiological pressure wave form [24].

Two different PHVs have been inserted into the mock aorta. The ATS (figure I-V) bileaflet valve (tissue annulus 25 mm) and a prototype of a monoleaflet tilting disc PHV (tissue annulus 24 mm), designed at Technical University of Lodz, Poland [21]. A PHV is clamped inside the mock aorta by a cable tie. Therefore, it is possible to acquire not only the movement of the valve's leaflet but also the relative movement of the valve. Once the leaflets are hitting the hinges during closing, the valve shortly changes its position downwards [109]. In diastole, it recovers its initial position.

Our main interest was to visualize the flow behind the leaflets. Consequently, we had to choose different orientations of the aortic Valsalva sinuses for the bileaflet and monoleaflet PHV, with respect to the measurement plane. The optimal anatomic position of both valves and respective measurement planes are illustrated in figure VII-I. The chosen region of interest (ROI) covered the area starting at the valve plane ( $y = -27$  mm) and ending at about 57 mm downstream ( $y = 30$  mm). The actual measured width of the ROI equalled 40 mm.



VII-I. Orientation of the A) bileaflet and B) monoleaflet PHV according to the sinuses in the mock aorta. The ROI was placed in the central plane of the aorta covering an area of  $57 \times 40 \text{ mm}^2$  ( $y = -27$  to  $30 \text{ mm}$ ;  $x = -20$  to  $20 \text{ mm}$ ). The arrows indicate the view direction in which results are presented (figure VII-IV, VII-V, VII-VI, VII-VII).

The measurements were performed separately for each valve under the same running conditions. The pulse duplicator was switched on approximately ten minutes before recording the PIV images. A mixture of glycerine and distilled water (37% / 63%) acted as a blood analogue fluid having a comparable density ( $\rho_{w,\text{fluid}} = 1.2 \text{ g.cm}^{-3}$  vs.  $\rho_{\text{blood}} = 1.06 \text{ g.cm}^{-3}$ ) and kinematic viscosity ( $\mu_{w,\text{fluid}} \sim \mu_{\text{blood}} \sim 3.5 \text{ mPa.s}$ ) [94]. Its refractive index was matching the refractive index of the silicone aorta ( $n_{\text{fluid}} = n_{\text{aorta}} = 1.41$ ). We, therefore, didn't observe any optical distortions. Red fluorescent particles ( $d_{\text{mean}} = 50 \text{ }\mu\text{m}$ ;  $\rho = 1.05 \text{ g.cm}^{-3}$ ;  $\lambda_{\text{excitation}} = 527 \text{ nm}$ ;  $\lambda_{\text{emission}} = 590 \text{ nm}$ ) were added to the working fluid as tracers.

The transvalvular pressure gradient was measured with capacitance-changing pressure sensors (Setra Systems Inc., Boxborough, MA, USA). They were connected to the valve tester by Luer connectors (Smiths Medical Germany GmbH, Kirchseeon / Eglharting, Germany). Flow was measured with an inductive flow sensor (Zepeda Instruments, Seattle, WA, USA). The entire data acquisition for volume flow and pressure was carried out using a customly

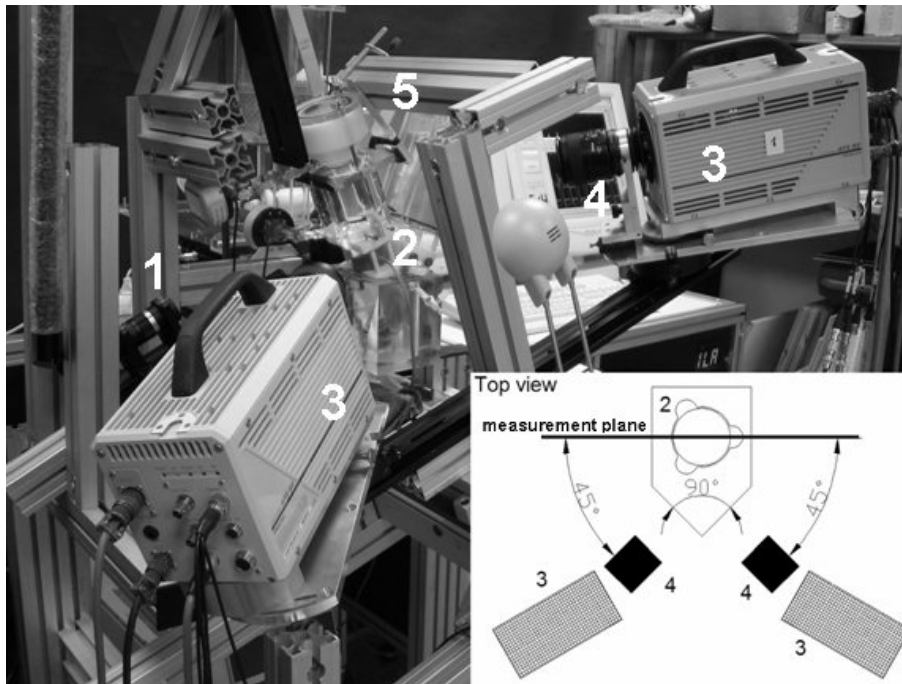
developed LabVIEW console (National Instruments Germany GmbH, Munich, Germany) with a sampling frequency of 3 kHz.

### VII.2.2. *Stereoscopic high Speed PIV set-up*

Two Photron APX-RS CMOS cameras (Photron, Marlow, UK) with a frame rate of 3 kHz and a resolution of 1024 x 1024 pixels have been used. Due to the limited amount budget, installed memory inside the camera was only 2.6 GB, which allowed to record images within a time interval of about 1.3 s at the acquisition sampling rate of 3 kHz and heart rate 1.3 Hz. For identical optical magnification two 60 mm f2.8 F-Mount Nikkor objectives, one for each camera, have been utilized. One camera was positioned to have a perspective view on the ROI under an angle of 45° from the left side of the measurement section. The other one was placed in the same way on the right side, as shown on figure VII-II. The camera bodies were mounted on customly designed tilt adapters (ILA GmbH, Juelich, Germany) to achieve the Scheimpflug conditions that are optimal for stereoscopic PIV [28]. A schematic drawing of the cameras' orientation is displayed in the bottom right corner of figure VII-II. A red bandpass filter ( $\lambda = 590 \pm 20$  nm) was placed in front of the CMOS sensor to eliminate the excitation wavelength of  $\lambda = 527$  nm. As such, only the fluorescing red light was allowed to pass through. Moreover, the wall reflections of the aortic wall and the leaflets of the PHV which could normally lead to erroneous signals were avoided.

A Nd:YLF double-cavity laser (New Wave Research, Fremont, US) was synchronized via the synchronizer (ILA GmbH, Juelich, Germany) to meet the frequency of 3 kHz of the recording cameras. The onset of the measurement sequence was triggered by the piston pump shortly before ventricular systole. This was accomplished in order to be able to record one full cycle (systole and diastole). The pulse distance, i.e. the time interval between the laser pulses illuminating the ROI and the actual image recording, was 333  $\mu$ s. Each laser cavity reached a maximum energy of 10 mJ, which was sufficient to illuminate our desired ROI. The laser beam was guided from the output of the laser head

through an articulated arm into the light sheet (LS) optics. The LS optics convert the laser beam to a plane aligned to the central plane of the mock aorta, parallel to the flow direction. On the opposite side of the LS optics, behind the housing of the mock aorta, a surface-coated mirror was arranged to redirect the LS in order to illuminate the area behind the leaflets. The detailed view of the PIV set-up is shown in figure VII-II.



VII-II. Detailed view on the stereoscopic high speed PIV set-up and a schematic top view on the components of the measurement section. The optics (1) are creating a light sheet, which illuminates the ROI from left towards the measurement section (2). The objectives (4) are inclined at a  $45^\circ$  angle with respect to the ROI, and the cameras (3) are tilted against the objectives to determine the so-called Scheimpflug conditions. The mirror (5) is reflecting the light sheet towards the valve to illuminate the area behind the leaflet in the period when the valve is open. The sketch in the bottom right part shows the strategic stereoscopic configuration of the cameras according to the measurement plane. The objectives (4) are in the Scheimpflug conditions with respect to the camera bodies (3) and measurement plane.

For the PIV image processing a commercial VidPIV 46XP (ILA GmbH, Juelich) software is used. For calibration a target with cross-markers was inserted in the ROI and images of both cameras were recorded. The stereoscopic algorithm uses a quadratic mapping function in  $x$ - and  $y$ - direction to map each pixel to real world coordinates. A misalignment error due to the not perfect

superposition of the cameras to the measurement plane was corrected by using the disparity map. The correction according to the disparity map was applied into the mapping function [138]. All recorded images were dewarped [51] with the corrected mapping function before the PIV evaluation took place. A first correlation, including Whittaker peak fit and phase correlation [49] was performed on 32 x 32 pixel (16 pixel overlap) interrogation windows. Then, a local median filter was applied after which the filtered vectors were interpolated. On the smoothed data an adaptive correlation function calculates the displacement on the 32 x 32 pixel (16 pixel overlap) interrogation windows. This processing step includes sub-pixel shifting and window deformation [50; 68] using grey value reconstruction by B-spline interpolation [70]. The complete sequence of the algorithm is iteratively performed in a tree-like structure. The overall spatial resolution of the vector distribution was 1.2 mm in both  $x$ - and  $y$ -direction.

To demonstrate the influence of the out-of-plane velocity component on the overall absolute velocity value, the absolute velocity calculated from two  $v(u, v)$  and from three  $v(u, v, w)$  velocity components is shown in the results section. The absolute velocity scalar values of  $v(u, v)$  and  $v(u, v, w)$  are calculated in the following way:

$$v(u, v) = \sqrt{u^2 + v^2} \tag{VII-1}$$

$$v(u, v, w) = \sqrt{u^2 + v^2 + w^2} \tag{VII-2}$$

where  $u$ ,  $v$  and  $w$  represent the velocity components along the  $x$ -,  $y$ - and  $z$ -axis, respectively.

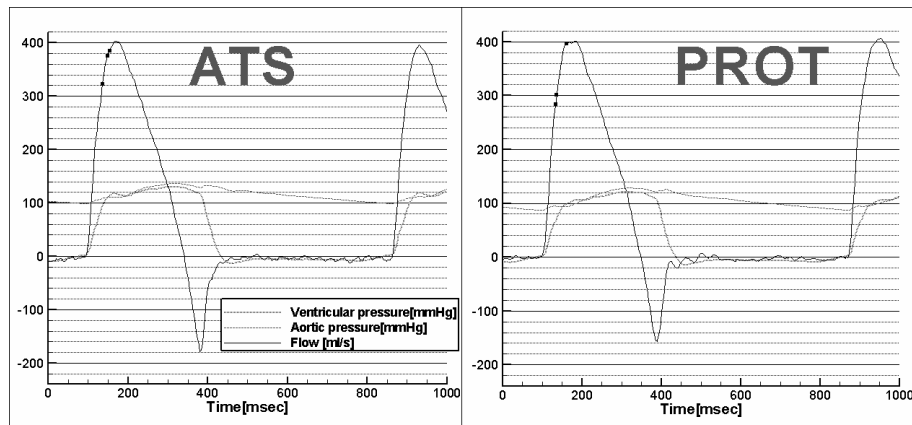
### VII.3. Results

The flow dynamics downstream of two different types of mechanical PHV's, a bileaflet ATS and a monoleaflet prototype of a tilting disc valve, were

investigated experimentally by means of stereoscopic high speed PIV. Pressure and flow parameters have also been monitored during one cycle.

### VII.3.1. *Bileaflet ATS valve*

In the first series of measurements with the bileaflet ATS valve, the stroke volume measured 60.9 ml/cycle. The regurgitation flow was 8.2 ml/cycle. The peak value for forward flow reached around 402 ml/s. The highest value for backflow reached 178 ml/s. The duration of the cycle was 770 ms (systole 288 ms vs. diastole 482 ms). The systole/diastole ratio was calculated to be 37.4/62.6 %. The plot on the left side in figure VII-III displays the measured ventricular aortic pressure and the volume flow. The volume flow results for ATS valve over the first cycle is shown in detail in the lower left panel.

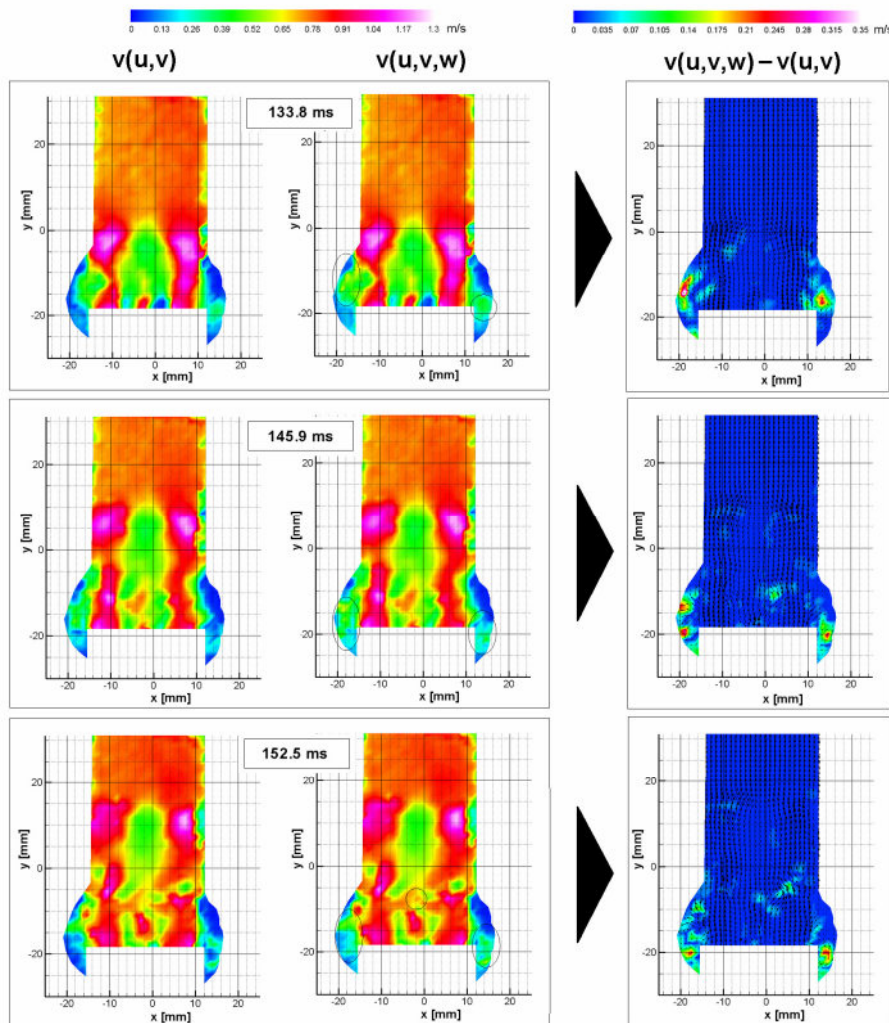


VII-III. Ventricular and aortic pressure [mmHg] and flow [ml/s] for the bileaflet ATS (left panel) and the prototype of the monoleaflet tilting disc valve PROT (right panel). The black dots on the flow curve indicate the time instances of PIV instantaneous flow fields shown later in following figures.

The onset of the PIV measurements is represented by  $t = 0$  ms. The quick rise in flow velocity magnitude in the vicinity of valve's leaflets indicates that the ATS valve starts to open at  $t = 93.2$  ms. In figure VII-IV the two and three-component velocity magnitude at three different time instants are shown. The major differences between both are marked with circles in figure VII-IV. In this paper, we specifically opted to display the results at these three time points

since the discrepancies between the two and three component are most prominent then. It should be noted, however, that the differences in velocity magnitude persist in almost the entire systolic period, but in a lesser degree.

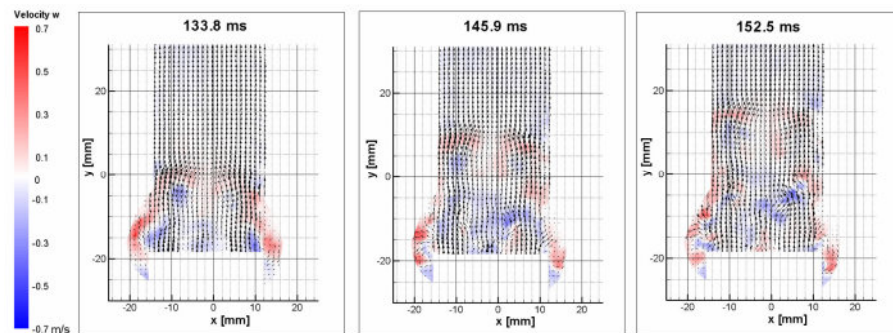
The flow development behind the ATS valve is a typical three-jet stream. In the early stage of ventricular systole, only the jet streams through the major orifices are present (not shown in here). However, at  $t = 133.8$  ms we already observe a third jet stream upon the middle orifice. At this time we also observe the first difference in magnitude of absolute velocities. In the regions near the sinuses the velocities  $v(u, v, w)$  show somewhat higher magnitudes compared to  $v(u, v)$ . The maximum difference approximates more than  $0.2 \text{ ms}^{-1}$ . The overall maximum velocity is about  $1.3 \text{ ms}^{-1}$  (figure VII-IV). The maximal values are located in the cores of side jet streams situated in the major openings of the bileaflet valve. At this initial systolic phase the central minor jet stream is only reaching velocities up to  $0.9 \text{ ms}^{-1}$ . No velocity mismatches by means of absolute velocity values were recognized in this region. At  $t = 145.9$  ms, the discrepancies persist in the regions of sinuses. At  $t = 152.5$  ms the major distinctions between the two and three component absolute velocity values are still present in the sinuses. Yet, there is also slight local higher value of the absolute velocity  $v(u, v, w)$  in the central part of the aorta, where the central jet stream is raising between the leaflets. We can't observe any clearly evident differences in the rest of the ROI.



VII-IV. Two-component (left) and three-component (middle) absolute velocity magnitude (color coded in m/s) behind a bileaflet valve at three different time instants. The corresponding time instants (in milliseconds) refer to the onset of the PIV acquisition. The circles point out the main differences between the  $v(u,v)$  and  $v(u,v,w)$ . The differences between  $v(u,v,w)$  and  $v(u,v)$  (right panel) are color coded using a specific velocity color scale with velocities up to 0.35 m/s.

The out-of-plane velocity component at the given time points are presented in figure VII-V in a two-dimensional view. The red colors indicate an out-of-plane velocity component in the positive direction, while the blue colors indicate a negative direction. The positive and negative directions are explained in figure VII-I. This view also presents the velocity vectors, and, as such, provides information about the flow direction within the entire ROI. In the first case ( $t =$

133.8 ms) the highest observed value of the out-of-plane velocity was about  $0.3 \text{ ms}^{-1}$  at the sinuses and downstream the lumen. At position  $y = 0 \text{ mm}$  the values reached about  $0.1 \text{ ms}^{-1}$ . At  $t = 145.9 \text{ ms}$  the out-of-plane component in Valsalva sinuses reach higher local maximum above  $0.3 \text{ m/s}$  close to the aortic wall. The neighbourhood of Valsalva sinuses gets weaker in magnitude. The increase of the third velocity component can be seen in the third image at  $y = 5 \text{ mm}$  representing the instantaneous flow field at  $152.5 \text{ ms}$  after the onset of the measurement. In the major area of the displayed ROI third component didn't reach a significant value at the respective time instants and even later in systolic period.



VII-V. The magnitude (m/s) of the out-of-plane velocity component is color coded. The positive and negative  $z$  direction of the velocity is indicated in figure 4. The velocity vectors behind the monoleaflet tilting disc prototype (PROT) are calculated out of  $u$  and  $v$  component only. The corresponding time instants refer to the onset of the PIV acquisition.

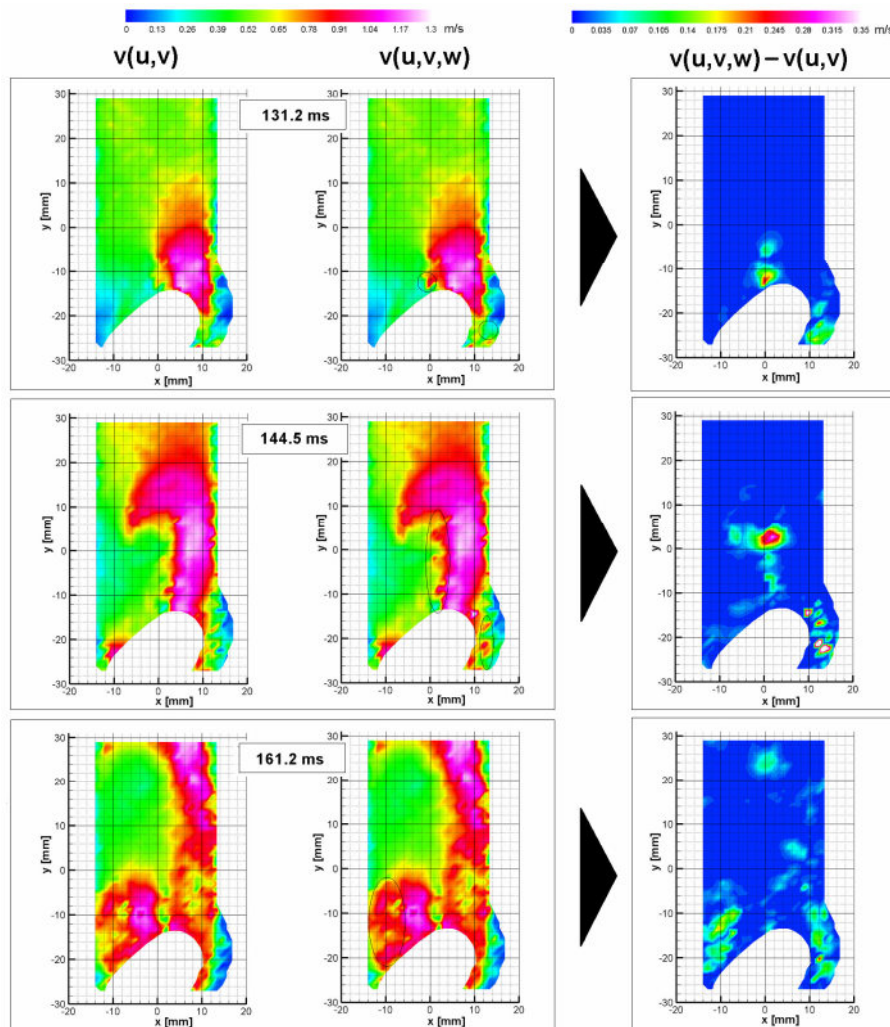
The local maximum of the out-of-plane velocity component tended to decrease to  $0.2 \text{ ms}^{-1}$  in the entire ROI (not shown). In the decelerating part of systole and the complete diastolic period of the heart cycle no values higher than  $0.2 \text{ ms}^{-1}$  were found.

### VII.3.2. *Monoleaflet PHV*

In the monoleaflet valve set-up the stroke volume was  $61.9 \text{ ml/cycle}$ . The regurgitating flow was  $7.6 \text{ ml/cycle}$ . The duration of the cycle was  $765 \text{ ms}$  (systole  $285 \text{ ms}$  vs. diastole  $480 \text{ ms}$ ). The systole/diastole ratio was calculated

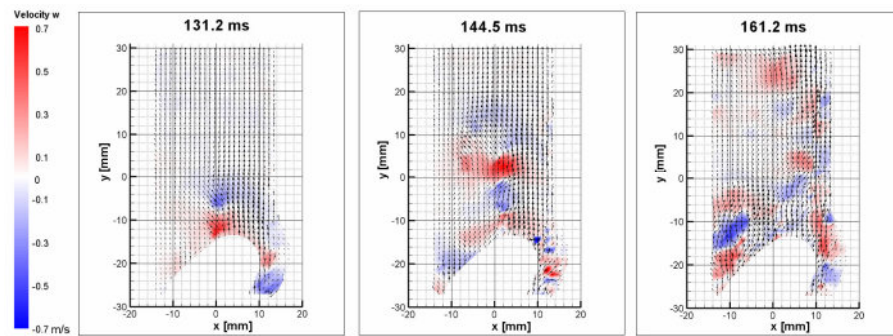
37.25/62.75 %. Figure VII-III (right panel) plots the measured ventricular and aortic pressure and the volume flow.

We observed that the monoleaflet PHV opens at  $t = 94.5$  ms, which is 1.2 ms later than the ATS valve. Figure 6 displays the absolute velocity magnitude of  $v(u,v)$  and  $v(u,v,w)$  at three different time instants.



VII-VI. Two-component (left) and three-component (middle) absolute velocity magnitude (color coded in m/s) behind a monoleaflet valve in three different time instants. The corresponding time instants (in milliseconds) refer to the onset of the PIV acquisition. The circles point out the main differences between the  $v(u,v)$  and  $v(u,v,w)$ . The differences between  $v(u,v,w)$  and  $v(u,v)$  (right panel) are color coded using a specific velocity color scale with velocities up to 0.35 m/s.

The out-of-plane velocity component behind the monoleaflet valve for the given time instants is presented in figure VII-VII in a two-dimensional view. In the first case ( $t = 131.2$  ms) the highest value of  $0.7 \text{ ms}^{-1}$  was observed above the leaflet's tip. In the middle of the ROI there were two spots with a high velocity magnitude, one with a positive and one with a negative out of plane direction. A small area in the Valsalva sinus region is also marked with red color, meaning that the velocity magnitude there was higher than  $0.3 \text{ ms}^{-1}$ . In the second case ( $t = 144.5$  ms) the observed spots with high velocity magnitudes appeared to have moved downstream the aorta for about 10 mm. In the same time the velocities in the blue areas tended to decrease in magnitude. The jet stream above the large orifice (right) was growing and the out of plane velocity values in the aortic sinus reached  $0.7 \text{ ms}^{-1}$ .



VII-VII. The magnitude (m/s) of the out-of-plane velocity component (color coded) and vectors plotted (as in Figure 5) behind the monoleaflet prototype of PHV.

At  $t = 161.2$  ms, a jet stream above the minor valve orifice was already present with out-of-plane velocity values reaching  $0.3 \text{ ms}^{-1}$ . The values in the Valsalva sinus approximated  $0.7 \text{ ms}^{-1}$ . However, a few local zones showing opposite directions were noticed. The flow downstream, in particular within the main jet stream, contained out-of-plane values from 0 up to  $0.7 \text{ ms}^{-1}$ . Later during flow development in systole, the out-of-plane velocities continuously decreased in magnitude but persisted in the entire ROI (not shown). During the deceleration systolic period and the complete diastolic period we did not observe any values higher than  $0.1 \text{ ms}^{-1}$ .

## VII.4. Discussion

The aim of this study was to visualize the three-dimensional flow distribution using a new method for investigating a flow dynamics behind a prosthetic heart valve (PHV), called stereoscopic high speed particle image velocimetry (PIV). The measurements were performed in order to quantify the flow behind the prosthetic aortic heart valve. This novel approach employs the benefits of stereoscopic PIV [85; 86; 130; 131; 132; 133; 134] and the dynamic approach of high speed (or time resolved) PIV [87; 109; 113; 114; 135; 136]. It enables one to assess all three velocity components with a very high temporal resolution.

The mock loop was designed to closely simulate the physiological conditions of an in vivo implanted PHV. The frequency of the pulse duplicator system was running at about 1.3 Hz, approximating the heart rate of a patient during normal activity. According to the monitored aortic/ventricular pressure ratio and volume flow [139], the duration of one cycle for a bileaflet valve ATS was 770 ms, whereas for a monoleaflet tilting disc it was 765 ms. Certain variability in the peaks of minimal values of volume flow among the monitored cycles for both valves was also observed. The regurgitation flow was for both valves close to 8 ml/s which is in the expected range [140; 141].

The PIV results confirm the expectations that the out-of-plane velocity component ( $w$ -component) plays a role in flows such as the ones behind PHV. In the major part of the ROI the difference between  $v(u, v)$  and  $v(u, v, w)$  was below  $0.1 \text{ ms}^{-1}$ . The out-of-plane velocity component behind the leaflets of the ATS valve reached  $0.3 \text{ ms}^{-1}$  in small regions of Valsalva sinuses in early systole (figure VII-V). At the same time instances the magnitude of absolute velocity  $v(u, v, w)$  was at certain local regions considerably higher than  $v(u, v)$  (figure VII-IV). However, the two-component velocity  $v(u, v)$  and three-component velocity  $v(u, v, w)$  do not differ significantly from each other behind the bileaflet PHV. When observing the velocity maps of a monoleaflet prototype valve, more evident differences in absolute velocity magnitude were found (figure VII-VI). The discrepancies between  $v(u, v, w)$  and  $v(u, v)$  among the three presented time instants for the two- and three-component velocities mainly occurred at the

area of the jet stream during early systole. The highly unsteady flow was confirmed by the fluctuating direction of the out-of-plane velocity component downstream the mock aorta reaching the maximum values close to  $0.7 \text{ ms}^{-1}$  (figure VII-VII). We consider  $0.7 \text{ ms}^{-1}$  third component velocity quite significant compared to absolute velocity of about  $1.4 \text{ ms}^{-1}$ . Certainly, for better visual comparison we chose the three time instances for both valves where the differences among two and three component absolute velocity values are more evident.

The stereoscopic approach for PIV measurements is somewhat hampered in terms of optical access. In figures in results section there are annotated (cut out) regions in an oval like shape just above the major orifice. Due to the stereoscopic view these regions are optically obstructed by open leaflet(s) during the systole period. Therefore, the stereoscopic PIV reconstruction of the out-of-plane velocity component cannot provide valid signals from that region. This optically occluded region is by the bileaflet valve remarkably smaller. The reason is that the leaflets of the bileaflet valve, even when fully opened, optically don't block an area as large as it happens by the monoleaflet model, because the leaflets are shorter.

It should also be noted that the used hardware components limited the acquisition time. Using speed cameras that are capable of recording longer time periods it will be possible to also perform statistical comparisons among several consecutive cycles. However, those cameras are much more expensive than the ones used in this study.

It is important to mention that the methods here presented are still planar. A stereoscopic high speed PIV featuring traverse units could lead to visualization of the flow behind a PHV in a three-dimensional volume.

## **VII.5. Conclusion**

Apparently, stereoscopic high speed PIV is a powerful tool to investigate the complex flow field behind PHV's. Its major benefit lies in its capability to visualize the third component of the velocity vector.

Our study shows that the third velocity component in the flow behind a PHV doesn't have a strong impact on the overall absolute velocity, especially in the bileaflet model. However, it has to be also noted that in small regions mainly in the regions of Valsalva sinuses and in the vicinity of leaflets the out-of-plane velocity values are reaching quite a high values during the accelerating systolic phase. It should be kept in mind when validating numerical codes (CFD), which are commonly 2D.



## VIII. PIV Validation of CFD Based Designs of Central Venous Hemodialysis Catheter\*\*

---

\*\* The contents of this chapter is accepted for publication in

Artificial Organs

**PIV validated CFD based design to reduce shear stress and residence time in central venous hemodialysis catheters.**

Guy Mareels, Radoslav Kaminsky, Sunny Eloot, Pascal Verdonck

---

## Abstract

As crucial factors in blood clot formation, shear stress (SS) distribution and low flow zones are assessed in different central venous catheter tip designs using a combined numerical and experimental approach. CFD was validated with PIV by comparing simulated and measured velocities and shear strains in three designs of the blood withdrawing 'arterial' lumen: cylindrical and with tip (1) cut straight, (2) cut at an angle, or (3) cut straight with a sleeve entrance. After validation, four additional designs were studied: (4) with two side holes and tip cut straight or (5) at an angle, (6) concentric lumens and (7) Ash Split based. In these seven designs, SS, blood residence time, and Platelet Lysis Index, which combines the influence of shear stress magnitude and exposure time, were simulated. Concentric catheter is discarded due to highly elevated SS. 'Ash Split' based design has elevated RT values in the distal tip zone as major inflow occurs through the most proximal side holes, but this is compensated by low average SS. A straight cut tip and possibly two side holes are preferred when aiming at minimal SS and RT. These data may lead to more patent catheters.

## VIII.1. Introduction

Central venous catheters are commonly used as a vascular access method for hemodialysis [142]. However, apart from several advantages as the ease of insertion and immediate access to the circulation, central venous catheter use is accompanied with a higher incidence of infection and thrombosis as compared to other means of vascular access like grafts or fistulas.[143] Concerning thrombosis, stagnating blood zones in the catheter lumen and regions of elevated shear stress which induce platelet activation may promote the formation of a blood clot. Elevated shear stress (SS) also give rise to damage to red blood cells. Significant levels of SS are mostly present in the blood withdrawing ('arterial') lumen of the catheter, more specifically in the distal tip region. Various different catheter (tip) designs are marketed whilst for the time being no proven advantage of one design over another exists. Nevertheless, changes in catheter tip design have shown to cause alterations in local flow pattern and SS distributions [144]. Further study of the local haemodynamics of different catheter designs might provide insight in how catheters can be optimized to reduce SS and stagnant zones thus leading to possibly less thrombogenic catheters.

In the first part of this study standard PIV was used to validate CFD by comparing simulated and measured velocities and shear strains in three designs of the 'arterial' lumen: cylindrical and with tip (1) cut straight, (2) cut at an angle, or (3) cut straight with a sleeve entrance. This was done to demonstrate the accuracy of CFD. Afterwards, in the second part of this study, to point out the useful implementation of validated results, we applied only CFD for further purely mathematical investigation of other catheter models. Following four additional designs were studied: (4) with two side holes and tip cut straight or (5) at an angle, (6) concentric lumens and (7) Ash Split based.

In the second part, flow and SS distributions and blood residence time (RT) in different catheter designs are compared. CFD allows a time efficient study of

the haemodynamics of different catheter designs without the time consuming effort of fabricating prototypes suitable for PIV measurements. However, validation of CFD results is necessary as mesh-independent SS fields, in contrast to flow fields, are difficult to achieve and are only obtained at very high (local) mesh density.[145] For this purpose, PIV was chosen as a challenging approach to obtain both high resolution flow fields and SS distributions *inside* the lumens of different catheter models.

Results of PIV and CFD approaches are compared to validate the numerical approach. Secondly, SS distributions and blood RT in four additional (in total seven) catheter designs are studied using CFD. Throughout the entire study, the distal end or tip of the arterial lumen is considered, as stagnant blood zones and highest SS are expected there [144]. Results are analyzed to assess which tip design is optimal to reduce SS levels and the presence of stagnating blood zones. Adoption of this information can lead to possibly less thrombogenic catheters.

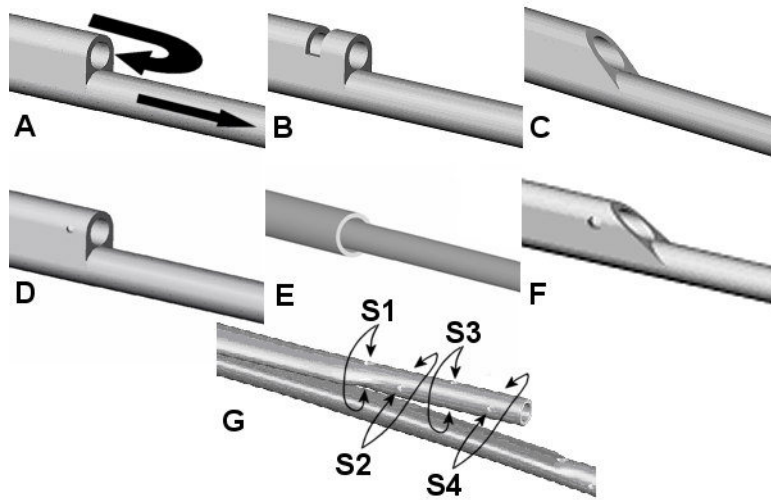
## **VIII.2. Materials and Methods**

### VIII.2.1. Catheter designs

#### *VIII.2.1.1. Three catheter designs studied by PIV and CFD*

Three catheters were studied by both PIV and CFD for flow and shear stress validation purposes. It concerned three shotgun (or step-tip) type catheters. The ‘arterial’ lumen, which withdraws blood from the vessel, has a circular cross section with an internal diameter of 2.1 mm. The ‘venous’ lumen, which returns cleansed blood to the circulation, is also cylindrical with an internal diameter of 2.1 mm, but its tip extends 30 mm further in length. The three catheters differed only in the tip design of the arterial lumen. The distal end of catheter ‘Cut Straight’ (figure VIII-IA) is cut orthogonally to its axis and has no other ‘arterial’ flow entrance than the distal end-opening. This is the most

simplistic catheter design and is considered as the reference catheter in the second part of this study. Catheter ‘Cut Straight Sleeve’ (figure VIII-IB) also has a distal end which is cut at 90° but it features a sleeve entrance (1.4 mm wide) at 3.1 mm distal from the ‘arterial’ tip. Catheter ‘Cut Angle’ (figure VIII-IC) has a distal end cut at an angle of 33° and only has one distal end-opening.



VIII-I. Catheter designs studied. A = Cut Straight; B = Cut Straight Sleeve; C = Cut Angle; D = Cut Straight Hole; E = Concentric; F = Cut Angle Hole; G = Ash Split based with four pairs of side holes S1-4.

#### VIII.2.1.2. Four additional catheter designs studied by CFD only

For the in-depth CFD study, four additional catheters were simulated. Catheter ‘Cut Straight Hole’ (figure VIII-ID) is a variant of catheter ‘Cut Straight’ but with two symmetrically placed side holes (inner diameter = 1.2 mm) at 3.1 mm distal from the ‘arterial’ tip. Catheter ‘Concentric’ (figure VIII-IE) is a typical concentric catheter design. The inner ‘venous’ lumen has an inner diameter of 2.1 mm. The surface area of the outer ‘arterial’ lumen annulus is also identical to the ‘arterial’ lumen surface area of the ‘Cut Straight’ catheter – to make comparison to the shotgun-type catheters valid. Catheter ‘Cut Angle Hole’ is analogously a variant of catheter ‘Cut Angle’ with two symmetrically placed side holes (inner diameter = 1.2 mm) at 3.1 mm

distal from the ‘arterial’ tip. The last catheter is based on the Ash Split design (Medcomp, Harleysville, PA, USA - figure VIII-IF). It has a D-shaped lumen which changes to a circular lumen with a smaller cross-section towards the tip (inner diameter = 1.8 mm). This catheter was scaled so the D-shaped lumen had the same surface area as the lumen in the reference catheter to allow comparison to other simulation results. It has four pairs of side holes (two pairs on top and bottom each alternating with two pairs on left & right of catheter lumen) extending the entire tip zone. Side holes most distal to the tip have a diameter of 1.3 mm; the other side holes have a diameter of 0.9 mm. Side holes are positioned at respectively 18.3 mm, 13.8 mm, 8.4 mm and 3.2 mm from the tip. The tip of the lumen is positioned under an angle of 3° to the horizontal axis.

The presented catheter designs are virtual designs. Nevertheless they bear high resemblance to existing commercially available catheters so results may be extrapolated to catheters of different manufacturers but with similar designs (e.g., Mahurkar, PermCath (Tyco Healthcare, Mansfield, Massachusetts, USA), Niagara, VasCath, OptiFlow (BARD Access Systems, Salt Lake City, Utah, USA), Duo-Flow and Split Cath (Medcomp, Harleysville, PA, USA)). Adoption of the results of this study may thus lead to better performing catheters.

### **VIII.3. PIV analysis**

#### VIII.3.1. Catheter prototypes

The three catheter prototypes were cast in an aluminum mold using a clear, homogeneous, transparent silicone (CF-2616, NuSil Silicone Technology, Carpinteria, California, USA) with RI of 1.41. To make casting more feasible, experimental catheter models were scaled so the inner diameter of the lumen is 6 mm. Consequently, a geometrical scaling factor  $\alpha_L$  of 2.857 (= 6 mm / 2.1 mm) was used for the entire *in vitro* set-up.

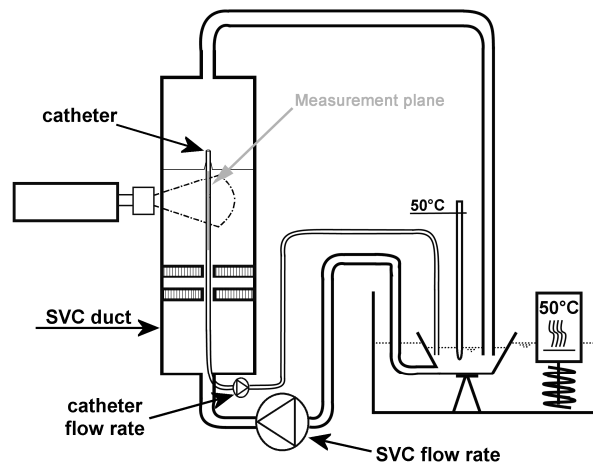
### VIII.3.2. Experimental setup

In vivo, the tip of a central venous catheter is located in the SVC, in the RA or at the junction of both. Previous work has shown that this location has little or no influence on flow or SS distribution *inside* the catheter lumens [144]. As such, *in vitro* the catheter is placed in a duct representing the SVC. Following *in vivo* parameters were assumed: catheter flow rate is 300 ml/min, blood density ( $\rho$ ) is 1060 kg/m<sup>3</sup>; blood dynamic viscosity ( $\eta$ ) is 3.5 mPa.s; SVC diameter (D) is 18 mm [146]; average blood velocity (v) in SVC during systolic inflow is 0.18 m/s [147], corresponding with a SVC blood flow rate of 2.7 L/min. According to the geometrical scaling factor, the hydraulic diameter of the *in vitro* duct has to be 51.4 mm. However, to minimize optical distortion and diffraction of the PIV laser on a curved surface, a rectangular PMMA duct was used. Hydraulic diameter of a rectangular duct equals four times the cross-sectional surface area divided by the circumference. As such, the cross-section of the duct was chosen to be 40 x 72 mm which complies with geometric similarity.

As a working fluid, a 42-58 weight % water-glycerin mixture was used at 50°C to reduce fluid viscosity. The mixture ( $\rho = 1150 \text{ kg/m}^3$ ) provides a RI of 1.41 matching with the catheter model material (manufacturer's data).. Kinematic viscosity ( $\nu$ ) of the mixture was determined experimentally using an Ubbelohde capillary viscometer (ViscoSystem AVS, Schott-Geräte GmbH, Germany). In five measurements at 50°C, mixture kinematic viscosity was measured  $2.961 \times 10^{-6} \text{ m}^2/\text{s} \pm 2.8 \times 10^{-9} \text{ m}^2/\text{s}$  Consequently, a dynamic viscosity ( $\eta = \nu \cdot \rho$ ) of 3.405 mPa.s was obtained. Subsequently, dynamic similarity theory was used to determine the *in vitro* flow conditions in the scaled PIV model. According to dynamic similarity, Reynolds numbers ( $Re = \rho \cdot D \cdot v / \eta$ ) in the *in vivo* and *in vitro* situation must be identical for both the catheter flow ( $Re = 937$ ) and the vein flow ( $Re = 981$ ). From this, an *in vitro* duct flow rate of 9.7 L/min and an *in vitro* catheter prototype flow rate of 784 mL/min were obtained. Consequently, a velocity scale factor  $\alpha_v$  of 0.314 and a shear rate scale factor  $\alpha_\gamma (= \alpha_v / \alpha_L)$  of

0.11 was calculated. These values are used to scale the results of PIV measurements for comparison with CFD results.

An experimental setup (figure VIII-II) was constructed in which the catheter was mounted securely in the rectangular duct. The working fluid is kept at a constant 50°C and continuously circulated through the duct mimicking the SVC blood flow rate, while another pump draws fluid via the arterial catheter lumen.



VIII-II. Schematics of PIV set up.

### VIII.3.3. Measurement protocol

For the flow visualization through the catheter model, standard PIV was used. Figure VIII-II shows schematics of the PIV set-up. As a light source for the measurements we used a double cavity Nd:YAG Solo PIV I (New Wave, Fremont) laser with  $\lambda = 532$  nm and 30 mJ of energy per pulse. An articulated mirror arm redirected the laser beam from the laser head to the light sheet optics. A 12bit CCD camera Sensicam QE (PCO, Kelheim) with a resolution of 1376x1040 pixels was used to record 100 pairs of images at 4 Hz frequency. A Nikor Micro 60 mm f2.8 lens was attached to the camera. To calibrate the ROI to real units (mm) we used a black aluminum plate with white cross-markers precisely written on it by a laser at given distances. The master of the

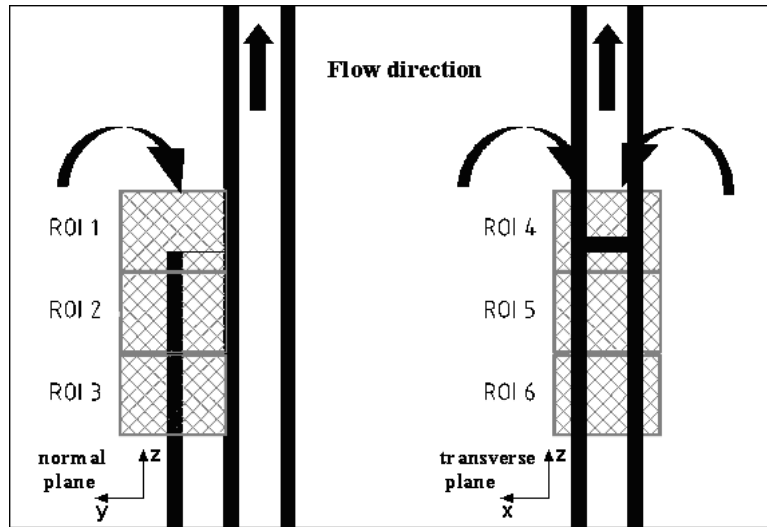
acquisition procedure was the synchronizer (ILA GmbH, Juelich), which controlled synchronized recording of the images to the emitted laser pulses in chosen frequency domain. The camera was orthogonally inclined to the laser LSO and both were fixed to the traverse unit allowing the positioning along the axis parallel to the main flow (figure VIII-II).

Rhodamine-B coated red fluorescent particles, micro-spheres of 10  $\mu\text{m}$  diameter, were added to the working fluid. Fluorescent particles emitted the red light ( $\lambda_{\text{emission}} = 580 \sim 620 \text{ nm}$ ) once they are illuminated with the green laser LS ( $\lambda_{\text{excitation}} = 532 \text{ nm}$ ). In order to avoid reflections at the wall of the catheter we applied a red band pass filter in front of the CCD sensor. Through this filter only red light ( $\lambda_{\text{band}} = 590 \pm 20 \text{ nm}$ ) was visible for the camera.

The resolution is given by an interrogation window size for the adaptive correlation of 32x32 pixels with an overlap shift of 8 pixels. The LS thickness was about 0.7 mm, with a spatial Gaussian distribution.

For three different catheters we measure three ROIs serially organized to the flow direction in two longitudinal central planes, normal and transverse (figure VIII-III). The combined ROIs in one plane covered approximately 13.7 x 32.8 mm<sup>2</sup> of the arterial catheter tip region.

For evaluation of the PIV images we used the commercial VidPIV software package (ILA GmbH, Juelich) with iterative window deformation [148], B-spline grey value interpolation [149] and phase correlation [150]. In all ROIs, ‘in plane’ velocity magnitudes and shear strain values were computed. The evaluation results are computed from a statistical average of 100 instantaneous flow field measurements for each ROI.



VIII-III. PIV measurement planes: normal and transverse plane were measured by combining three subsequent ROIs in each plane.

#### VIII.3.4. CFD analysis

All catheter models were constructed in *in vivo* scale in the CAD package SolidWorks 2003 (SolidWorks Corporation, Concord, MA, U.S.A.) and exported into the grid generation software Gambit 2.1 (Fluent Inc., Lebanon, NH, U.S.A.) via the Parasolid data format. Catheter models were inserted concentrically in an *in vivo* scale, straight, rigid cylinder representing the SVC. Fluent 6.2 was used as numerical solver.

##### VIII.3.4.1. Comparison with PIV

For comparison with PIV, blood was modeled as an incompressible, Newtonian fluid. Velocity inlet value of the SVC was set at a constant 0.18 m/s (cfr. *in vivo* flow conditions – supra). Catheter lumen boundary faces were set at 300 ml/min either entering or leaving the fluid domain. All walls in the model were set as rigid, impermeable and with no slip at the wall surfaces. SVC outlet face was set as a pressure outlet to provide a zero reference pressure. A T-Grid mesh was used, which was locally refined to gain better resolution for the

assessment of shear stress and to achieve grid independence. The resulting average number of grid cells in the tip volume was  $1.5 \times 10^6$  cells. ‘In plane’ velocities (Eq. VII-7) and shear strain values (Eq. VII-2) in the PIV measurement planes of the three catheters were computed and compared to the PIV results ( $u_i = i$ -component of velocity vector).

$$\begin{aligned} \text{velocity magnitude}_{\text{normal plane}} &= \sqrt{u_y^2 + u_z^2} \\ \text{velocity magnitude}_{\text{transverse plane}} &= \sqrt{u_x^2 + u_z^2} \end{aligned} \quad \text{VIII-1}$$

$$\begin{aligned} \text{shear strain}_{\text{normal plane}} &= -\left(\frac{\partial u_y}{\partial z} + \frac{\partial u_z}{\partial y}\right) \\ \text{shear strain}_{\text{transverse plane}} &= -\left(\frac{\partial u_x}{\partial z} + \frac{\partial u_z}{\partial x}\right) \end{aligned} \quad \text{VIII-2}$$

Quantitative comparison was performed by comparing numerical and experimental average velocity magnitudes and average (absolute values of) in-plane strain rates in the measurement planes.

#### *VIII.3.4.2. Assessment of shear stress levels and blood residence time*

In subsequent simulations to assess possible blood clotting risk in catheters, blood was modeled as a non-Newtonian fluid using the Quemada blood viscosity model [151]. More details on boundary conditions and parameters of CFD approach are described in [152].

As the flow inside the catheter lumen is proven to be three-dimensional [144], SS and blood RT were evaluated in a constant tip volume of the arterial lumen of each catheter model. A tip volume of 0.075 ml was considered, e.g., corresponding to the distal 2.16 cm end of the arterial lumen in the ‘Cut Straight’ reference catheter. Volume averaged SS in this tip zone is calculated for all catheters. A shear stress threshold of 10 Pa for platelet activation was selected [153]. As such, also the percentage of the tip volume which is subjected to a shear stress of 10 Pa or more is calculated for each catheter. Concerning residence time, the average value of parameter ‘ $t$ ’ at the end of the tip volume

is 0.015 s for each catheter, given the tip volume and the catheter blood flow rate. However, due to local stagnation of blood in the tip zone the time since the blood has entered the ‘arterial’ lumen can locally exceed 0.015s. Consequently, the percentage of tip volume with  $RT > 0.015$  s and the percentage of tip volume with  $RT > 0.030$  s was evaluated for each catheter design. Extended residence time combined with elevated SS can lead to platelet activation and eventually blood clotting. As such, also the average SS in zones with  $RT \leq 0.015$ s and in zones with  $RT > 0.015$ s was calculated for each catheter design.

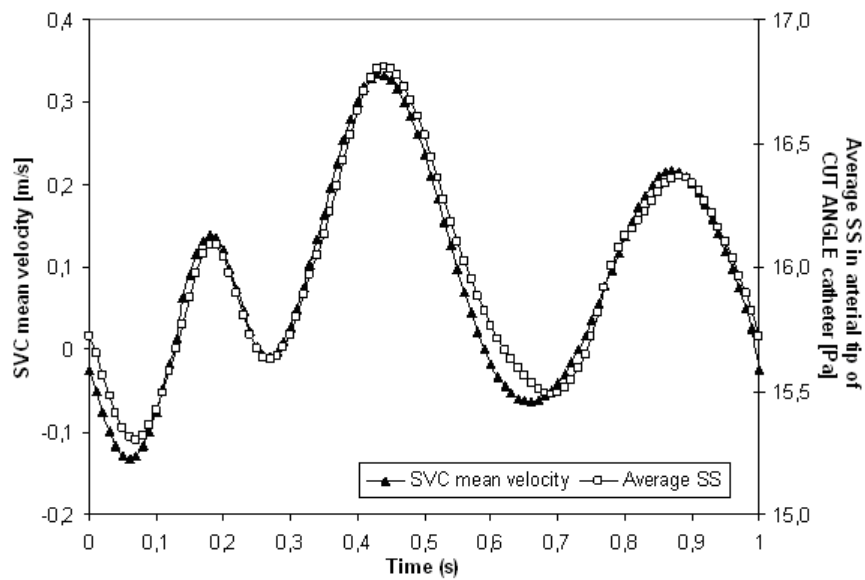
The choice of the 10 Pa SS threshold for platelet activation can be questioned as the range of SS over which platelet adhesion and subsequent aggregation are observed is approximately 0.1 to 20 Pa [154]. Waniewski *et al.*[155] use a two level critical threshold of  $2500 \text{ s}^{-1}$  ( $\sim 8.75$  Pa) to  $7500 \text{ s}^{-1}$  ( $\sim 26.5$  Pa) to assess the conditions of thrombosis. As such, to reduce the sensitivity of the results and conclusions of this study to the choice of the SS threshold, the Platelet Lysis Index [156; 157] (PLI) was added. Similar to the Hemolysis Index equation by Giersiepen [156], this experimentally fitted equation describes the lysis of a platelet, taking into account the combined effect of magnitude of SS and the exposure time.

This approach allows linking high SS to subsequent low flow zones via path lines. Although the equation is set up for platelet lysis, it can be used to assess possible platelet activation as the same determinants are applicable. As such, the index is used as a comparative tool in the quantitative assessment of the catheter tip designs, rather than as a predictive tool of actual platelet activation.

For each inlet of a catheter, a minimum of 1000 path lines were computed by Fluent 6. Each path line takes 3000 steps of  $10 \mu\text{m}$  to allow the path line to extend well past the disturbed flow in the tip zone and into the Poiseuillian flow further downstream the catheter lumen. At every point, shear stress and velocity magnitude values are exported. The time value is computed as the distance between subsequent points along a path line divided by the average velocity over the segment. PLI values of every step along a path line are

summed up. Subsequently, for each catheter a weighed average of all path line PLI values is computed using the entrance velocity of a path line as weighing factor. As such, each path line contributes to the PLI according to the amount of catheter inflow they represent.

A realistic superior vena cava (SVC) velocity profile [147] was imposed in one case ('Cut Angle') to assess the influence of pulsatile flow and even backflow in the catheter surrounding vein. Figure VIII-IV shows the velocity profile [147] (period = 1s) imposed at the vein inlet face. Average SS in the tip was monitored during the 2<sup>nd</sup> cycle to avoid transitional flow effects.

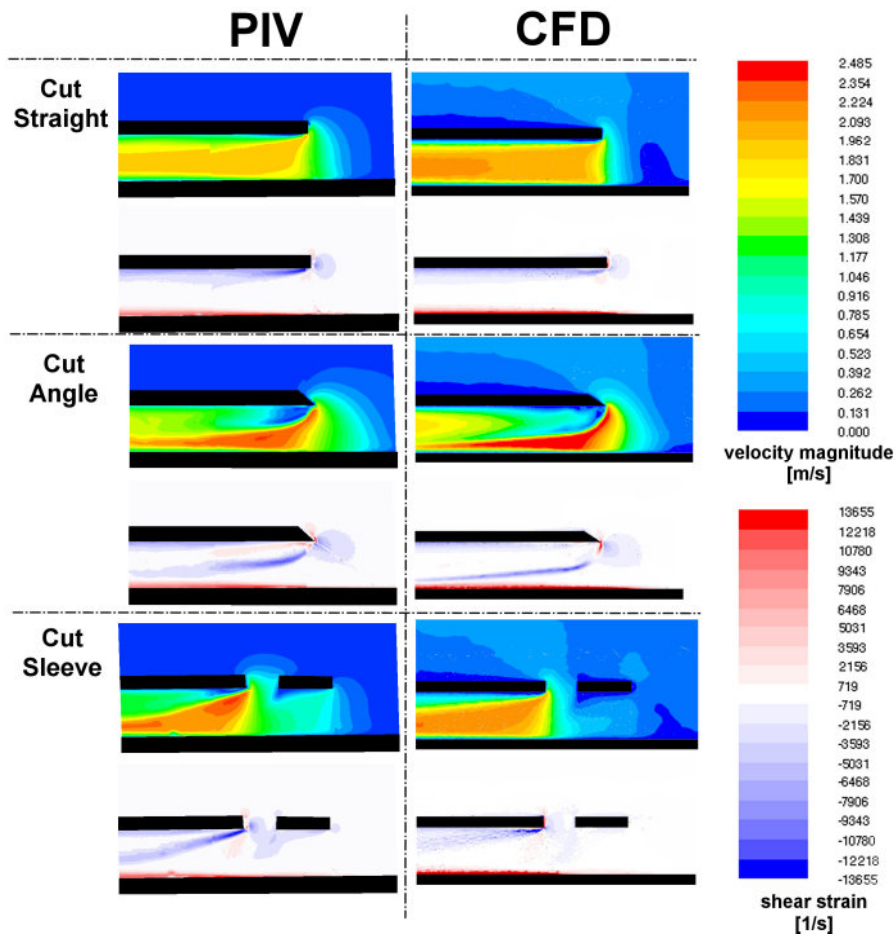


VIII-IV. Realistic time-dependent superior vena cava average inlet velocity (m/s) and average SS (Pa) in catheter 'Cut Angle' tip under these transient conditions.

## VIII.4. Results

### VIII.4.1. *CFD validation by PIV measurements for three catheter designs*

Figure VIII-V shows ‘in plane’ velocity magnitudes and strain rates in the normal and transverse plane of the three catheters studied. The range of velocity magnitude and shear strain is set equal for PIV and CFD.



VIII-V. CFD and PIV results of in-plane velocity and shear strain distribution defined according to Eq. VII-2 in two orthogonal planes in the ‘arterial’ lumen tip of three catheter models (Cut Straight, Cut Angle and Cut Straight Sleeve).

The inflow in the ‘Cut Straight’ catheter is homogeneous in both, the normal and transverse plane. Only very small zones of low velocity and flow separation are present just downstream the inlet and are both visible in PIV and CFD. Shear strains are highest near the inlet where the flow bends around the catheter entrance and near the border of the small recirculation zone and the large inflow. In case the inlet of the catheter is cut at an angle of  $33^\circ$  (‘Cut Angle’), a large zone of low velocities is present close to the top of the ‘arterial’ lumen. Maximal velocity values are higher as compared to the catheter ‘Cut Straight’ as the effective inflow area is reduced. In the transverse plane, velocities are high near the wall and low in the center of the lumen. This illustrates how the major flow enters the lumen. The incoming flow bends to the bottom of the lumen and flows to the top along the side walls and comes back down more downstream in the center of the ‘arterial’ lumen. This swirling motion during arterial inflow was already observed in previous work.[144] As a result of the complex three-dimensional flow, high shear strains are present throughout the tip of the ‘Cut Angle’ catheter. Adding a sleeve entrance to the straight cut catheter (‘Cut Straight Sleeve’) results in low velocities in the most distal zone of the catheter’s tip. The majority of the flow is now drawn into the lumen through the sleeve. A zone of low velocities is noticed near the wall just downstream the sleeve and as well as a relatively large zone near the top of the lumen in the most distal zone extending to the center of the lumen. As such, high strain rate values are mostly present near the sleeve wall and at the bottom of the lumen.

Results show that PIV measurements and CFD simulations are in good qualitative agreement in all cases for both, the velocity magnitudes and the shear strain values. However, some mismatches can be recognized visually. The intake flow in case of ‘Cut Straight’ catheter is measured by PIV to be higher in the upper part of the lumen. The CFD results show rather symmetric intake at the inlet. In case of ‘Cut Angle’ catheter the stagnant flow region just behind the inlet is somewhat larger estimated by PIV compared to CFD. Moreover, we can observe evident difference of the velocity magnitude inside

the major inlet lumen of ‘Cut Sleeve’ model. Quantitative comparison is presented in Table I-1.

		Cut Straight (ref.)	Cut Angle	Cut Straight Hole	Cut Angle Hole	Cut Straight Sleeve	Conc.	Ash Split based
Flow division	End opening	100 %	100 %	48.8 %	46.6 %	18.0 %	100 %	6.6 %
	Side entrance	N/A	N/A	51.2 %	53.4 %	82.0 %	N/A	S4: 4.2% S3: 8.6% S2: 15.6% S1: 65.0%
avg. SS		12.6 Pa	16.3 Pa	14.2 Pa	14.6 Pa	12.8 Pa	44.8 Pa	11.6 Pa
			<b>+29%</b>	<b>+13%</b>	<b>+167%</b>	<b>+2%</b>	<b>+255%</b>	<b>-8%</b>
% vol. SS > 10 Pa		41.8 %	54.7 %	45.8 %	47.9 %	41.0 %	87.9 %	32.2 %
			<b>+31%</b>	<b>+10%</b>	<b>+15%</b>	<b>-2%</b>	<b>+110%</b>	<b>-23%</b>
% vol. RT > 0.015 s		16.8 %	13.9 %	9.8 %	10.2 %	19.7 %	18.9 %	60.8 %
			<b>-17%</b>	<b>-42%</b>	<b>-39%</b>	<b>+17%</b>	<b>+13%</b>	<b>+262%</b>
% vol. RT > 0.030 s		0.1 %	2.6 %	0.1 %	0.1 %	2.7 %	8.3 %	31.4 %
			<b>x 26</b>	<b>x 1</b>	<b>x 1</b>	<b>x 27</b>	<b>x 83</b>	<b>x 314</b>
avg. SS where RT ≤ 0.015 s		10.7 Pa	15.3 Pa	13.4 Pa	13.7 Pa	10.6 Pa	37.1 Pa	11.0 Pa
			<b>+43%</b>	<b>+25%</b>	<b>+28%</b>	<b>-1%</b>	<b>+247%</b>	<b>+3%</b>
avg. SS where RT ≥ 0.015 s		21.3 Pa	22.7 Pa	21.3 Pa	22.6 Pa	22.0 Pa	77.6 Pa	12.0 Pa
			<b>+6%</b>	<b>0%</b>	<b>+6%</b>	<b>+3%</b>	<b>+264%</b>	<b>-44%</b>
Platelet Lysis Index - PLI		0.0071	0.0448	0.0154	0.0249	0.0497	0.1260	0.0357
			<b>x 6.3</b>	<b>x 2.2</b>	<b>x 3.5</b>	<b>x 7.0</b>	<b>x 17.7</b>	<b>x 5.0</b>

Table VIII-1. Quantitative comparison of PIV and CFD results of average velocity magnitude and average absolute value of strain rate in the two PIV measurement planes of the three catheters studied using both PIV and CFD (Cut Straight, Cut Angle and Cut Straight Sleeve).

#### VIII.4.2. *CFD assessment of SS and RT in the tip of 7 catheter designs*

The following parameters were assessed in the tip zone of the ‘arterial’ lumen of each catheter: (1) tip volume average SS, (2) percentage of tip volume with SS > 10 Pa, (3) percentage of tip volume with RT > 0.015 s, (4) percentage of tip volume with RT > 0.030 s, (5) average SS in zones with RT ≤ 0.015 s, (6)

average SS in zones with RT > 0.015 s and (7) PLI. Also flow division is reported in case of different flow entrances. Results are presented in Table VIII-2. Catheter ‘Cut Straight’ is set as the reference catheter as its design is no more than just a simple cylindrical lumen.

		Cut Straight (ref.)	Cut Angle	Cut Straight Hole	Cut Angle Hole	Cut Straight Sleeve	Conc.	Ash Split based
Flow division	End opening	100 %	100 %	48.8 %	46.6 %	18.0 %	100 %	6.6 %
	Side entrance	N/A	N/A	51.2 %	53.4 %	82.0 %	N/A	S4: 4.2% S3: 8.6% S2: 15.6% S1: 65.0%
avg. SS		12.6 Pa	16.3 Pa <b>+29%</b>	14.2 Pa <b>+13%</b>	14.6 Pa <b>+167%</b>	12.8 Pa <b>+2%</b>	44.8 Pa <b>+255%</b>	11.6 Pa <b>-8%</b>
% vol. SS > 10 Pa		41.8 %	54.7 % <b>+31%</b>	45.8 % <b>+10%</b>	47.9 % <b>+15%</b>	41.0 % <b>-2%</b>	87.9 % <b>+110%</b>	32.2 % <b>-23%</b>
% vol. RT > 0.015 s		16.8 %	13.9 % <b>-17%</b>	9.8 % <b>-42%</b>	10.2 % <b>-39%</b>	19.7 % <b>+17%</b>	18.9 % <b>+13%</b>	60.8 % <b>+262%</b>
% vol. RT > 0.030 s		0.1 %	2.6 % <b>x 26</b>	0.1 % <b>x 1</b>	0.1 % <b>x 1</b>	2.7 % <b>x 27</b>	8.3 % <b>x 83</b>	31.4 % <b>x 314</b>
avg. SS where RT ≤ 0.015 s		10.7 Pa	15.3 Pa <b>+43%</b>	13.4 Pa <b>+25%</b>	13.7 Pa <b>+28%</b>	10.6 Pa <b>-1%</b>	37.1 Pa <b>+247%</b>	11.0 Pa <b>+3%</b>
avg. SS where RT > 0.015 s		21.3 Pa	22.7 Pa <b>+6%</b>	21.3 Pa <b>0%</b>	22.6 Pa <b>+6%</b>	22.0 Pa <b>+3%</b>	77.6 Pa <b>+264%</b>	12.0 Pa <b>-44%</b>
Platelet Lysis Index – PLI		0.0071	0.0448 <b>x 6.3</b>	0.0154 <b>x 2.2</b>	0.0249 <b>x 3.5</b>	0.0497 <b>x 7.0</b>	0.1260 <b>x 17.7</b>	0.0357 <b>x 5.0</b>

Table VIII-2. The following parameters were calculated in the tip zone of the ‘arterial’ lumen of each catheter: (1) tip volume average SS, (2) percentage of tip volume with SS > 10 Pa, (3) percentage of tip volume with RT > 0.015 s, (4) percentage of tip volume with RT > 0.030 s, (5) average SS in zones with RT ≤ 0.015 s, (6) average SS in zones with RT > 0.015 s and (7) PLI. Percentages show relative difference compared to reference (ref.) case.

Tip volume average SS in ‘Cut Straight’ catheter attains 12.5 Pa. Cutting the inlet at an angle increases average SS with about 30%. Incorporation of side holes renders quasi-identical results irrespective of the angle at which the inlet is cut and leads to about 14-17 % higher SS as compared to the reference case. Adding a sleeve entrance does not significantly change tip average SS as compared to the reference catheter. A 3.6-fold avg. SS compared to the reference case is noticed when a concentric catheter design is used. Using an

Ash Split design reduces average SS with about 7%. Similar trends are noticed in the percentages of volume where SS attains 10 Pa or more.

The percentage of volume with a  $RT > 0.015$  s is reduced when the end opening is cut at an angle compared to a straight cut with about 17%. Addition of side holes to catheter 'Cut Straight' or 'Cut angle' both reduce the volume with  $RT > 0.015$  s with more than a third compared to the reference case; adding a sleeve to the 'Cut Straight' catheter, however, increases the volume with  $RT > 0.015$  s with about 17%, as well as again increasing the amount of volume with  $RT > 0.030$  s to 2.7%. 'Concentric' catheter has 13% more zones with  $RT > 0.015$ s in its tip zone, but an 83-fold of volume with  $RT > 0.030$  s. The largest increase in percentage of volume with  $RT > 0.015$  s and  $> 0.030$  s was found in the 'Ash Split' catheter tip compared to the reference catheter.

Looking at the SS levels in zones with different RT levels, SS is approximately 21 Pa in zones with  $RT > 0.015$  s and approximately 11 Pa in zones with  $RT < 0.015$  s. In case of 'Cut Angle', 'Cut Straight Hole' and 'Cut Angle Hole' the change in tip averaged SS is due to a change in SS levels in zones with  $RT < 0.015$  s. In catheter 'Ash Split' the change in average SS is mostly due to the change in SS levels in zones with  $RT > 0.015$  s. In case of 'Concentric' catheter, the rise of average SS level compared to the reference case is equally pronounced in both RT interval zones.

As for average SS and RT parameters, the PLI is lowest for the reference catheter 'Cut Straight'. Trends for PLI values do not always clearly follow the SS or RT values as both parameters are used to calculate the PLI. Catheter classification according to the lowest PLI is: 'Cut Straight' < 'Cut Straight Hole' < 'Cut Angle Hole' < 'Ash Split based' < 'Cut Angle' < 'Cut Straight Sleeve' < 'Concentric'.

## **VIII.5. Discussion**

For the first time, flow inside a catheter lumen was assessed using PIV. This was highly successful due to maximal reduction of optical distortion by

matching the RI of the fluid and catheter material and by using red fluorescent particles, while respecting dynamic similarity theory. As such, standard PIV was enhanced to allow the application to this small scale geometry. Very high resolution of velocity measurements was achieved, even to such a level that it was possible to accurately compute first order derivatives (shear strains). Validation of CFD with PIV was found to be relevant and necessary to prove the capability of the simulating technique. Quantitative agreement between PIV and CFD results was reported in Table VIII-1. Several mismatches can be determined also visually (figure VIII.3.4.1). The inconsistency of the absolute values can be based on a slight translational displacement of the LS to the exact position of the normal and transverse plane in CFD, which causes obvious differences in maximal and overall velocity magnitude and consequently SS distribution. Nevertheless, the relative velocity distribution mismatch is probably resulting from the limited capability of the CFD to truly simulate the experimentally visualized flow. The relative errors for the average velocity values in the normal planes are below 15%. The errors in the transverse planes are larger, but this can be understood when looking at the flow field. The slow flow zone downstream the end-opening (and sleeve) is located at the top of the lumen. As such, the measurement results are more prone to 'vertical' shifts of the transverse plane (adding the risk of missing the slow flow zone when not measuring close enough to the top of the lumen) than to 'lateral' shifts of the normal plane. To illustrate the sensitivity of the results to the exact positioning of the measurement planes, average velocity and strain rate values were computed for a slightly shifted plane for both normal and transverse planes. In case of the Cut Straight Sleeve catheter, the relative error on velocity magnitude is reduced from 34.4% to 8% with a plane shift of only 0.5 mm in the transverse plane. A slight rotational displacement of the PIV laser sheet is, e.g., evident in the PIV results of the transverse plane of catheter 'Cut Angle' (figure VIII-V.), where an asymmetrical flow was measured. The quantitative discrepancy between PIV and CFD may be further reduced by devising a procedure for a more accurate positioning of the PIV measurement planes in future work.

After validation of numerical results with PIV, a second goal of this work was to study possible thrombogenicity of different central venous catheter designs. The methodology used in this study solely concentrates on flow and SS parameters inside the catheter lumens.

Apart from high SS, areas of flow stagnation or recirculation that are characterized by longer RT may implicate platelet aggregation. Flow induced platelet activation and aggregation has been shown in stenosed human coronary arteries [158] where a volume average SS of approximately 46 Pa and an average transit time of approximately 0.004 s can be calculated (based on an average stenotic diameter of 1.1 mm, 5 mm in length, a peak diastolic blood flow rate of 73 ml/min, average wall SS of 70 Pa along the stenosis wall and assuming a linear SS profile across the artery lumen). Given the comparable settings regarding SS and RT values, the results of this study are considered relevant and may prove to be of importance in order to minimize risk of blood clotting. *In vitro* validation however may be useful to ascertain the results of this numerical study.

Catheter 'Cut Straight' was set as a reference model as it represents the simplest tip design: a straight cylindrical tip. Blood inflow is highly homogeneous. The tip volume averaged SS attains 12.6 Pa. Theoretically, the average SS in laminar flow through a cylinder under the simulated conditions is approximately 12.5 Pa (calculated with constant  $\eta = 3.4$  mPa.s). As such, little additional shear stress is induced by the catheter inflow design. Due to the homogeneous inflow, RT values larger than 0.030 s are virtually non-existent. This indicates that almost no local recirculation or zones with low velocities exist in the catheter tip. As a consequence of the low SS and RT, PLI is lowest for this catheter.

Cutting the end opening at an angle (Cut Angle) reduces the effective inflow area as blood is drawn into the 'arterial' lumen as close as possible to the driving force (i.e. pump). This leads to relatively increased SS levels as compared to the reference catheter. The more complex three-dimensional inflow gives a slightly better wash-out of blood residing near the wall (= zones

with high RT), reducing the percentage of volume with  $RT > 0.015$  s. Nevertheless, wash-out is not complete near the inlet as a zone with a significant RT is present near the most distal end of the tip zone, significantly increasing the volume with  $RT > 0.030$  s as compared to the reference case. The combination of elevated SS and RT causes the PLI to increase to a more than six fold value as compared to the 'Cut Straight' catheter.

Adding side holes to the reference catheter (Cut Straight Hole) strongly reduced the percentage of volume with  $RT > 0.015$  s indicating that the side holes provide a more disturbed flow patterns near the wall and consequently a better wash-out near the wall. However this is at the cost of a slightly increased SS level. Adding side holes to the angular cut catheter (Cut Angle Hole) disturbs the inflow pattern and reduces the size of the slow flow zone near the distal tip of the lumen. Consequently, regions with  $RT > 0.030$  s have almost disappeared, while the larger effective inflow area decreases average SS. Also, since side holes provide slightly more than 50% of the total blood inflow rate, the importance of the distal end-opening is reduced. So, quasi-identical results are obtained when adding side holes to the 'Cut Angle' catheter as compared to the 'Cut Straight Hole' catheter and PLI level for catheters with side holes is between the 'Cut Straight' and 'Cut Angle' designs.

Adding a sleeve to the reference design (Cut Straight Sleeve) causes low entrance velocities in the most distal tip zone as more than 80% of the flow enters through the sleeve. More zones with elevated RT are now present: an almost doubled percentage of volume with  $RT > 0.015$  s as compared to using side holes.  $RT > 0.030$  s zones are at the same level as in 'Cut Angle'. Although average SS levels are maintained at the level of the reference catheter, PLI of 'Cut Straight Sleeve' is strongly elevated, slightly higher than 'Cut Angle'

Although the inflow surface area of the 'Concentric' catheter is identical to the reference catheter and inflow is homogeneous throughout the end opening, the higher SS levels in the 'Concentric' catheter are a consequence of the annular design of the inflow surface. The latter has more inner wall surface, forcing the flow through the thin area between the two walls. Moreover, because of the

flow separation near the entrance, percentage of tip volume with  $RT > 0.030$  s is also highly elevated. Consequently, this catheter accounts for the highest PLI of all tip designs studied.

The 'Ash Split' based design has multiple side holes which give a more spread inflow pattern. This accounts for the lowest average SS levels of all catheters studied. However, as more than 80% of the incoming flow is drawn by the two most proximal pairs of side holes, the most distal region of the tip is characterized by very low velocities. This observation can be extrapolated to every catheter design which uses multiple (sets of) side holes which are located longitudinally across the tip length as the most proximal holes receive the largest blood flow and increase the residence time in the low flow distal tip region. This strongly increases local RT values causing blood in about a third of the tip volume to be present in the tip zone for longer than twice the average RT of blood passing through the tip zone. For this catheter with a different trend in SS and RT levels, the PLI parameter allows to assess how the combination of decreased SS and increased RT influences the classification of this design according to possible platelet activation. PLI of 'Ash Split type' is between values of the tip designs with side holes and the 'Cut Angle' design. So, although RT are highest of all tips studied, the less than linear dependence of PLI on exposure time causes the PLI value to be far lower than the PLI of the 'Concentric' catheter.

Concerning the influence of pulsatile SVC flow, as average SS in the catheter tip closely follows SVC flow rate, catheter classification according to thrombogenicity is not expected to change.

## **VIII.6. Conclusion**

The 'Concentric' catheter is discarded due to the highly elevated SS levels. 'Ash Split' based design has elevated residence time values in the distal tip zone as major inflow occurs through the most proximal side holes, as can be expected with catheter designs with multiple side hole along its tip. This numerical

study recommends using the reference catheter ‘Cut Straight’ as a minimal risk to platelet activation. Catheters ‘Cut Straight Hole’ and ‘Cut Angle Hole’ render second-to-best results, showing that adding two (relatively large) side holes, symmetrically placed close to the tip are not detrimental to the catheter performance. Catheter ‘Cut Angle Hole’ (with end opening cut at an angle and with two lateral side holes close to the tip) may be preferred in practice because of ease of insertion as compared to the ‘Cut Straight catheter’.

Transient flow in the SVC is not expected to influence this recommendation. *In vitro* validation however may be useful to ascertain the results of this numerical study.

The chosen standard PIV was a successful method to measure velocity magnitudes in the small scale of a dialysis catheter model. Velocity and derived shear strain distributions in two orthogonal planes of three different catheter models were compared qualitatively and quantitatively to the numerical results. CFD was validated by using PIV.

## IX. Conclusions and future prospects.

This dissertation focused on the study of blood flow in cardiovascular devices (heart valves, vascular access) with Particle Image Velocimetry (PIV) in *in vitro* experimental set-ups. The thesis was organized into two major parts. For the background, in part A, the introduction to cardiovascular anatomy and physiology was presented together with a basic description of the advanced measuring technique, PIV. The contents of part B presented six selected cases where different modalities of PIV flow visualization were used. The use of artificial organs as prosthetic heart valves (PHV) or treatment procedures using catheters and grafts needs to be studied in terms of blood flow properties within these geometries. The haemodynamic quality of the blood flow through an artificial organ is in many cases related to the diseases resulting from this kind of treatment. Especially for PHV, as a long term treatment for the patients with severe valvular heart disease (VHD). It is important to improve the design to achieve the flow dynamics properties close to the ones of healthy natural valves. Since it is not feasible to continuously study the real conditions of an implanted PHV in a patient, mock loops are designed to simulate a patient in *in vitro* conditions. In such mock loops different investigating methods can be used, which are for several reasons not possible in *in vivo* situation. In this hydrodynamic study we present PIV as an optimal experimental approach to study the flow dynamics in different *in vitro* mock loops. The non invasive approach is bringing the advantage of not disturbing the flow by placing a measuring device. Even though particles have to be added to the fluid, their influence upon flow is negligible because of their size and amount needed. Another great advantage is the planar approach and high resolution compared to e.g., single point measurement technique Laser Doppler Anemometry (LDA). The accuracy of the calculated results is above 95%. Different modalities of PIV may measure miscellaneous parameters. Stereoscopic PIV for instance is able to determine the flow field composed of three-component velocity vectors. The 3<sup>rd</sup> velocity (the out of plane) component might reveal information about the complexity of the flow. The high speed PIV

approach resolves the fluid flow in the detailed time domain and thus visualizes its development. It can therefore visualize a rapid event, e.g., closing of the valve leaflet and its rebound. Another advantage of the high speed approach is the possibility to quantify the frequency distribution of the velocity field at each point of the investigated region of interest. The highest frequencies have the more impact on the development of the flow pattern. However, this quantification is mainly useful for steady flows.

The major objective of this research was to visualize the blood flow in simulated mock loops by using PIV. Based on the demonstrated cases, we can say that PIV is suitable technique to study these kinds of flows. Moreover, due to its accuracy, it has nowadays become also a standard technique to validate Computational Fluid Dynamics (CFD) based designs and simulations. The future direction in biomedical field tend to use CFD codes for the quantification of patient specific flow conditions across an artificial organ. The virtual geometry of a model is easier to generate than to cast a physical transparent model needed for PIV investigation. Moreover, CFD yields more information and spatial resolution even in the regions of interest, where experimental techniques don't have access. Nevertheless, bioCFD is at the beginning of its evolution and still needs an experimental validation in complex flows such as in case of fluid-structure interaction.

The presented results are useful for deeper understanding of the flow through the particular valves. The information on the performance of specific PHV in different mock loops reveals the major differences. This information could help the designer s of the PHV innovate the architecture of the valves, change the opening angles and/or the shape of the leaflet. However, these results are expected to support other more detailed study, which is necessary for quantification of the flow quality. Moreover, the structure of the PHV and the aorta itself is a very complex 3D structure and as such it should be concerned. Therefore as a future aim, I suggest to perform three dimensional study of specific PHV in order to quantify the entire flow distribution within the whole volume downstream the valve.

Nevertheless, according to the presented results, the major difference is the flow distribution of the bileaflet and monoleaflet valves can be used for comparison of the flow quality. The three jet stream structure behind a bileaflet has a symmetrical distribution compared to a monoleaflet model. The three jet streams over the entire systolic phase don't have strong third velocity component. The higher SS, as an indicator of blood damage risk, occurs in the vortices and flow with a higher velocity. Therefore, generally speaking, it is expected that the monoleaflet models have a greater blood damage risk as the bileaflet models.



## Bibliography

- [1] Sherwood, L. (2004). "Human Physiology From cells to Systems", *Brooks/Cole* ISBN 0-534-39536-8
- [2] Darovic, G. (1995). "Hemodynamic monitoring: Invasive and noninvasive clinical application., 2nd ed." *W.B. Saunders Company*
- [3] Claessens, T. (2006). "Model-Based Quantification of Systolic and Diastolic Left Ventricular Mechanics", PhD Thesis, ISBN 13 978-90-8578-124-0, *Ghent University*
- [4] Matthys, K. (2004). "Assesment of Vascular Hemodynamics: Investigation of non-invasive and minimally invasive methods for assesment of vascular function at rest and during cardiovascular chalenge." PhD thesis, *Ghent University*
- [5] Dumont, K. (2005). "Experimental and numerical modelling of heart valve dynamics." PhD thesis, *Ghent, University*
- [6] Virgilio, R. W., Long, D. M., Mundth, E. D. and McClenathan, J. E. (1961) "The effect of temperature and hematocrit on the viscosity of blood." *Surgery*, **55** 825-30.
- [7] Artmann, G. M., Kelemen, C., Porst, D., Büldt, G. and Chien, S. (1998) "Temperature Transitions of Protein Properties in Human Red Blood Cells ", *Biophysical Journal*, **75**(6) 3179-3183.
- [8] Pries, A. R., Neuhaus, D. and Gaehtgens, P. (1992) "Blood viscosity in tube flow: dependence on diameter and hematocrit." *Am J Physiol*, **263**(6 Pt 2) H1770-8.
- [9] Fåhræus, R. and Lindqvist, T. (1931) "The viscosity of the blood in narrow capillary tubes." *The american journal of physiology*(96) 562-568.
- [10] Yamashita, K., Yamaguchi, K., Yamamoto, T., Shirabe, S., Hashiguchi, N., Kaji, M. and Tochihara, Y. (2005) "Hematological change in venous blood of the lower leg during prolonged sitting in a low humidity and hypobaric environment." *J Physiol Anthropol Appl Human Sci*, **24**(6) 611-5.
- [11] Keatinge, W. R., Coleshaw, S. R., Easton, J. C., Cotter, F., Mattock, M. B. and Chelliah, R. (1986) "Increased platelet and red cell counts, blood viscosity, and plasma cholesterol levels during heat stress, and mortality from coronary and cerebral thrombosis." *Am J Med*, **81**(5) 795-800.
- [12] Lee, G. R., Bithell, T. C., Foerster, J., Athens, J. W. and Lukens, J. N. (1993). "Wintrobe's Clinical Hematology", *Lea & Febiger*
- [13] Cho, Y. I. and K.R., K. (1991) "Effects of the non-Newtonian viscosity of blood on flows in a diseased arterial vessel. Part 1: Steady flows." *Biorheology*, **28**((3-4)) 241-62.

- [14] Hinghofer-Szalkay, H. and Greenleaf, J. (1987) "Continuous monitoring of blood volume changes in humans." *Journal of Applied Physiology*, **63**(3) 1003-7.
- [15] Martini, F. H. and Welch, K. (1998). "Fundamentals of Anatomy and Physiology: Applications Manual ", *Gale group* ISBN 0130962929
- [16] Bender, J. (1992). "Yale University School of Medicine Heart book", *William Morrow and Company Inc.* ISBN 0-688-09719-7
- [17] Yoganathan, A. P., He, Z. and Casey Jones, S. (2004) "Fluid mechanics of heart valves." *Annu Rev Biomed Eng*, **6** 331-62.
- [18] Hufnagel, C. A., Villegas, P. D. and Nahas, H. (1958) "Experiences with new types of aortic valvular prostheses." *Ann Surg*, **147**(5) 636-44; discussion 644-5.
- [19] Vongpatanasin, W., Hillis, L. D. and Lange, R. A. (1996) "Prosthetic heart valves." *N Engl J Med*, **335**(6) 407-16.
- [20] Bettadapur, M. S., Griffin, B. P. and Asher, C. R. (2002) "Caring for patients with prosthetic heart valves." *Cleve Clin J Med*, **69**(1) 75-87.
- [21] Jozwik, K. S. (2006). "Mechanical disc tilting heart valve with a nanocrystalline diamond layer", PhD, *Technical University of Lodz*
- [22] Cobanoglu, A., Fessler, C. L., Guvendik, L., Grunkemeier, G. and Starr, A. (1988) "Aortic valve replacement with the Starr-Edwards prosthesis: a comparison of the first and second decades of follow-up." *Ann Thorac Surg*, **45**(3) 248-52.
- [23] Schoevaerdt, J. C., Buche, M., el Gariani, A., Lichtsteiner, M., Jaumin, P., Ponlot, R. and Chaland, C. H. (1987) "Twenty years' experience with the Model 6120 Starr-Edwards valve in the mitral position." *J Thorac Cardiovasc Surg*, **94**(3) 375-82.
- [24] Simons, A. P. (2002). "Entwicklung eines transparenten, elastischen Aortenmodells und dessen Implementierung in einen Teststand zum Testen von stentless Herzklappen – Prothesen", diploma thesis, *University of Applied Sciences Aachen, Division Juelich, Germany*
- [25] Hodges, T. C., Fillinger, M. F., Zwolak, R. M., Walsh, D. B., Bech, F. and Cronenwett, J. L. (1997) "Longitudinal comparison of dialysis access methods: risk factors for failure." *J Vasc Surg*, **26**(6) 1009-19.
- [26] Krueger, U., Zanow, J. and Scholz, H. (2002) "Computational fluid dynamics and vascular access." *Artif Organs*, **26**(7) 571-575.
- [27] Erben, J., Kvasnicka, J., Bastecky, J. and Vortel, V. (1969) *Proc EDTA* 59-64.
- [28] Raffel, M., Willert, C. and Kompenhans, J. (1998). "Particle image Velocimetry", *Springer* ISBN 3-540-63683-8

- [29] Menzel, R. (1994). "Laser Spectroscopy: techniques and applications", *CRC* ISBN 978-0824792657
- [30] New Wave Research. "Nd:YAG Laser Systems." Retrieved 05.05.2007, 2007, from <http://www.new-wave.com/1nwrProducts/SoloPIV.htm>.
- [31] Koechner, W. (1999). "Solid-State Laser Engineering", *Springer* ISBN 3540650644
- [32] New Wave Research. "Pegasus-PIV." Retrieved 05.05.2007, from <http://www.new-wave.com/1nwrProducts/PegasusPIV.htm>.
- [33] Henderson, A. R. (1997). "A guide to laser safety", *Springer* 0412729407
- [34] ILA GmbH. "Articulated Mirror Arm." Retrieved 08.06.2007, from <http://www.ila.de>.
- [35] Van de Hulst, H. C. (1957). "Light scattering by small particles." *John Wiley & Sons, Inc.*
- [36] Van de Hulst, H. C. (1981). "Light scattering by small particles", *Dover Publications*
- [37] Adrian, R. J. (2005) "Twenty years of particle image velocimetry." *Experiments in fluids*, **39**(2) 159-169.
- [38] Willert, C. and Gharib, M. (1991) "Digital particle image velocimetry." *Experiments in fluids*, **10**(4) 181-193.
- [39] Westerweel, J. (1993). "In: Cha SS, Trolinger JD (eds) Analysis of PIV interrogation with low pixel resolution. " SPIE, Bellingham, Washington,, SPIE.
- [40] PCO AG. (2007). "Sensicam QE." Retrieved 05.02.2007, from <http://www.pco.de>.
- [41] Litwiller, D. (2001) "CCD vs. CMOS: Facts and Fiction." *Photonics spectra*(January) pp. 154-158.
- [42] Photron Inc. "ultima APX-RS." Retrieved 05.05.2007, from <http://www.photron.com/products.cfm?id=KingOfHighSpeedVideo>.
- [43] ILA GmbH. (2005). "Newsletter." Retrieved 05.05.2007, from [http://www.ila.de/News/ila\\_newsletter\\_07\\_05.pdf](http://www.ila.de/News/ila_newsletter_07_05.pdf).
- [44] Lourenco, L. ( 1996 ) "Particle image velocimetry." *Von K'arm'an Institute Lecture Series 1996-03, Belgium: Rhode-Saint Gen'ese*
- [45] Riethmuller, M. L. (1996). Particle Image Velocimetry, Von Karman Institute for fluid dynamics.
- [46] Stanislas, M., Okamoto, K. and Kähler, C. J. (2003) "Main results of the First International PIV Challenge." *Measurement Science and Technology*(14).

- [47] Stanislas, M., Okamoto, K. and Kähler, C. J. (2005) "Main results of the Second International PIV Challenge ", *Experiments in fluids*(39) 170-191.
- [48] ILA GmbH. "VidPIV software handbook." Retrieved 10.04., 2007.
- [49] Wernet, M. (2005) "Symmetric phase only filtering: a new paradigm for DPIV data processing." *Measurement Science and Technology*, **16** 601–618.
- [50] Scarano, F. (2004). "On the stability of iterative PIV image interrogation methods". 12th International Symposium on Applications of Laser Techniques to Fluid Mechanics, Lisbon, Portugal.
- [51] Willert, C. (1997) "Stereoscopic digital particle image velocimetry for application in wind tunnel flows." *Measurement Science and Technology*, **8** 1465–1479.
- [52] Staude, W. (2001). "Laser-Strophometry.High-Resolution Techniques for Velocity Gradient Measurements in Fluid Flows." *Springer*,15-17 ISBN: 978-3-540-42622-6
- [53] Bluestein, D., Einav, S. and Hwang, N. H. (1994) "A squeeze flow phenomenon at the closing of a bileaflet mechanical heart valve prosthesis." *J Biomech*, **27**(11) 1369-78.
- [54] Makhijani, V. B., Siegel, J. M., Jr. and Hwang, N. H. (1996) "Numerical study of squeeze-flow in tilting disc mechanical heart valves." *J Heart Valve Dis*, **5**(1) 97-103.
- [55] Makhijani, V. B., Yang, H. Q., Dionne, P. J. and Thubrikar, M. J. (1997) "Three-dimensional coupled fluid-structure simulation of pericardial bioprosthetic aortic valve function." *Asaio J*, **43**(5) M387-92.
- [56] Hsu, A. T., Yun, J. X. and Hwang, N. H. (1999) "Application of an unstructured grid algorithm to artificial heart valve simulations." *Asaio J*, **45**(6) 581-6.
- [57] Kelly, S. G., Verdonck, P. R., Vierendeels, J. A., Riemsdagh, K., Dick, E. and Van Nooten, G. G. (1999) "A three-dimensional analysis of flow in the pivot regions of an ATS bileaflet valve." *Int J Artif Organs*, **22**(11) 754-63.
- [58] Kelly, S. G. (2002) "Computational fluid dynamics insights in the design of mechanical heart valves." *Artif Organs*, **26**(7) 608-13.
- [59] Shipkowitz, T., Ambrus, J., Kurk, J. and Wickramasinghe, K. (2002) "Evaluation technique for bileaflet mechanical valves." *J Heart Valve Dis*, **11**(2) 275-82.
- [60] Goubergrits, L., Leirner, A. and Affeld, K. (2003) "Trileaflet valve for VAD use with purged sinus." *Artif Organs*, **27**(6) 586-91.
- [61] Shi, Y., Zhao, Y., Yeo, T. J. and Hwang, N. H. (2003) "Numerical simulation of opening process in a bileaflet mechanical heart valve under pulsatile flow condition." *J Heart Valve Dis*, **12**(2) 245-55.

- [62] Yin, W., Alemu, Y., Affeld, K., Jesty, J. and Bluestein, D. (2004) "Flow-induced platelet activation in bileaflet and monoleaflet mechanical heart valves." *Ann Biomed Eng*, **32**(8) 1058-66.
- [63] King, M. J., Corden, J., David, T. and Fisher, J. (1996) "A three-dimensional, time-dependent analysis of flow through a bileaflet mechanical heart valve: comparison of experimental and numerical results." *J Biomech*, **29**(5) 609-18.
- [64] Hoerstrup, S. P., Sodian, R., Sperling, J. S., Vacanti, J. P. and Mayer, J. E., Jr. (2000) "New pulsatile bioreactor for in vitro formation of tissue engineered heart valves." *Tissue Eng*, **6**(1) 75-9.
- [65] Dumont, K., Yperman, J., Verbeken, E., Segers, P., Meuris, B., Vandenberghe, S., Flameng, W. and Verdonck, P. R. (2002) "Design of a new pulsatile bioreactor for tissue engineered aortic heart valve formation." *Artif Organs*, **26**(8) 710-4.
- [66] Vierendeels, J. A., Dumont, K. and Verdonck, P. R. (2005) "A partitioned strongly coupled fluid-structure interaction method to model heart valve dynamics." *Accepted for the Journal of Computational and Applied Mathematics*.
- [67] Malek, A. M. and Izumo, S. (1996) "Mechanism of endothelial cell shape change and cytoskeletal remodeling in response to fluid shear stress." *J Cell Sci*, **109 ( Pt 4)** 713-26.
- [68] Scarano, F. (2002) "Iterative image deformation methods in PIV." *Measurement Science and Technology*, **13**(1) R1-R19(1).
- [69] Lecordier, B. and Trinité, M. (2003). "Advanced PIV algorithms with Image Distortion Validation and Comparison using Synthetic Images of Turbulent Flow." EuroPIV 2 Workshop, Zaragoza, Spain.
- [70] Thévenaz, P., Blu, T. and Unser, M. (2000). "Image interpolation and resampling, in: Handbook of medical imaging, processing & analysis." *I.N. Bankman, Academic Press*, 393-420
- [71] Zhang, H. and Bathe, K. J. (2001). "Computational Fluid and Solid Mechanics, chapter Direct and iterative computing of fluid flows fully coupled with structures." *Elsevier*
- [72] Piperno, S., Farhat, C. and Larrourou, B. (1995) "Partitioned procedures for the transient solution of coupled aeroelastic problems: Model problem, theory and 2-dimensional application." *Computer methods in applied mechanics and engineering*, **124**((1-2)) 79-112.
- [73] Matthies, H. G. and Steindorf, J. (2001). "Computational Fluid and Solid Mechanics, chapter How to make weak couplings strong." *Elsevier*
- [74] Vierendeels, J., Dumont, K. and Verdonck, P. R. (2003). "Stabilization of a fluid-structure coupling procedure for rigid body motion." 33rd AIAA Fluid Dynamics Conference and Exhibit, Orlando, US.

- [75] Dumont, K.,Stijnen, J. M.,Vierendeels, J.,van de Vosse, F. N. and Verdonck, P. R. (2004) "Validation of a fluid-structure interaction model of a heart valve using the dynamic mesh method in fluent." *Comput Methods Biomech Biomed Engin*, **7**(3) 139-46.
- [76] David, T. (2000). McDonald's Blood Flow in Arteries., chapter Advances in Fluid Dynamics: Verdonck P, Perktold K.: Intra and Extracorporeal Cardiovascular Fluid Dynamics., WIT Press: 177-208.
- [77] Bluestein, D.,Li, Y. M. and Krukenkamp, I. B. (2002) "Free emboli formation in the wake of bi-leaflet mechanical heart valves and the effects of implantation techniques." *J Biomech*, **35**(12) 1533-40.
- [78] Bluestein, D.,Yin, W.,Affeld, K. and Jesty, J. (2004) "Flow-induced platelet activation in mechanical heart valves." *J Heart Valve Dis*, **13**(3) 501-8.
- [79] Grigioni, M.,Daniele, C.,Morbiducci, U.,D'Avenio, G.,Di Benedetto, G. and Barbaro, V. (2004) "The power-law mathematical model for blood damage prediction: analytical developments and physical inconsistencies." *Artif Organs*, **28**(5) 467-75.
- [80] Grigioni, M.,Morbiducci, U.,D'Avenio, G.,Di Benedetto, G. and Del Gaudio, C. (2005) "Proposal for a new formulation of the power law mathematical model for blood trauma prediction." *Biomechanics and Modeling in Mechanobiology*, **Dec**:4(4) pp. 249-60.
- [81] Fontaine, A. A.,Ellis, J. T.,Healy, T. M.,Hopmeyer, J. and Yoganathan, A. P. (1996) "Identification of peak stresses in cardiac prostheses. A comparison of two-dimensional versus three-dimensional principal stress analyses." *Asaio J*, **42**(3) 154-63.
- [82] Ellis, J. T.,Healy, T. M.,Fontaine, A. A.,Weston, M. W.,Jarret, C. A.,Saxena, R. and Yoganathan, A. P. (1996) "An in vitro investigation of the retrograde flow fields of two bileaflet mechanical heart valves." *J Heart Valve Dis*, **5**(6) 600-6.
- [83] Barbaro, V.,Grigioni, M.,Daniele, C.,D'Avenio, G. and Boccanera, G. (1997) "19 mm sized bileaflet valve prostheses' flow field investigated by bidimensional laser Doppler anemometry (part II: maximum turbulent shear stresses)." *Int J Artif Organs*, **20**(11) 629-36.
- [84] Prasad, A. K.,Adrian, R. J.,Landreth, C. C. and Offutt, P. W. (1992) "Effect of resolution on the speed and accuracy of particle image velocimetry interrogation." *Experiments in fluids*, **13** 105-16.
- [85] Marassi, M.,Castelini, P.,Pinotti, M. and Scalise, L. (2004) "Cardiac valve prosthesis flow performances measured by 2D and 3D-stereo particle image velocimetry." *Experiments in Fluids*, **36**(1) 176-186.
- [86] Kaminsky, R.,Rossi, M.,Morbiducci, U.,Scalise, L.,Castelini, P.,Kallweit, S.,Verdonck, P. and Grigioni, M. (2005). 3D PIV measurements of prosthetic heart valve dynamics. *International Journal of Artificial Organs*. **28**: 868.

- [87] Kaminsky, R., Rossi, M., Morbiducci, U., Scalise, L., Castellini, P., Kallweit, S., Verdonck, P. and Grigioni, M. (2005) "Time resolved PIV technique for high temporal resolution measurements of prosthetic heart valves fluid dynamics." *International Journal of Artificial Organs*, **28**(9) 946.
- [88] Rossi, M., Morbiducci, U. and Scalise, L. (2005) "Laser based measurement techniques applied to the study of prosthetic mechanical heart valves fluid dynamics." *Int J Artif Organs*, **28**(9).
- [89] Prasad, A. K. and Adrian, R. J. (1993) "Stereoscopic Particle Image Velocimetry Applied to Liquid Flows." *Experiments in fluids*, **15** 49-60.
- [90] Temple, L. J., Serafin, R., Calvert, N. G. and Drabble, J. M. (1964) "Principles of Fluid Mechanics Applied to Some Situations in the Human Circulation and Particularly to the Testing of Valves in a Pulse Duplicator." *Thorax*, **19** 261-7.
- [91] Grigioni, M., Daniele, C., D'Avenio, G., Morbiducci, U., Del Gaudio, C., Abbate, M. and Di Meo, D. (2004) "Innovative technologies for the assessment of cardiovascular medical devices: state-of-the-art techniques for artificial heart valve testing." *Expert Rev Med Devices*, **1**(1) 81-93.
- [92] Morbiducci, U., D'Avenio, G., Del Gaudio, C. and Grigioni, M. (2004). "Testing requirements for stereoscopic Particle Image Velocimetry measurements of mechanical heart valves fluid dynamics." Proceedings on III Workshop BioFluMen, Istituto Superiore di Sanità, Rome.
- [93] Leo, H. L., Dasi, L. P., Carberry, J., Simon, H. A. and Yoganathan, A. P. (2006) "Fluid dynamic assessment of three polymeric heart valves using particle image velocimetry." *Ann Biomed Eng*, **34**(6) 936-52.
- [94] Brücker, C., Steinseifer, U., Schröder, W. and Reul, H. (2002) "Unsteady flow through a new mechanical heart valve prosthesis analysed by digital particle image velocimetry." *Measurement Science and Technology*, **13**(7) 1043-1049.
- [95] Grigioni, M., Morbiducci, U., D'Avenio, G., Di Meo, D. and Del Gaudio, C. (2005) "Laser techniques to study prosthetic heart valves fluid dynamics." *In Recent Research Developments in Biomechanics, Transworld Res. Network, Trivandrum :79-106*.
- [96] Uzol, O. and Camci, C. (2001). "The effect of sample size, turbulence intensity and the velocity field on the experimental accuracy of ensemble averaged PIV measurements." 4th International Symposium on Particle Image Velocimetry.  
, Gottingen, Germany.
- [97] Yoganathan, A. P., Corcoran, W. H., Harrison, E. C. and Carl, J. R. (1978) "The Bjork-Shiley aortic prosthesis: flow characteristics, thrombus formation and tissue overgrowth." *Circulation*, **58**(1) 70-6.

- [98] Sallam, A. M. and Hwang, N. H. (1984) "Human red blood cell hemolysis in a turbulent shear flow: contribution of Reynolds shear stresses." *Biorheology*, **21**(6) 783-97.
- [99] Giersiepen, M.,Wurzinger, L. J.,Opitz, R. and Reul, H. (1990) "Estimation of shear stress-related blood damage in heart valve prostheses--in vitro comparison of 25 aortic valves." *Int J Artif Organs*, **13**(5) 300-6.
- [100] Nygaard, H.,Giersiepen, M.,Hasenkam, J. M.,Westphal, D.,Paulsen, P. K. and Reul, H. (1990) "Estimation of turbulent shear stresses in pulsatile flow immediately downstream of two artificial aortic valves in vitro." *J Biomech*, **23**(12) 1231-8.
- [101] Grigioni, M.,Daniele, C.,D'Avenio, G. and Barbaro, V. (1999) "A discussion on the threshold limit for hemolysis related to Reynolds shear stress." *J Biomech*, **32**(10) 1107-12.
- [102] Lim, W. L.,Chew, Y. T.,Chew, T. C. and Low, H. T. (2001) "Pulsatile flow studies of a porcine bioprosthetic aortic valve in vitro: PIV measurements and shear-induced blood damage." *J Biomech*, **34**(11) 1417-27.
- [103] Bottio, T.,Casarotto, D.,Thiene, G.,Caprili, L.,Angelini, A. and Gerosa, G. (2003) "Leaflet escape in a new bileaflet mechanical valve: TRI technologies." *Circulation*, **107**(18) 2303-6.
- [104] Hanle, D. D.,Harrison, E. C.,Yoganathan, A. P. and Corcoran, W. H. (1986) "In vitro velocity measurements down stream from the Ionescu-Shiley aortic bioprosthesis in steady and pulsatile flow." *Med Biol Eng Comput*, **24**(5) 449-59.
- [105] Baldwin, J. T.,Deutsch, S.,Petrie, H. L. and Tarbell, J. M. (1993) "Determination of principal reynolds stresses in pulsatile flows after elliptical filtering of discrete velocity measurements." *J Biomech Eng*, **115**(4A) 396-403.
- [106] Sung, H. W.,Cape, E. G. and Yoganathan, A. P. (1994) "In vitro fluid dynamic evaluation of the Carbomedics bileaflet heart valve prosthesis in the aortic and mitral positions." *J Heart Valve Dis*, **3**(6) 673-83.
- [107] Grigioni, M.,Daniele, C.,D'Avenio, G. and Barbaro, V. (2000) "Laser Doppler anemometry study of bidimensional flows downstream of three 19 mm bileaflet valves in the mitral position, under kinematic similarity." *Ann Biomed Eng*, **28**(2) 194-203.
- [108] Adrian, R. J. (1991) "Particle-imaging techniques for experimental fluid mechanics." *Annual Review of Fluid Mechanics*, **23** 261-304.
- [109] Kaminsky, R.,Kallweit, S.,Simons, A. P. and H.J, W. (2005). "PIV Measurements with high Temporal Resolution behind Artificial Heart Valves". 6th International Symposium on Particle Image Velocimetry, Pasadena, USA.
- [110] Browne, P.,Ramuzat, A.,Saxena, R. and Yoganathan, A. P. (2000) "Experimental investigation of the steady flow downstream of the St. Jude bileaflet heart valve: a comparison between laser Doppler velocimetry and particle image velocimetry techniques." *Ann Biomed Eng*, **28**(1) 39-47.

- [111] Subramanian, A., Mu, H., Kadambi, J. R., Wernet, M. P., Brendzel, A. M. and Harasaki, H. (2000) "Particle image velocimetry investigation of intravalvular flow fields of a bileaflet mechanical heart valve in a pulsatile flow." *J Heart Valve Dis*, **9**(5) 721-31.
- [112] Manning, K. B., Kini, V., Fontaine, A. A., Deutsch, S. and Tarbell, J. M. (2003) "Regurgitant flow field characteristics of the St. Jude bileaflet mechanical heart valve under physiologic pulsatile flow using particle image velocimetry." *Artif Organs*, **27**(9) 840-6.
- [113] Pierrakos, O., Vlachos, P. P. and Telionis, D. P. (2004) "Time-resolved DPIV analysis of vortex dynamics in a left ventricular model through bileaflet mechanical and porcine heart valve prostheses." *J Biomech Eng*, **126**(6) 714-26.
- [114] Akutsu, T. and Fukuda, T. (2005) "Time-resolved particle image velocimetry and laser doppler anemometry study of the turbulent flow field of bileaflet mechanical mitral prostheses." *J Artif Organs*, **8**(3) 171-83.
- [115] Cromheecke, M. E., Overkamp, P. J., de Mol, B. A., van Gaalen, G. L. and Becker, A. E. (1998) "Retrieval analysis of mechanical heart valves: impact on design and clinical practice." *Artif Organs*, **22**(9) 794-9.
- [116] Dumont, K., Vierendeels, J., Kaminsky, R., Van Nooten, G., Verdonck, P. R. and Bluestein, D. (2007) "Comparison of the Hemodynamic and Thrombogenic Performance of Two Bileaflet Mechanical Heart Valves using a CFD/FSI model." *accepted for publication in ASME*.
- [117] Redaelli, A., Bothorel, H., Votta, E., Soncini, M., Morbiducci, U., Del Gaudio, C., Balducci, A. and Grigioni, M. (2004) "3-D simulation of the St. Jude Medical bileaflet valve opening process: fluid-structure interaction study and experimental validation." *J Heart Valve Dis*, **13**(5) 804-13.
- [118] Dumont, K., Vierendeels, J. A., Segers, P., Van Nooten, G. J. and Verdonck, P. R. (2005) "Predicting ATS Open Pivot heart valve performance with computational fluid dynamics." *J Heart Valve Dis*, **14**(3) 393-9.
- [119] Yoganathan, A. P., Chandran, K. B. and Sotiropoulos, F. (2005) "Flow in prosthetic heart valves: state-of-the-art and future directions." *Ann Biomed Eng*, **33**(12) 1689-94.
- [120] Grigioni, M., Daniele, C., Del Gaudio, C., Morbiducci, U., Balducci, A., D'Avenio, G. and Barbaro, V. (2005) "Three-dimensional numeric simulation of flow through an aortic bileaflet valve in a realistic model of aortic root." *Asaio J*, **51**(3) 176-83.
- [121] Ge, L., Jones, S. C., Sotiropoulos, F., Healy, T. M. and Yoganathan, A. P. (2003) "Numerical simulation of flow in mechanical heart valves: grid resolution and the assumption of flow symmetry." *J Biomech Eng*, **125**(5) 709-18.
- [122] Bellhouse, B. J., Bellhouse, F. H. and Reid, K. G. (1968) "Fluid mechanics of the aortic root with application to coronary flow." *Nature*, **219**(5158) 1059-61.

- [123] Ohta, Y., Kikuta, Y., Shimooka, T., Mitamura, Y., Yuhta, T. and Dohi, T. (2000) "Effect of the sinus of valsalva on the closing motion of bileaflet prosthetic heart valves." *Artif Organs*, **24**(4) 309-12.
- [124] Kleine, P., Perthel, M., Nygaard, H., Hansen, S. B., Paulsen, P. K., Riis, C. and Laas, J. (1998) "Medtronic Hall versus St. Jude Medical mechanical aortic valve: downstream turbulences with respect to rotation in pigs." *J Heart Valve Dis*, **7**(5) 548-55.
- [125] Kaminsky, R., Kallweit, S., Weber, H. J., Claessens, T., Jozwik, K. and Verdonck, P. R. (2007) "Flow visualization through two types of aortic prosthetic heart valves using stereoscopic high speed particle image Velocimetry." *Accepted for publication in Artificial Organs*.
- [126] Affeld, K., Walker, P. and Schichl, K. (1989) "The use of image processing in the investigation of artificial heart valve flow." *ASAIO Trans*, **35**(3) 294-8.
- [127] Lim, W. L., Chew, Y. T., Chew, T. C. and Low, H. T. (1994) "Particle image velocimetry in the investigation of flow past artificial heart valves." *Ann Biomed Eng*, **22**(3) 307-18.
- [128] Daily, B. B., Pettitt, T. W., Sutura, S. P. and Pierce, W. S. (1996) "Pierce-Donachy pediatric VAD: progress in development." *Ann Thorac Surg*, **61**(1) 437-43.
- [129] Shandas, R. and Kwon, J. (1996) "Digital particle image velocimetry (DPIV) measurements of the velocity profiles through bileaflet mechanical valves: in vitro steady." *Biomed Sci Instrum*, **32** 161-7.
- [130] Brücker, C. (1997) "Dual-camera DPIV for flow studies past artificial heart valves." *Experiments in Fluids*, **22**(6) 496-506.
- [131] Akutsu, T. and Masuda, T. (2003) "Three-dimensional flow analysis of a mechanical bileaflet mitral prosthesis." *J Artif Organs*, **6**(2) 112-23.
- [132] Castellini, P., Pinotti, M. and Scalise, L. (2004) "Particle image velocimetry for flow analysis in longitudinal planes across a mechanical artificial heart valve." *Artif Organs*, **28**(5) 507-13.
- [133] Kaminsky, R., Morbiducci, U., Rossi, M. and Scalise, L. (2006) "3D stereo PIV Measurements of prosthetic heart valves fluid dynamics." *Clinician and Technology Journal*, **36**(2) 217-221.
- [134] Marrassi, M., Paone, N., M. P., Scalise, L. and Thomassini, E. P. (2002). Development of an advanced mechanical heart valves piv test bench. 11th International symposium on Application of Laser Techniques to Fluid Mechanics. Lisbon, Portugal.
- [135] Akutsu, T. and Saito, J. (2006) "Dynamic particle image velocimetry flow analysis of the flow field immediately downstream of bileaflet mechanical mitral prostheses." *J Artif Organs*, **9**(3) 165-78.

- [136] Kaminsky, R., Morbiducci, U., Rossi, M., Scalise, L., Verdonck, P. and Grigioni, M. (2007) "Time resolved PIV technique for high temporal resolution measurement of mechanical prosthetic aortic valves fluid dynamics." *International Journal of Artificial Organs*, **30**(2) 153-162.
- [137] Reul, H., Vahlbruch, A., Giersiepen, M., Schmitz-Rode, T., Hirtz, V. and Effert, S. (1990) "The geometry of the aortic root in health, at valve disease and after valve replacement." *J Biomech*, **23**(2) 181-91.
- [138] Raffel, M., Richard, H., Ehrenfried, K., Van der Wall, B., Burley, C., Beaumier, P., McAlister, K. and Pengel, K. (2004) "Recording and evaluation methods of PIV investigations on a helicopter rotor model ", *Experiments in Fluids*, **36**(1) 146-156.
- [139] Daughters, N., Baan, J., Covell, J., Reneman, R. and Yin, F. (1996). "systolic and diastolic function of the heart", *IOS Press* 1 85312 547 4
- [140] Wu, Z. J., Gao, B. Z., Slonin, J. H. and Hwang, N. H. (1996) "Bileaflet mechanical heart valves at low cardiac output." *Asaio J*, **42**(5) M747-9.
- [141] Feng, Z., Nakamura, T., Fujimoto, T. and Umezu, M. (2002) "In vitro investigation of opening behavior and hydrodynamics of bileaflet valves in the mitral position." *Artif Organs*, **26**(1) 32-9.
- [142] Pisoni, R. L. (2002) "Vascular access use and outcomes: results from the DOPPS." *Contrib Nephrol*(137) 13-9.
- [143] Schwab, S. J. (1994) "Assessing the adequacy of vascular access and its relationship to patient outcome." *Am J Kidney Dis*, **24**(2) 316-20.
- [144] Mareels, G., De Wachter, D. S. and Verdonck, P. R. (2004) "Computational fluid dynamics-analysis of the Niagara hemodialysis catheter in a right heart model." *Artif Organs*, **28**(7) 639-48.
- [145] Prakash, S. and Ethier, C. R. (2001) "Requirements for mesh resolution in 3D computational hemodynamics." *J Biomech Eng*, **123**(2) 134-44.
- [146] Twardowski, Z. J. and Seger, R. M. (2002) "Dimensions of central venous structures in humans measured in vivo using magnetic resonance imaging: implications for central-vein catheter dimensions." *Int J Artif Organs*, **25**(2) 107-23.
- [147] Cohen, M. L., Cohen, B. S., Kronzon, I., Lighty, G. W. and Winer, H. E. (1986) "Superior vena caval blood flow velocities in adults: a Doppler echocardiographic study." *J Appl Physiol*, **61**(1) 215-9.
- [148] Scarano, F. (2002) "Iterative image deformation methods in PIV." *Measurements Science and Technology*, **13** R1-19.
- [149] Thévenaz, P., Blu, T. and Unser, M. (2000). Image interpolation and resampling. Handbook of medical imaging, processing & analysis. Bankman, I. N. San Diego, CA, Academic Press: 393-420.
- [150] Wernet, M. (2005) "Symmetric phase only filtering: a new paradigm for DPV data processing." *Measurements Science and Technology*, **16** 601-618.

- [151] Cockett, G. C. (1987). The rheology and tube flow of blood. Handbook of bioengineering. Skalak, R. and Chien, S. Londen, Mc Green Hill.
- [152] Mareels, G., Kaminsky, R., Eloit, S. and Verdonck, P. R. (2007) "PIV Validated CFD Based Design to Reduce Shear Stress and Residence Time in Central Venous Hemodialysis Catheters." *accepted for publication in Artificial Organs*.
- [153] Hellums, J. D. and Hardwick, R. A. (1981). Response of Platelets to Shear Stress - a Review. The Rheology of Blood Vessels and Associated Tissues. Gross, D. R. and Hwang, N. H. C. Alphen aan den Rijn, Sijthoff & Noordhoff: 160-183.
- [154] Kroll, M. H., Hellums, J. D., McIntire, L. V., Schafer, A. I. and Moake, J. L. (1996) "Platelets and shear stress." *Blood*, **88**(5) 1525-41.
- [155] Waniewski, J., Kurowska, W., Mizerski, J. K., Trykozko, A., Nowinski, K., Brzezinska-Rajszyk, G. and Kosciesza, A. (2005) "The effects of graft geometry on the patency of a systemic-to-pulmonary shunt: a computational fluid dynamics study." *Artif Organs*, **29**(8) 642-50.
- [156] Giersiepen, M., Wurzinger, L. J., Opitz, R. and Reul, H. (1990) "Estimation of Shear Stress-Related Blood Damage in Heart-Valve Prostheses - Invitro Comparison of 25 Aortic Valves." *Int J Artif Organs*, **13**(5) 300-306.
- [157] Goubergrits, L. and Affeld, K. (2004) "Numerical estimation of blood damage in artificial organs." *Artif Organs*, **28**(5) 499-507.
- [158] Strony, J., Beaudoin, A., Brands, D. and Adelman, B. (1993) "Analysis of shear stress and hemodynamic factors in a model of coronary artery stenosis and thrombosis." *Am J Physiol*, **265**(5 Pt 2) H1787-96.

## Symbols, abbreviations and units

## Abbreviations

2C	two velocity component
2D	two dimensional
3C	three velocity component
3D	three dimensional
ALE	Arbitrary Lagrangian-Eulerian
CCD	charge-coupled device
CD	compact disc
CE-MRA	Contrast-enhanced MR angiography
CFD	Computational Fluid Dynamics
CMOS	Complementary metal-oxide-semiconductor
CO <sub>2</sub>	carbon dioxide
D	diameter
ECG	Electrocardiogram
FSI	fluid-structure interaction
ILA	Intelligent Laser Applications
LA	left atrium
LASER	Light Amplification by Stimulated Emission of Radiation
LDA	Laser Doppler Anemometry
LS	light sheet
LSO	light sheet optics
LV	left ventricle
MRI	Magnetic Resonance Imaging
Nd:YAG	neodymium-doped yttrium aluminium garnet
Nd:YLF	Neodymium-doped yttrium lithium fluoride
Nd <sup>3+</sup>	neodymium molecular form
O <sub>2</sub>	oxygen (molecular form)
PCI	Peripheral Component Interconnect
PHV	prosthetic heart valve
PIV	Particle Image Velocimetry
PLI	Platelet Lysis Index
PMMA	Polymethyl methacrylate
PTFE	polytetrafluoroethylene
PVC	Polyvinyl chloride
QE	quantum efficiency
RA	right atrium
RI	refractive index
ROI	region of interest
RT	residence time
RT	residence time
RV	right ventricle

SS	shear stress
SVC	superior vena cava
TE	tissue engineering
VHD	valvular heart disease
Wo	Womersley number

## Symbols

$\alpha_\gamma$	shear rate scale factor
$\alpha_v$	velocity scale factor
$b$	width
D	diameter of the tube
$d_p$	size of the particle
$E$	Young modulus
EI	stiffness
fps	frames per second
g	gravitational acceleration
$h$	thickness
$I$	moment of inertia
K	number of physical variables
$k_s$	spring constant
$k_{s,hinge}$	hinge stiffness
$l$	length
L	independent fundamental quantities
$M$	moment of force
M	duration of the cardiac cycle
$N$	number of segments
$p$	pressure
P	set of dimensionless variables
Q	flow rate
$\rho$	density
Re	Reynolds number
$R_x, R_y$	reaction forces
SS	shear stress
t	time instance
t'	a time instance after t
$u_f$	velocity of the fluid
$u_g$	gravitationally evoked velocity
$u_i$	i-component of velocity vector
$u_p$	velocity of the particle
$u_s$	velocity lag
v	velocity
$V_{ref}$	reference velocity vector
$\Delta l$	length of a segment
$\Delta t$	time step

$\eta$	dynamic viscosity
$\eta_{\text{blood}}$	dynamic blood viscosity
$\theta$	angle
$\ddot{\theta}$	acceleration of the leaflet
$\lambda$	wavelength
$\lambda_{\text{band}}$	bandpass wavelength
$\lambda_{\text{emission}}$	emission wavelength
$\lambda_{\text{excitation}}$	excitation wavelength
$\pi$	pi-constant (3.14)
$\rho_{\text{fluid}}$	density of the fluid
$\rho_p$	density of the particle
$\tau_s$	relaxation time
$\nu$	kinematic viscosity

## Units

$^{\circ}\text{C}$	Celsius temperature degree
$\mu\text{m}$	micrometer
Hz	Herz
kg	kilogram
L	litre
min	minute
mJ	millijoule
mL	millilitre
mm	millimeter
N	Newton
nm	nanometer
s	second
W	watt
$\mu\text{s}$	microsecond



